Spring 2015

Inclusion engineering in Mn-Si de-oxidized steel for thin-strip casting

Vivek Thapliyal

Department: Materials Science and Engineering

INCLUSION ENGINEERING IN Mn-Si DE-OXIDIZED STEEL FOR THIN-STRIP CASTING

by

VIVEK THAPLIYAL

A DISSERTATION

Presented to the Faculty of the Graduate School of the

MISSOURI UNIVERSITY OF SCIENCE AND TECHNOLOGY

In Partial Fulfillment of the Requirements for the Degree

DOCTOR OF PHILOSOPHY

in

MATERIALS SCIENCE AND ENGINEERING

2015

Approved
Dr. Jeffrey D. Smith, Advisor
Dr. David G. C. Robertson
Dr. Simon N. Lekakh
Dr. Ronald J. O'Malley
Dr. William G. Fahrenholtz

PUBLICATION DISSERTATION OPTION

This dissertation was prepared in the style utilized by *ISIJ International – The iron and Steel Institute of Japan*. The introduction and literature review present pertinent background on inclusions in Mn-Si killed steels, focusing on application in thin-strip casting process. Paper 1 (page 34-70) has been published in *Ironmaking & Steelmaking* under the title “Transient Inclusion Formation and Evolution in Silicon-Killed Steels”. Paper 2 (page 71-105) has been published in *ISIJ International* under the title “Inclusion Modification in Si-Mn Killed Steels using Titanium Addition”. Paper 3 (page 106-131) was submitted for publication in February, 2015 in *ISIJ International* under the title “A Kinetic Model for Vacuum Tank Degassing”.

ABSTRACT

The focus of this research was to understand inclusion formation and evolution in Mn-Si de-oxidized steels used in thin-strip casting. Inclusions formation and evolution in ultra-low carbon low-alloyed steels were studied. Inclusion engineering can be used to remove or modify detrimental inclusions, which cause casting issues.

The first part of this study focused on inclusion formation as a result of ferro-alloy addition. De-oxidation reaction in steels are the primary source of the typical oxide inclusion formed in steel. For Mn-Si de-oxidized steels ferro-silicon and ferro-manganese are the two ferro-alloys used for de-oxidation. Inclusion formation and evolution during the early stages of dissolution of these ferro-alloys was experimentally studied. The mechanism for inclusion formation in their transient phase was proposed.

The second part of this study shows the results of modification of inclusions observed in Mn-Si killed steel as a result of ferro-titanium addition. $MnO\text{-}SiO_2\text{-}Al_2O_3$ based inclusions were modified by ferro-titanium addition to form inclusions of lower melting points. These inclusions would cause fewer issues during casting.

In the third part of this study a comprehensive dynamic model for vacuum tank degasser (VTD) was developed. VTD is used in the industry to obtain ultra-low carbon steels. Further, VTD processing typically removes gaseous species from liquid steel which is essential for thin-strip casting. Inclusion content in the steel is further reduced by this process. The VTD model calculated thermodynamic equilibrium under different conditions within steel in a ladle during VTD processing. The model successfully predicted composition change in steel over time under VTD processing.

ACKNOWLEDGMENTS

It has been four and a half years, since I started on this journey towards one objective, during which I have seen highs and lows in life. It wouldn't have been possible without the support of so many people. First and foremost thanks to Dr. Jeffrey Smith, my advisor, for his support, guidance, motivation and his belief in me. Thanks for all the advice, both personal and professional, of which I will be forever indebted.

Thanks to Dr. Robertson for the guidance and numerous discussions. I would also like to thank Dr. Lekakh, Dr. O'Malley and Dr. Fahrenholtz for their time and valuable inputs to this work. Thanks to the Materials Science and Engineering Department for helping me throughout my stay at Missouri S&T.

I would like to thank Nucor for giving me the opportunity of working on the Castrip projects which have funded my stay at Missouri S&T.

I would like to thank Abhishek Kumar, for his help in conducting all the experiments, publications and setting up the tempo for continuous hard-work. I would like to thank Sean Padgett and Brad Osmonson for all the sample preparations. Thanks goes to my friends Manoj, Sid, Priyatham and Samrat for their support.

I would like to thank my parents, my sisters, brother-in-laws and my friends Hemant and Preeti for their understanding and unconditional support during my PhD. Lots of love to my nephew Atiksh for bringing smile to my face during the tough times and being the ball of happiness.

Finally, I would like to thank late Dr. Kent Peaslee for giving me the opportunity to start on this path and for always being an inspiration to me. Special thanks to Mary Peaslee for being a family to us.

TABLE OF CONTENTS

Page

LIST OF ILLUSTRATIONS

Page

SECTION

PAPER I

PAPER III

LIST OF TABLES

Page

SECTION

PAPER I

PAPER II

1. INTRODUCTION

1.1. THIN-STRIP CASTING

Thin-strip casting is a technique in which steel strip (1-15 mm thickness) is cast directly from liquid steel thus minimizing further size reduction and finishing steps. The concept of strip casting was invented by Bessemer in 1846 where he used a twin-roll caster to produce metallic strip from molten metal.[1-3] In 1865, he patented a twin-roll caster designed for iron and steel strips.[3] The major difficulties identified by Bessemer with his design were liquid metal feeding, edge containment, and strip quality.[2]Even though, this technique was invented as early as 1846, its commercial application advanced only in the last decade or so because of technical difficulties such as roll wear, low productivity, poor quality of the casts, variable solidification structures and mechanical properties.[2]

Twin-roll caster at Hikari (Nippon Steel Corporation and Mitsubishi Heavy Industries - Japan), Eurostrip (Joint European R&D Effortof VAI, ThyssenKrupp and ArcelorMittal - Germany), Castrip (Nucor Steel - USA, Broken Hill Proprietary Company - Australia and Ishikawajima-Harima Heavy Industries - Japan) and Postrip (POSCO -South Korea) are the few places where this technique was applied commercially.[2-7] Baostrip (Baosteel – China)and MAINSTRIP (SMS Demag -Germany, MAIN AG/MTAG Marti-Technologie AG - Switzerland and Corus Research, Development and Technology - UK) are other facilities where the twin-roll casting technology is in full-scale testing or semi-production phase and is advancing towards full commercialization.[2] Nippon Steel terminated the commercial operation of the strip caster at Hikari Works in September 2003.[2] Since 2003, the Eurostrip consortium has also been

reluctant to release any information regarding its progress and it is believed that that the project was terminated sometime in the mid 2000's.[2)] Since 2002, Castrip plant at Crawfordsville, Indiana, USA continues to produce thin-strip cast steel and is capable of producing 500,000 ton steel annually.[2,5-7)] A second facility at Blytheville, Arkansas, USA was commissioned in January, 2009 with similar production capacity.[2,5,6)] POSCO started production using its commercial-scale twin-roll strip (Postrip) at Pohang Works in July 2007 with annual capacity of 600,000 ton.[2)]

A schematic diagram depicting the major components of the CASTRIP process is shown in Figure 1.1. The figure shows two counter rotating rolls which form two individual shells that are formed into a continuous sheet, of thickness less than 2 mm, at the roll nip. It has been reported that only Mn-Si de-oxidized steels are used in the CASTRIP process to ensure that inclusions formed ($MnO\text{-}SiO_2$ based) are liquid during the casting process to avoid clogging.[8-11)] Also, Si-Mn deoxidization is utilized for adequate heat transfer.[8-11)]

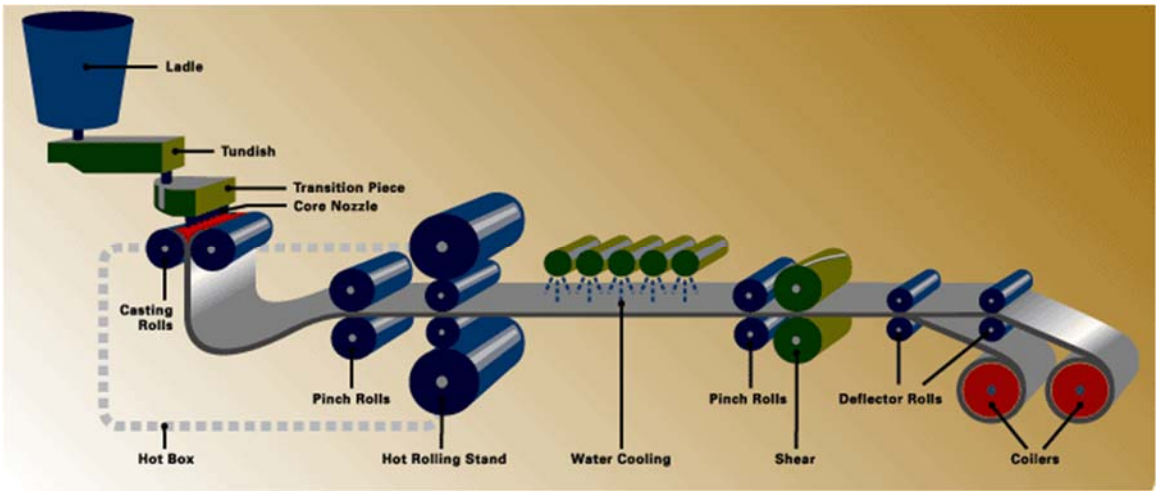

Figure 1.1. A representation of the main components of the CASTRIP process[8)]

Thin-strip casting is different from the traditional casting techniques having very thin molds (1-2 mm) and very fast cooling rates (1700ºC/sec) compared to conventional casting.[8)] The microstructure of steel (and hence the properties) obtained via thin-strip casting are different due to the fast cooling rate. Finely dispersed inclusions formed during solidification are helpful in achieving the microstructure.[8-10)] However, even very small inclusions (< 10 μm)[8-10)] present in the liquid steel can cause casting issues and defects in the final product. So, the control of inclusion chemistry and size is very important for smooth casting operation (without clogging or strip-breaks) and achieving desired properties in the final product.[8-10)]

1.2. INCLUSIONS

Inclusions are non-metallic compounds, solutions or mixtures (multi-phase inclusions) found in steel. They comprise of metallic elements (Fe, Mn, Al, Si, Ti, Ca, Mg etc.) and non-metallic elements (O, C, N, S etc.).

Inclusion type can be defined based on the inclusion chemistry as oxides, sulfides, carbides or nitrides having oxygen, sulfur, carbon or nitrogen as the primary non-metallic elements respectively. Inclusions can also be a combination of these compounds and can be termed as complex inclusions.

Inclusions can also be categorized based on how they form. Indigenous inclusions form within steel as a result of chemical reactions during de-oxidation, re-oxidation, alloy-addition, ladle-refinement, slag-steel interaction, refractory-steel interaction and solute-segregation. For example; Al_2O_3 inclusions form in Al-killed steel during de-oxidation and can modify to $CaO \cdot Al_2O_3$ inclusions during Ca treatment in the ladle.[12,13] Exogenous inclusions form in steel as a result of physical processes like slag-entrapment or refractory wear. Inclusions formed as a result of de-oxidation, re-oxidation and solute-segregation are generally primary oxides, sulfides, carbides or nitrides. Secondary inclusions form as a result of heterogeneous nucleation of inclusions on the primary inclusions.

In the 21st century the major challenges for the steel industry are (a) to develop new steel grades with better properties; (b) to reduce energy consumption, and (c) to reduce greenhouse gas emission. Developing new steel grades with improved properties requires careful control of chemistry and cleanliness as inclusions are detrimental to achieving the desired properties. Producing thin-strip directly from molten steel is an

effective way to reduce greenhouse gas emission and energy consumption. Thin-strip casting reduces the greenhouse gas emission by 90% and reduces energy consumption by 75% as compared to traditional slab-casting.[5-10] With processes such as thin-strip casting even small inclusions can cause clogging and strip-breaks calling into question the viability of the approach.

Steel cleanliness is generally defined by the inclusion content of the steel. Inclusions are present in all steels and it is not possible to remove them as they form throughout the steel-making process and during solidification and cooling. Thus, critical inclusion size and content are defined to decide whether or not steel is clean. Typical steel cleanliness requirements for various steel products were reported by Zhang at al.[14] and are summarized in Table 1.1. To make clean steel it is essential to understand how inclusions form, how they evolve, and how they can be modified or removed from the steel.

Table 1.1. Typical steel cleanliness requirements for various steel products

Steel Product	Maximum impurity fraction (ppm)	Maximum inclusion size (μm)
Automotive and deep-drawing sheet	[C]≤30, [N] ≤30	100
Drawn and ironed cans	[C]≤30, [N]≤30, T.O.≤20	20
Line pipe	[S]≤30, [N]≤50, T.O.≤30	100
Ball bearings	T.O.≤10	15
Tire cord	[H]≤2, [N]≤40, T.O.≤15	20
Heavy plate steel	[H]≤2, [N]≤30-40, T.O.≤20	Single inclusion=13, cluster=200
Wire	[N]≤60, T.O.≤30	20

1.2.1. Inclusion Sources. Oxides and sulfide inclusions are the most common inclusions observed in steel. De-oxidation reactions and alloying additions are considered to be the primary sources of oxide inclusions. However, de-oxidation of steel is essential to prevent the formation of blowholes (CO evolution) and FeO during steel solidification.[15] Aluminum, silicon and manganese are the most common deoxidizers used in steel making. These de-oxidizers react with dissolved oxygen in steel to form their primary oxides as shown in the following reactions:

$$2[Al] + 3[O] = Al_2O_3 \quad (1)$$

$$[Si] + 2[O] = SiO_2 \quad (2)$$

$$[Mn] + [O] = MnO \quad (3)$$

Ferro-alloys like ferro-silicon, ferro-manganese and silico-manganese are used as deoxidizers in Mn-Si killed steel. The dissolution (melting) behavior of different ferro-alloys has been described in detail by Argyropoulos et al.[16,17]. They summarized the

expected dissolution times needed for assimilation of different ferro-alloys in liquid steel. In this work, the author has used these dissolution mechanisms to study inclusion formation immediately after ferro-alloy additions and prior to macro-mixing/homogenization.

Ferro-alloys contain some (≤5%) impurities in the form of carbon, aluminum, magnesium, and sulfur.[18] The knowledge of these impurities is essential in determining ferro-alloy quality which in turn provides information about nature of inclusions formed in steel. Pande et al.[19] characterized different ferro-alloys for their impurity content through chemical and microstructural analysis. It was reported that ferro-silicon contains impurities like Al (0.05 – 0.44%) and Ca (0.03 – 0.12) and ferro-manganese contains Al (0.021 – 0.22 %), Mg (0.09 – 0.11 %) and P (0.02 – 0.15 %).[19] These impurities under equilibrium conditions are expected to form oxide inclusions of Al_2O_3, CaO, MgO or combinations of these possibly in solution with MnO-SiO_2.

It is a common practice to add calcium to steel to modify alumina inclusions to form liquid calcium aluminates which can be shown through following chemical reactions[15]:

$$Ca(l) = Ca(g) \tag{4}$$

$$Ca(g) = [Ca] \tag{5}$$

$$[Ca] + [O] = CaO \tag{6}$$

$$[Ca] + \left(x + {}^{1}/_{3}\right)[Al_2O_3] = CaO \cdot xAl_2O_3 + {}^{2}/_{3}\,[Al] \tag{7}$$

Magnesium oxides are also observed in steel and originate from ferro-alloys, refractories or slag through following chemical reaction:

$$[Mg] + [O] = MgO \quad (8)$$

Titanium can be used in steel-making as deoxidizer or to modify the existing inclusions to form titanium oxide (TiOx) inclusions (reaction 9).

$$[Ti] + x[O] = TiO_x \quad (9)$$

Sulfur content in the steel leads to the formation of sulfide inclusions during de-sulfurization or during cooling and solidification due to sulfur segregation. Additions of CaO are made to the slag for de-sulfurization. Calcium sulfide inclusions are also known to form during calcium treatment in steel (reaction 10).[15] Manganese sulfide inclusions are the commonly observed sulfide inclusions formed as a result of sulfur segregation (reaction 11). These inclusions can also nucleate on top of existing oxide inclusions to form complex inclusions.

$$[Ca] + [S] = CaS \quad (10)$$

$$[Mn] + [S] = MnS \quad (11)$$

Availability of nitride forming elements like aluminum, titanium, boron and zirconium along with access to air or dissolved nitrogen from the steel can result in the formation of nitride inclusions. Similarly, carbide forming elements like Cr, Ti etc. can

form carbide inclusions. The presence of other inclusions (oxides or sulfides) can act as nucleation sites for these inclusions.

Exogenous inclusions found in steel are generally complex in chemistry and large (>100 microns) in size. Industrially, ladle practices such as stirring (gas or electromagnetic) and slag practices are well established to avoid entrapment of slag droplets by steel. Researchers have studied inclusion formation due to slag entrapment.[20-23] Riboud et al.[20] reported that gas bubbling as well as turbulence caused at slag-metal interface due to non-equilibrium can lead to slag entrapment. Iguchi et al.[21] studied slag entrapment due to gas bubbling using water model to determine the critical gas flow rate. They showed that the formation of slag droplets becomes difficult by increasing slag viscosity. Formation of vortices during steel transfer operation between furnace, ladle, tundish or mold can cause slag to be drawn from one vessel to another.[24]

Ladle glaze is another source of inclusions as studied by various researchers.[25-27] Ladle glaze is formed due to adhering of the top slag as it flows down the ladle wall during the draining of the ladle to the tundish. Song et al.[27] studied inclusion from ladle glaze by using BaO as a tracer in the slag in industrial trial. They observed BaO containing inclusions in the samples from the ladle in the second and third heat after the tracer addition.

Mold flux is another potential source of inclusions which can be trapped during steel solidification or react with steel to form inclusions.[21,28-30] Iguchi et al.[21] studied mold slag and steel interface in industrial continuous casting molds. They observed that the formation of a wide range of inclusion sizes was possible by reduction of silica and sodium oxide from the casting powder by the deoxidizing elements used in aluminum or

aluminum/titanium killed steels. Feng et al.[30] used water and numerical modeling to determine optimal outlet angle and immersion depth for a submerged entry nozzle in a mold to minimize slag entrapment.

In thin-strip casting of steel, additional refractory components are required compared to traditional ladle and tundish refractories. These refractory components referred to as core-nozzles and side-dams and are typically made of zirconia-carbon and boron-nitride materials and they can also be source of exogenous inclusions.[31] The types of inclusions formed through interaction of BN-ZrO_2-SiC ceramic with Si-killed steel were reported by Kumar et al.[32,33]. Further, Kumar et al.[34] also studied behavior of zirconia-graphite refractories in thin-strip casting of steel and reported the dislodging of zirconia grains from the refractory into the steel.

1.2.2. Problems Due to Inclusions. Inclusions are detrimental to steel affecting its mechanical, chemical and thermal properties.[35-37] Zhang et al.[36] have summarized the different defects related to inclusions in steel. Maeda et al.[38] highlighted the importance of steel cleanliness to achieve high tensile strength for wire rods for tire cord steel. Murtaza et al.[39] report that non-metallic inclusions play a major role in crack initiation affecting the fatigue life in spring steels.

Researchers have reported that large alumina particles (>30μm) are the major source of fatigue problems in bearing steel.[36,40] Bearing life can be extended (by almost 30 times) by reducing the amount of large inclusions by lowering the oxygen content from 20 ppm to 3-6 ppm.[36,40] Ginzburg et al.[41] reviewed the defects in cast slabs and hot rolled products such as slivers, surface defects (trapped scum) and segregation (causing

brittleness) related to inclusions. Frank[42] provides a historical perspective of the problem of castability of steel due to alumina, calcium sulfide and spinel inclusions.

In general, the number and distribution of inclusions in steel plays an important role in initiation of fatigue cracks. Sulfide inclusions have high index of deformability at all temperatures and are not usually harmful for fatigue properties.[37] These inclusions participate in hot/cold working of steel and change their shape in accordance with surrounding steel matrix.[43-45] In contrast, oxide inclusions are harmful to fatigue properties depending upon their phase, size and position. Usually, spherical, non-deformable Ca-aluminate inclusions and Al_2O_3 inclusions are most detrimental to the fatigue properties.[45,46] Both of these inclusions do not change their shape during steel deformation. Large, exogenous oxide inclusions from slag or refractory origin are always detrimental to fatigue properties due to their size and irregular shape.

Hot-shortness is a fracture phenomenon which involves tendency of steel to brittle fracture in the hot forming temperature range.[37] This phenomenon is frequently attributed to sulfur content, and caused by the precipitation of FeS in the austenite grain boundaries of the steel.[47] Further, oxygen enhances the effect of sulfur, whereas manganese counteracts hot-shortness due to formation of MnS.

Surface finish of steel is sensitive to surface irregularities, therefore presence of different inclusions types influence the degree of surface-finish attainable. Schoberl et al.[48] reported the influence of deoxidation on the surface-finish of high chromium alloyed steel. They practiced different deoxidation methods (such as Fe-Cr-Si, Fe-Si, Ca-Si, Ca-Al, Al etc.) in the ladle and as a result inclusions of different compositions were formed. The authors concluded that number of inclusions was of more importance compared to

inclusion types. The inclusion count was closely connected to oxygen content in steel and deoxidation method which gave lowest oxygen content was more suitable for better surface finish.

1.2.3. Benefits of Inclusions. It is not possible to remove all the inclusions from steel. Steel with only 1 ppm of oxygen and sulfur contains 10^{10} -10^{12} inclusions per tonne, with most of them being too small (<1 μm) to remove.[49,50] Further, there are economic considerations for removing inclusions from steel which must be optimized. Very fine inclusions in small amounts can be beneficial to steel. They can be utilized in grain refinement by Zener pinning effect of finely distributed particles which capture grain boundary movement.[51]

Inclusions can also be used to achieve desired microstructure in steel. Ti, Ce and La based inclusions are known to affect steel microstructure.[51] Inclusions such as Ti_2O_3, Ti(C,N), and $(La,Ce)_2O_3$, CeS, and Ce_2O_3 are favorable nucleation sites for ferrite, whereas, CeO_2, La_2O_3, $CeAlO_3$ are favorable cites for cementite and austenite.[51-53] Ti-Oxides were especially effective to nucleate acicular ferrite.[51]

Pro-eutectoid ferrite can nucleate at inclusions within austenite grains which can be utilized to achieve fine ferrite-pearlite microstructure within coarse austenite grains.[54,55] The generation of intra-granular ferrite at inclusions to refine grain structures effectively improves the toughness of steel.[54,55] Researchers at Castrip have found that the non-metallic inclusion type (MnO-SiO_2 based) and size distribution (0.5 – 5 μm) play a very beneficial role in the development of the final microstructure by promoting the

intra-granular nucleation of acicular ferrite without adversely affecting the formability of the strip.[10)]

Inclusions can be made useful through the oxide metallurgy process by forming inclusions of the optimal chemistry, size, shape and distribution, although achievement is difficult in practice.

1.3. INCLUSION REMOVAL

The benefits of removing inclusions far outweigh the negatives. Large inclusions can be easily removed from the steel by utilizing good industrial practices. Following are the common techniques utilized to remove inclusions:

1.3.1. Degassing Treatment. Inclusions content in steel can be reduced by minimizing the content of sulfur, hydrogen, nitrogen and oxygen. This can be achieved by degassing treatment of the steel. There are two principle types of degassers: recirculating systems such as RH, RH-OB, RH-KTB and DH; and non-recirculating systems such as ladle or tank degassers, including VAD (vacuum arc degassing) and VOD (vacuum oxygen decarburization), and stream degassers.[56)] The type of degasser used generally depends upon the target product mix. For example, to produce ultra-low carbon steels, RH degassing is usually preferred.

In vacuum degassing, hydrogen, nitrogen, carbon, and oxygen are removed through following reactions[57)]:

$$2[H] = H_2\,(g) \tag{12}$$

$$2[N] = N_2\,(g) \tag{13}$$

$$[C] + [O] = CO\,(g) \tag{14}$$

$$[C] + (FeO) = CO(g) + [Fe] \tag{15}$$

$$[C] + {}^{1}/_{2}\,O_2(g) = CO\,(g) \tag{16}$$

Hydrogen and nitrogen dissolved in steel are removed by forming diatomic molecules; whereas, carbon is removed by reaction with oxygen present as dissolved oxygen, FeO in slag or gaseous oxygen (O_2) to form CO. Due to reduction in pressure the formation of CO and other gases (H_2, N_2 etc.) is favored.[58)]

Bannenberg et al.[59)] reported that in non-recirculating systems, the time required to remove 50% of the carbon is approximately 7 minutes, whereas in the recirculating system RH this time can be as short as 3 to 4 minutes. During degassing, rate of hydrogen removal is controlled by mass transfer in the liquid steel.[58)] Nitrogen removal is made possible in vacuum degassing, provided liquid steel is fully killed and has low sulfur content. Bannenberg et al.[60)] reported that 50% of the nitrogen can be removed in 15 minutes with initial nitrogen greater than 50 ppm, for a killed steel containing 2 ppm dissolved oxygen and 10 ppm sulfur and a tank pressure of 100 Pa.

In this work, a dynamic model for a vacuum tank degasser (VTD) has been developed which utilizes mixing and fluid flow data from computational fluid dynamics software (FLUENT)[61)] and calculates thermodynamic equilibrium at different locations in the VTD by FactSage 6.4[62)]. The model also provides information about change in inclusion composition and content as a result of VTD processing. A preliminary model for the same system was designed using process simulation software (METSIM)[63)].

1.3.2. Floatation. Inclusions vary in density with composition but are generally lighter than steel resulting in their floatation. The rate at which inclusions would rise in steel can be calculated by using Stokes' law. The velocity at which inclusion would rise in steel can be expressed as[64]:

$$v = \frac{2}{9}\frac{gr^2(\rho_{steel} - \rho_{inclusion})}{\mu} \quad (17)$$

From this equation, it can be seen that the size of the inclusion plays a key role in determining the rate of inclusion floatation. Mills[49] calculated that for an alumina inclusion the time required to float out a 100 μm inclusion from a depth of 2.5 meters will be 5 minutes compared to 2 hours for a 20 μm inclusion. Thus, it is important to aid inclusion floatation by promoting steel flow using gas bubbling or electro-magnetic stirring. This would also help in allowing inclusions to agglomerate to form larger inclusions which would be easier to float out.

Researchers have reported that the agglomeration and coalescence due to collision is essential in making inclusions larger to promote floatation.[49,64-69] Zhang et al.[64] studied inclusion removal in continuous casting tundish. They reported that the number densities of the inclusions greater than 25 μm in radius increases first due to collision (of smaller inclusions) and then decreases due to floatation, whereas, for less than 25 μm inclusions, it always decrease with the time. Similar behavior was reported by Sinha et al.[68] for their work in inclusion removal in continuous casting tundish. Kaufmann et al.[65] and Tacke et al.[66] modeled fluid flow and inclusion removal using Stokes velocities for inclusions rise to the top surface slag but ignored collision of inclusions and adhesion

to the solid surface.[64] Kaufmann et al.[65] studied the separation of inclusions by buoyancy in tundishes. They performed theoretical investigations for two different tundishes one with a baffle and one without and did not find any significant difference in the inclusion removal behavior for the two cases.

Tundishes are capable of appreciably diminishing the inclusions in the molten steel especially when flow control devices such as dams, weirs, filters and baffles[64-69] are used. By means of these devices, the flow could be directed to the top surface to enhance inclusion removal by floatation. A strong turbulent condition can be confined in the inlet zone using flow control devices which promotes the collision of inclusions and improves the inclusions removal.[64,68] Collision of inclusions can occur by three possible mechanisms[64]:

i. Brownian movement of the inclusions by which inclusions can contact, collide and coagulate each other,
ii. Turbulent collision due to the movement of turbulent eddies in steel, and
iii. Stokes collision due to difference in Stokes velocity of rise of different inclusions of different sizes.

Zhang et al.[64] also reported that smaller inclusions have a much larger collision removal rate but point out that not all inclusions colliding with each other will coalesce and some aggregates of inclusions break up. As the smaller inclusions are much larger in number than the large ones their collision number per unit time per unit volume is high.[49,50,64] Thus collision is a key way to remove smaller inclusions that are difficult to remove by floatation for their small rising velocities.[64,68] Lindborg and Torssell[69]

reported that in a turbulent bath coalescence of small inclusions leads to larger inclusions and that such a mechanism is very important in determining the rate of inclusion removal.

1.3.3. Inclusion Entrapment by Slag. The inclusions floating in the steel need to be captured by the slag at the surface otherwise the inclusions would continue to circulate with the steel. Therefore, one of key functions of the slag is to remove and assimilate the non-metallic inclusions contained in liquid steel. A particle (inclusion) reaching the slag/metal interface can pass into the slag layer with no-possibility of re-entrainment or will reach an equilibrium state after some oscillation. The entrapment of inclusions by the slag depends on the liquid flow at slag/metal interface and interfacial energies involved.[70] The following interfacial energy conditions enhance the inclusion removal[71-73]: (i) high metal/inclusion interfacial energy, (ii) high metal/slag interfacial energy, and (iii) low slag/inclusion interfacial energy. It implies that non-wetting solid phases (such as alumina by steel) are easier to get removed at the interface than liquid oxide inclusions.[74] In addition, steel cleanliness is improved by using a liquid basic slag that does not re-oxidize the steel and absorbs the oxide inclusions especially in the tundish.[75]

Rocabois et al.[70] developed an experimental technique to study the rate of entrapment of solid inclusions in liquid slag. In this technique, a steel rod with a slag droplet inside was melted through induction heating and inclusion entrapment phenomena were recoded. It was observed that slags with low alumina activity, high basicity and low viscosity (CaF_2 rich) were more efficient in assimilation of alumina

inclusions. In contrast, high slag viscosity is desirable for reduction of slag entrainment into the casting product.[76)]

Researchers have shown that by maintaining the appropriate slag chemistry, inclusion removal can be enhanced.[77-79)] Michelic et al.[77)] studied changes in Al_2O_3/CaO-Al_2O_3 inclusions on interaction with CaO-Al_2O_3 and CaO-Al_2O_3-MgO slags. They showed how initial alumina and calcium aluminate inclusions modify in presence of different slags. The inclusions in contact with the CaO-Al_2O_3-MgO slag showed the maximum modification. Inclusions were removed as a result of slag-entrapment with maximum entrapment in the CaO-Al_2O_3 slags.

1.3.4. Inclusion Entrapment by Refractory. Another method by which inclusions can be removed is attachment to the refractory walls in the ladle or the tundish. The steel in the ladle is in contact with the large surface area of the refractory walls to which inclusions can attach. Nozzle clogging is a known and widely studied problem faced in the steel industry which occurs due to the attachment of inclusions to the refractory walls in the nozzles.[80-82)] This attachment behavior of the inclusions to the refractory can be utilized to remove the inclusions by using flow control devices or filters in the tundish made of refractories which are prone to inclusion attachment.

Zhang et al.[64)] studied three-dimensional fluid flow in continuous casting tundishes with and without flow-control devices using water-modeling and computational fluid dynamics (FLUENT software) and used industrial experiment data for verification. They report that for smaller inclusions the adhesion removal is especially effective and

stronger stirring energy is favorable for the adhesion. Also, flow control devices provide surface for adhesion and improve inclusion adhesion to the walls and bottoms.

Sinha et al.[68] studied inclusion removal in continuous casting tundish taking the buoyancy, turbulent collision and adhesion to the solid surface into account. They reported that near the walls of the tundish the liquid steel velocities are low so the inclusions may move close and stick to the walls. The adherence of inclusions was more prominent along the longer walls and bottom of the tundish. Inclusions also adhere more to weirs than dams, and baffles provided the best results for inclusion removal than other flow control devices.

Kawawa et al.[83] measured the first order removal rate of inclusions in laboratory experiments using induction furnace and Tammann furnace in MgO, SiO_2, Al_2O_3 and CaO-20%CaF_2 crucibles with different deoxidizers. They showed that the crucible of a material having a higher chemical reactivity with primary oxide inclusions lead to a higher separation rate, confirming that inclusion separation by attachment to the refractory is a key process.

1.3.5. Gas Bubbling. Floatation of the inclusions in the ladle can be enhanced by bubbling gas into the ladle. Gas bubbles also provide an interface to which inclusions can attach and float out. Researchers have studied the optimal usage of gas bubbling into a ladle.

Single or multiple porous elements are used to purge inert gas such as argon into molten steel in the ladle.[84] The flow-rate of the gas is also very crucial and its effectiveness for inclusion removal has been studied by researchers.[85] Low gas flow rates can result in poor stirring and mixing; whereas, high gas flow rates can lead to emulsion between slag and metal and flushing-off of tiny inclusions from the refractory of the ladle wall.[85] Stirring energy as a function of gas flow rate can be expressed as[86]:

$$\dot{\varepsilon} = 14.23 \left(\frac{\dot{V}T}{M}\right) \log\left(1 + \frac{H}{1.48 P_a}\right) \quad (18)$$

where,

$\dot{V}$ = Ar flow rate at standard temperature and pressure in m^3/min

T = absolute steel temperature

M = steel mass in tonne

H = the total depth of the melt in m and P_a is in atmosphere.

Argon stirring in the ladle is applied to homogenize the steel, remove the impurities and reduce the number of non-metallic inclusions. The homogenization of steel is much faster compared to the removal of inclusions.[85] Ek et al.[85] studied inclusion removal for different argon flow rates using water model (0.15 m^3/h, 0.21 m^3/h, 0.36 m^3/h and 0.45 m^3/h) but did not observe any significant change in the inclusion

removal rate. A necessary condition for the separation of the inclusions from the steel bath to the slag is the direct contact between the inclusion and the slag.[85-89] Higher plume velocity brings more inclusion to the top per unit time but inclusions travelling along the horizontal slag-metal interface don't have enough time to separate.[85,87,88] As a result, smaller inclusions can return back to the metal bulk. The maximum number of inclusions that have the possibility to meet the slag per second depends on the size of the inclusions and the horizontal velocity of the liquid metal.[87] The fraction of inclusions brought into contact with the slag by the metal-gas plume is much higher than the fraction due to buoyancy.[87]

Researchers have also studied the optimal bubble size to remove inclusions both by fluid flow models and water modeling techniques.[89-91] Smaller bubbles appear to enable more inclusion removal for the same gas flow rate. Zhang et al.[91] used computational models to study inclusion removal by bubble floatation in continuous casting molds. They showed that bubbles smaller than 1 mm in diameter have high inclusion attachment probabilities (30 %), while that for bubbles larger than 5 mm the probability is less than 1 %.

1.3.6. Electromagnetic Stirring. Electromagnetic stirring (EMS) in the ladle, tundish and mold is utilized to homogenize steel and inclusion floatation.[92-97] Alexis et al.[94] observed that the induction stirrer results in high velocities close to the ladle walls. They recommended that high velocities close to the wall should be avoided to minimize refractory wear (ladle glaze removal) and hence non-metallic inclusions in the steel. The ladle age plays an important role for induction stirring as the ladle lining thickness decreases due to wear, making distance between stirrer and steel shorter.[94]

Ilegbusi et al.[95] studied the effect of electromagnetic force on inclusion removal in a tundish for different inclusion sizes (20 - 100 μm). They reported that electromagnetic fields minimize inclusion coalescence by minimizing turbulence but aids with floatation of larger particles.

It is common practice to use EMS technique in continuous casting strand. It causes the refinement of the solidification structure, reduction in inclusion content and improvement in the quality of the surface, sub surface and the inner structure of the cast products. There are three possible EMS applications in a continuous casting machine according to the position and the requirement of the cast products namely mold (M-EMS), secondary cooling zone (S-EMS) and the final solidification zone (F-EMS).[96] One or more EMS in combination is used depending upon the steel cleanliness requirement and cast product quality. It was reported by Glaws et al.[97] that EMS in the strand improves the steel cleanliness by lowering the total oxygen in the billet from 30 to 20 ppm.

1.4. INCLUSION MODIFICATION

Even though there are different ways to remove inclusions from steel, all inclusions cannot be removed. Inclusions floatation in steel is a function of inclusion size, chemistry and density. Solid inclusions behave differently than liquid inclusions. Further, liquid inclusions are known to cause fewer problems like clogging or strip breaks. Liquid inclusions agglomerate more easily to form larger inclusions. Researchers have pointed out that these issues (clogging) can be resolved even with a portion of the inclusion being either solid or semi-solid (< 70% solid).[98-101] According to Fuhr et al.[100], castability problems became more evident when the proportion of solid inclusions was higher than 60-70%. Pistorius et al.[101] suggested that clogging could be avoided if the inclusions contain more than 50% liquid.

The main objective of inclusion modification is to transform solid inclusions to liquid inclusions. In aluminum killed steel where solid alumina inclusions form as a result of de-oxidation, calcium treatment of the steel is practiced to transform them into liquid calcium aluminate inclusions.[98-102] Alumina inclusions are known to form clusters and cause nozzle clogging.[81] So, making them liquid enhances agglomeration and floatation, significantly reducing nozzle clogging.[36,81,98-102]

Pretorius et al.[98] showed that spinel inclusions can be modified by Ca treatment by preferential reduction of the MgO component of spinel to Mg in solution in steel. This is possible in low carbon aluminum killed steel where oxygen potentials are very low.[98] They also suggested that similar modification would not be possible in steels with higher oxygen potential like Si killed steels. Verma et al.[102,103] reported that spinel modification by Ca treatment can occur preferentially by reduction of MgO as well as some Al_2O_3

components. Formation of an initial CaS phase was also predicted for steel containing 45 ppm S.

Titanium addition to aluminum killed steel has also been studied to form aluminum-titanate inclusions.[104-106] For silicon killed steel, manganese additions are made along with silicon to aid in de-oxidation as well as form liquid manganese silicate inclusions instead of solid silica inclusions.[107-109] Thus, in thin-strip casting of steel, Si-Mn de-oxidation is used over aluminum de-oxidation. With titanium addition to Si-Mn de-oxidized steel, melting point of the inclusions can be further reduced.[110,111] Effect of titanium addition in Si-Mn de-oxidized steel has been presented in this work.

1.5. INCLUSION ENGINEERING

Tailoring non-metallic inclusions to achieve desired effect on steel properties is known as "inclusion engineering".[112] Inclusion engineering involves achieving specific de-oxidation inclusion composition, which are liquid at steelmaking temperatures and deformable during casting and further processing. Apart from the chemistry the control over population-density, size and distribution of inclusions in steel would define effective inclusion engineering. Further, it would involve utilizing the inclusion population for grain refinement and obtaining required microstructure using "oxide metallurgy".

For effective inclusion engineering the following information is required: (a) how inclusions form; (b) how they evolve during the steelmaking process; (c) whether the primary inclusions formed require modification and if so, how to modify them; (d) how to minimize inclusion population; (e) how to achieve a fine distribution of inclusions in the final product; and (f) how inclusions would influence the properties of the final product.[112,113] The type of inclusions varies with steel chemistry and further different type of inclusions can be formed in the same steel grade depending on different practices. An understanding of the effect of each type of inclusions on the properties of steel to determine the most desirable inclusion in a given product is required. With this knowledge adjustments in the process parameters can be made to obtain these inclusions. With good control of ladle steelmaking practices specific de-oxidation inclusion compositions can be achieved.

1.6. INCLUSIONS IN Mn-Si KILLED STEEL

There are primarily three deoxidizers used in steelmaking: aluminum, silicon and manganese.[15] Out of these, Al is the strongest deoxidizer and results in solid – Al_2O_3 as the primary inclusion at 1600°C. Mn is the weakest deoxidizer resulting in Mn(Fe)O inclusions which can be liquid or solid at 1600 °C depending on the Mn content of steel. Deoxidation by Si is much more effective than Mn and results in solid SiO_2 inclusions. However, simultaneous deoxidation by Mn and Si gives much lower dissolved oxygen in steel and liquid MnO-SiO_2 based inclusions. The equilibrium relation for Mn-Si deoxidation can be represented by the following reaction[15]:

$$[Si] + 2(MnO) = (SiO_2) + 2[Mn] \quad (19)$$

$$K_{MnSi} = \left(\frac{[\%Mn]}{a_{MnO}}\right)^2 \frac{a_{SiO_2}}{[\%Si]} \quad (20)$$

The activity of silica in manganese silicate (in case of Mn-Si deoxidation) is lower than solid silica (in case of Si deoxidation) which drives the oxidation reaction in the forward direction resulting in lower dissolved oxygen. The deoxidation product for Mn-Si deoxidation is either liquid manganese silicate or solid silica (Figure 1.2). For liquid steel with Mn > 0.4%, MnO-rich silicate is the deoxidation product in Mn-Si deoxidized steel for low Si concentrations (Figure 1.2 (a)). Figure 1.2 (b) shows the effect of temperature on the deoxidation product as a function of Mn and Si concentration in Mn-Si deoxidized steel.[15,57]

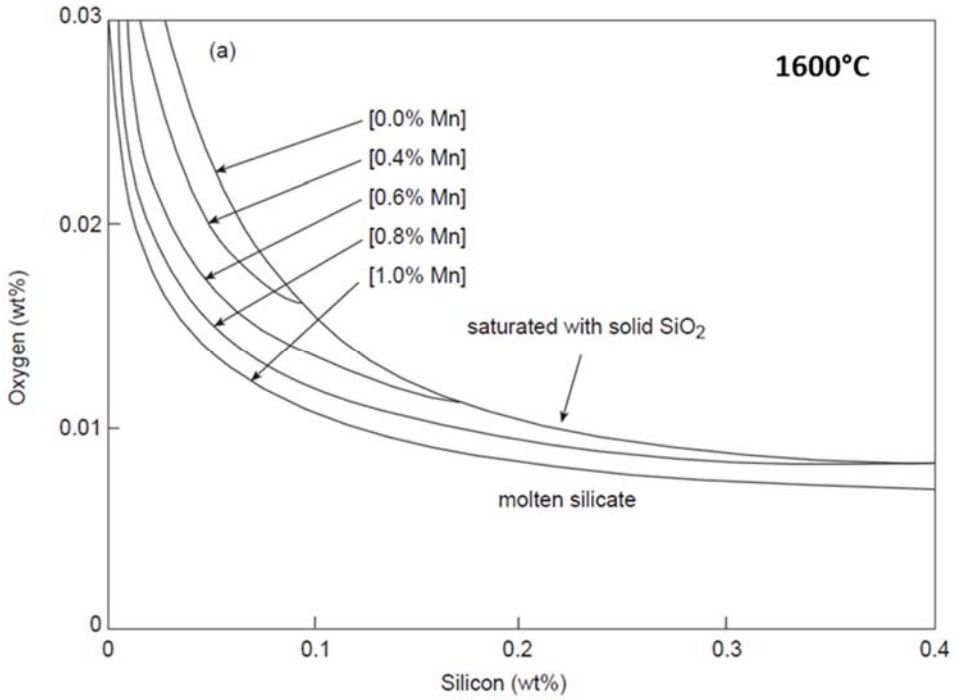

(a)

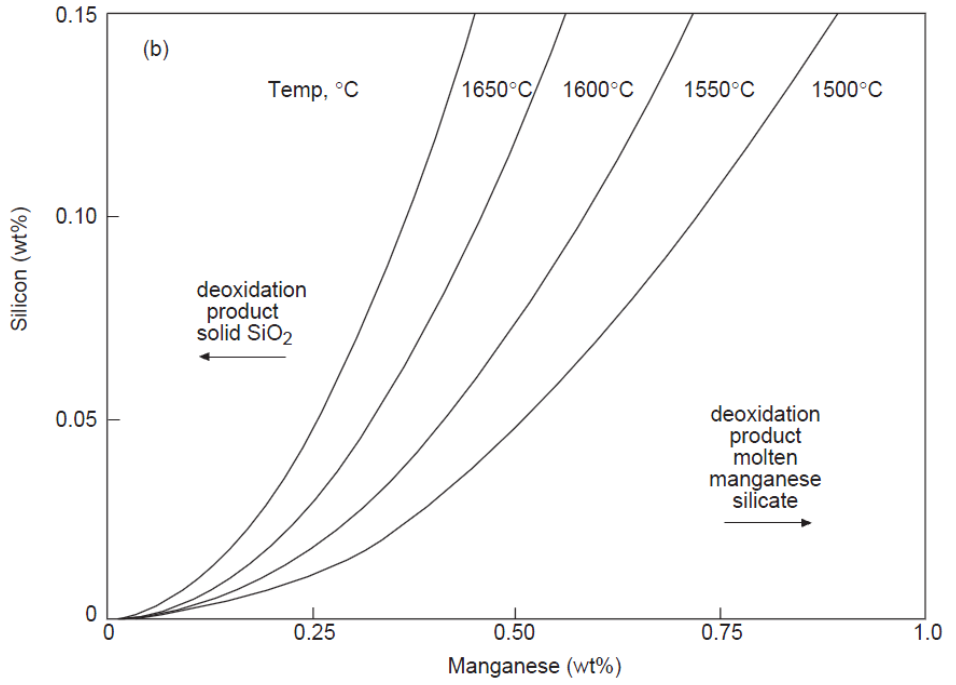

(b)

Figure 1.2. Equilibrium relations for deoxidation of steel with Si and Mn[15,54)]

MnO-SiO_2-Al_2O_3 system is one of the most important systems for the study of inclusions in modern steel type.[114] Inclusions in Si-killed steels belong to this system. As the ferro-alloys used for Mn-Si de-oxidation (ferro-manganese, ferro-silicon and silico-manganese) contain some amount of Al, the inclusions have significant Al_2O_3 content.

Inclusions of different compositions from the MnO-SiO_2-Al_2O_3 system have been observed in Si-killed steel. Corundum (Al_2O_3) inclusion are solid at steelmaking temperature (melting point 2050°C) and very hard (Micro-hardness 3000-4500 Kgf/mm^2).[113] The primary oxide inclusion for Si-deoxidation (Cristobalite SiO_2) has a lower melting point (1723°C) and hardness (Micro-hardness 1600 Kgf/mm^2).[113] SiO_2 is also observed as layer around inclusions of iron and manganese oxides. These inclusions are believed to be formed due to reduction of FeO/MnO at the surface by Si in steel (Hultgren's mechanism).[113,114] This behavior was also observed in the author's work. Primary oxide for Mn-deoxidation (Manganosite, MnO) is also solid at steelmaking temperature (melting point 1850°C) but is softer (Micro-hardness 400 Kgf/mm^2).[113] These inclusions form solid solution with FeO and are generally observed as $Fe_XMn_{1-X}O$. Pure MnO only exists in high Mn containing steel. Galaxite ($MnO \cdot Al_2O_3$) inclusions have spinel type structure and are considered to be harmful due to their hardness (Micro-hardness 1500-1700 Kgf/mm^2).[113] The melting point of $MnO \cdot Al_2O_3$ is 1560°C and these inclusions solidify before casting. Mullite ($3Al_2O_3 \cdot 2SiO_2$) inclusions have a comparable hardness (Micro-hardness 1500 Kp/mm^2) but a higher melting point (1850°C). The MnO rich inclusions in the MnO-SiO_2-Al_2O_3 system are softer and have much lower melting points. Rhodonite ($MnO \cdot SiO_2$) inclusions solidify at 1291°C and have micro-hardness

around 750 Kgf/mm^2.[113] Similarly, for Tephorite ($2MnO \cdot SiO_2$) the melting point is 1345°C and micro-hardness is around 950 Kgf/mm^2.[113] With presence of some Al_2O_3 in the inclusions the melting point drops even further. For Spessartite ($3MnO \cdot Al_2O_3 \cdot 3SiO_2$) the melting point is around 1195 °C and micro-hardness is around 1000-1100 Kgf/mm^2.[113,115,116] Mn-anorthite ($MnO \cdot Al_2O_3 \cdot 2SiO_2$) and Mn-cordierite ($2MnO \cdot 2Al_2O_3 \cdot 5SiO_2$) inclusions exist only with some amount of calcia.[114] Roghani et al.[117] studied MnO-SiO_2-Al_2O_3 melts containing up to 30 wt. % Al_2O_3 and measured liquidus temperatures between 1075°C to 1245°C.They reported melting temperatures for Mn-cordierite ($2MnO \cdot Al_2O_3 \cdot SiO_2$) and Mn-anorthite ($MnO \cdot Al_2O_3 \cdot 2SiO_2$) as 1175°C and 1130°C, respectively. Different inclusion compositions are shown in the MnO-SiO_2-Al_2O_3 phase diagram (Figure 1.3). The dotted lines mark the boundary with MnO/SiO_2 mass ratios of 0.5 and 2. These lines mark the boundary of the Spessartite region (lowest melting point region) at 1200°C. This composition range is targeted to achieve glassy inclusions in solid steel.[118]

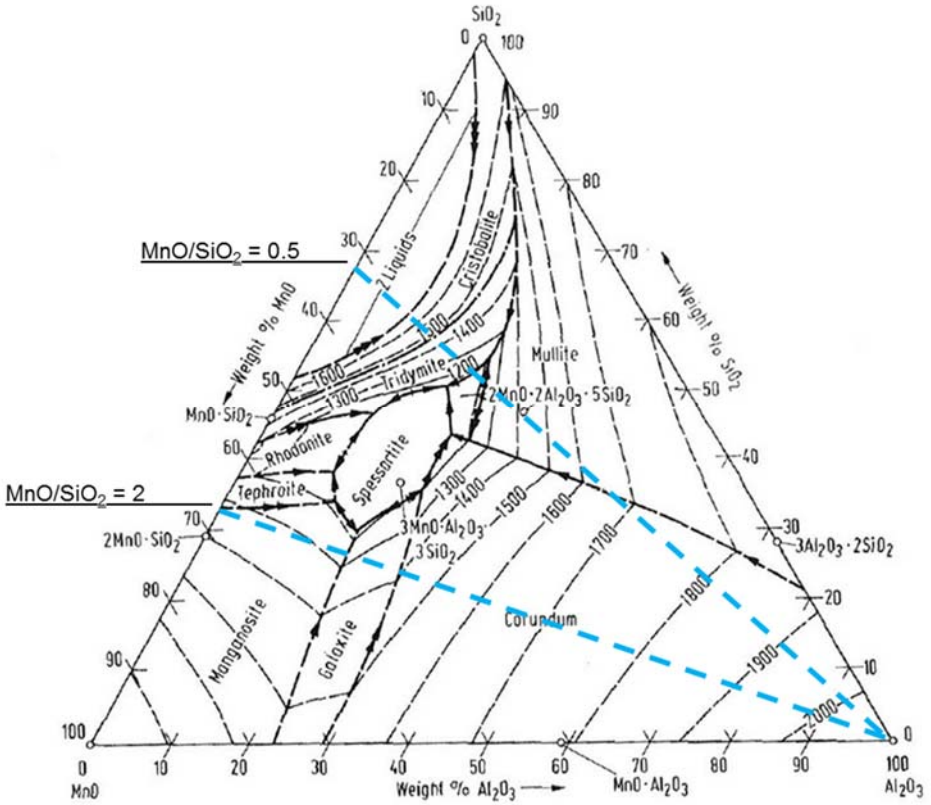

Figure 1.3. MnO-SiO_2-Al_2O_3 system[116)]

The MnO and SiO_2 content in the inclusions has a direct relation with Mn:Si ratio of the steel. Kiessling[114)] reported that for Mn:Si ratio of steel between 17 to 1.9 the corresponding MnO:SiO_2 ratio in inclusions is 1.7 to 0.47 respectively. Kang et al.[118)] performed thermodynamic calculation and found that inclusions with low liquidus temperature and a deformable phase on cooling can be obtained when the steel chemistry is controlled in the range of [Mn] + [Si] = 1 wt.% and [Mn]/[Si] = 2-5. This relation is shown in the Figure 1.4.

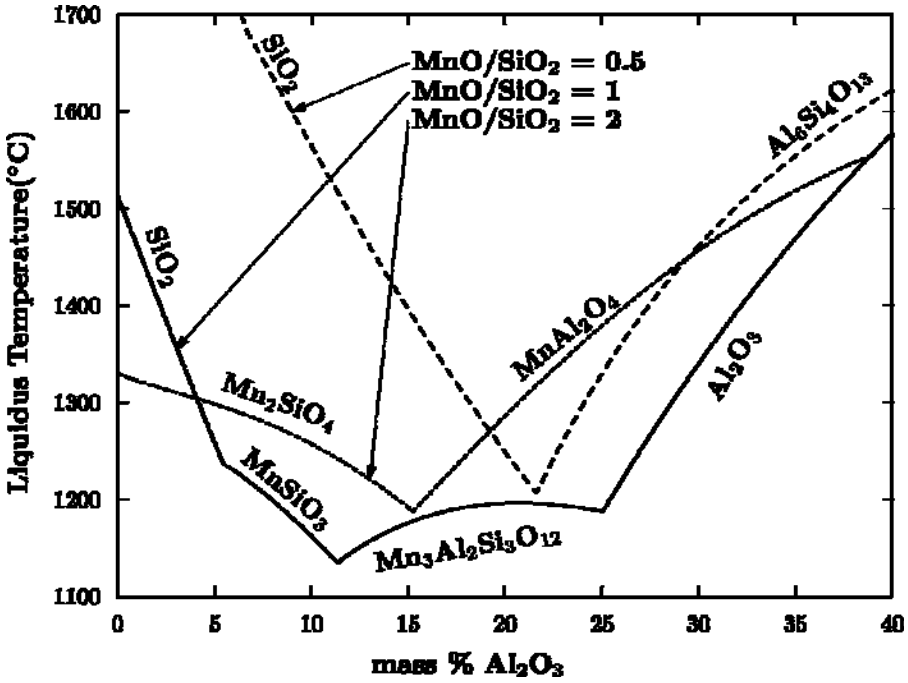

Figure 1.4. Liquidus temperatures in $MnO–SiO_2–Al_2O_3$ system as a function of Al_2O_3 concentration for MnO/SiO_2 ratios 0.5, 1.0 and 2.0[117)]

Inclusions rich in Al_2O_3 have a higher melting point compared to those with low Al_2O_3 content. Roghani et al.[117)] reported that for mixtures containing $MnO:SiO_2$ weight ratios between approximately 0.3 and 0.7, the liquidus temperatures decrease for Al_2O_3 concentrations less than 25 wt. % and any further Al_2O_3 additions resulted in increases in the liquidus temperature.

In tire-core production, wire-breakage is a frequently occurring problem in the presence of solid alumina inclusions. Therefore, Mn-Si de-oxidation is used for wire making process which results in deformable liquid $MnO-SiO_2$ inclusions.[112)]

Similarly Mn-Si de-oxidation is preferred for spring and bearing steel where extremely long fatigue life is required, which is severely decreased by alumina inclusions.[112)]

For near net shape casting, where section reduction during rolling is too small to cause sufficient microstructural refining, grain refinement by inclusion engineering is achieved by de-oxidation products of Mn-Si de-oxidation. For thin strip casting at Castrip, Mn and Si contents of the steel melt are controlled within certain limits (Mn > 0.55 wt. % and Si between 0.15-0.35 wt. %).[2,11] This composition is also chosen to ensure that liquid inclusions of MnO and SiO_2 are present during casting. This also helps to avoid clogging and to increase the rate of interfacial heat transfer.[11]

1.7. SCOPE OF WORK

In this work, inclusion-formation in their early stages has been studied. Inclusions first form during de-oxidation. Inclusion formation as a result of ferro-silicon and ferro-manganese addition, which are the de-oxidizers used in silicon killed steel, has been studied. Ferro-alloy particles were dissolved in a controlled volume of steel using a ceramic sampler. This was followed by air-cooling of the steel in the sampler to quench inclusions in their early stage of formation and evolution. During ferro-alloy dissolution the concentration inhomogeneity of the alloying element in steel resulted in inclusions of varying chemistry. Ferro-silicon with 75% silicon (Fe75Si), low carbon ferro-manganese (FeMn) and a combination of both were used in this study. The procedure and results of this study have been described in detail in chapter 3. The supporting data for inclusion analysis has been presented in Appendix A. The supporting calculation for solidification of the steel in the sampler has been described in Appendix B.

Inclusions formed in Mn-Si killed steel as a result of Fe75Si and FeMn additions were transformed by adding ferro-titanium (FeTi) to the steel. Different amounts of FeTi were added to the steel to study the extent of inclusion modification. Inclusion modification with time was evaluated by analyzing steel samples taken from the experimental crucible at different time intervals after each FeTi addition. In Appendix C an example of MnS precipitation on titanium-oxide inclusion is presented.

A dynamic model for vacuum tank degasser (VTD) was developed to study reactions in the VTD using METSIM software and FactSage macros. VTD is a key operation used in thin strip casting to achieve low levels of oxygen, hydrogen and nitrogen required for the process. A brief introduction to FactSage macro programming has been provided in Appendix D.

PAPER
I. TRANSIENT INCLUSION FORMATION AND EVOLUTION IN SILICON-KILLED STEELS

Vivek Thapliyal

Abhishek Kumar

David G. C. Robertson

Jeffrey D. Smith

Materials Science and Engineering

Missouri University of Science & Technology

Rolla, MO

Phone - 573-341-6469,

E-mail – vtty6@mst.edu

Published in Ironmaking & Steelmaking

ABSTRACT

Transient inclusion formation in low-carbon silicon-killed steel as a result of ferroalloy additions of ferro-silicon (Fe75Si) and ferro-manganese (FeMn) (for de-oxidation and alloying) was studied in the laboratory using a novel experimental technique. Inclusion chemistries and morphologies were analyzed using automated scanning electron microscopy (ASPEX). Formation of these inclusions was studied using thermodynamic software (FactSage) and a mechanism was proposed. Effect of solute concentration gradients during alloy dissolution and mixing was observed. Inclusions which formed initially, at low concentrations of ferro-alloy, were liquid phase with a high concentration of FeO. Depending on the ferroalloy addition, initial inclusions become richer in SiO_2 or MnO. Inclusions also underwent further phase transformations on cooling.

Key Words: transient; inclusions; ferro-alloy dissolution

1. INTRODUCTION

With recent developments of new steel grades, steel cleanliness has become increasingly important. The presence of inclusions represents a formidable challenge for achievement of the required properties of such steel. Inclusions originate from indigenous or exogenous sources. Indigenous inclusions form as a result of de-oxidation reactions, alloy additions, re-oxidation reactions and solute segregation during the casting process.[1-3] Exogenous inclusions enter steel from the slag or the refractory materials used during the steelmaking process.[3-5]

De-oxidation reactions and alloying additions are considered to be the primary sources of inclusions. When Al and ferro-silicon are used as deoxidizers under equilibrium conditions primary oxide inclusions of Al_2O_3 or SiO_2 would be expected. But inclusions observed after de-oxidation are frequently complex chemistries with variable composition. Impurities in the ferroalloys and other components in steel are the major contributors to this behavior. The effect of such impurities on inclusion formation has been studied by a number of researchers[6-8] and it is out of scope of this study.

In silicon-killed steel, ferro-alloys (Fe75Si, FeMn, etc.) are used as alloying additions as well as de-oxidizers. Different ferro-alloys follow different dissolution (melting) paths, which have been described in detail by Argyropoulos et al.[9,10]. Ferro-alloys with lower melting points than steel immediately form a solid steel shell around the ferroalloy lump upon immersion. The ferro-alloy lump then melts, followed by the melting of the outer steel shell. In this paper, the word ‘dissolution’ will be used to describe the above process. In normal practice ferro-alloys are primarily added as lumps of different shapes and sizes. The time required for dissolution depends on the size of the

ferro-alloy particles as indicated in a study by Lee et al.[11]. The diffusion and micro-scale mixing of the alloying element takes place after dissolution. For ferro-alloys with melting points greater than the steel, the solidified steel shell melts after some time and the solid ferroalloy particles take a much longer time to react.

Researchers have studied the macro-scale mixing (homogenization) of steel in ladles due to argon purging or electromagnetic stirring.[12-14] It has been reported that the time required to homogenize the steel in a ladle after ferro-alloy addition is about 1-4 minutes depending on the gas flow rate or stirring power.[12,13] During this homogenization period, local steel chemistry can be significantly different than the final expected bulk chemistry. Inclusion formation will take place at locations with high concentrations of alloying elements and oxygen. These inclusions will have a range of composition depending on the local chemistry. Most inclusion will further transform during the steel-making process and may therefore be considered as transient inclusions. Understanding the formation and evolution of inclusions composition and microstructure can be of significant importance for the steel industry.

Studies of inclusion formation immediately after the addition of Al as a deoxidizer and subsequent evolution with time have been investigated.[15,16] These studies suggest that diffusion of oxygen is the key mechanism for inclusion growth. Experiments were set-up utilizing Fe-Al diffusion couples to identify the reaction mechanism at the Fe/Fe-Al interface.[17,18] It has been proposed that large angular Al_2O_3 inclusion form due to heterogeneous nucleation of Al_2O_3 on FeO_x inclusions after reduction by Al.
In this work, a new technique was developed to study the evolution of inclusion formation in low alloyed Si/Mn de-oxidized steel. An experimental procedure was

designed to study inclusion formation immediately after deoxidizer addition and prior to macro-mixing/homogenization. Additions of ferro-silicon, ferro-manganese and a combination of both were made to steel to study the formation and morphology of the transient inclusions.

2. EXPERIMENTAL PROCEDURE

Experiments were conducted to study the effect of ferroalloy dissolution and micro-mixing on formation of inclusions. For these experiments, samplers were fabricated as shown in Figure 1, using a plastic ball of diameter 40 mm, to which styrofoam sections were attached to function as metal inlet and gas vent. To this arrangement, ceramic coatings of silica and zircon were applied. These coatings were dried for 48 hours before firing at 1173 K for 2 hours. After firing, the samplers had a hollow spherical cavity of diameter 4 cm, with metal inlet and gas outlet of 1 cm by 1 cm cross-section.

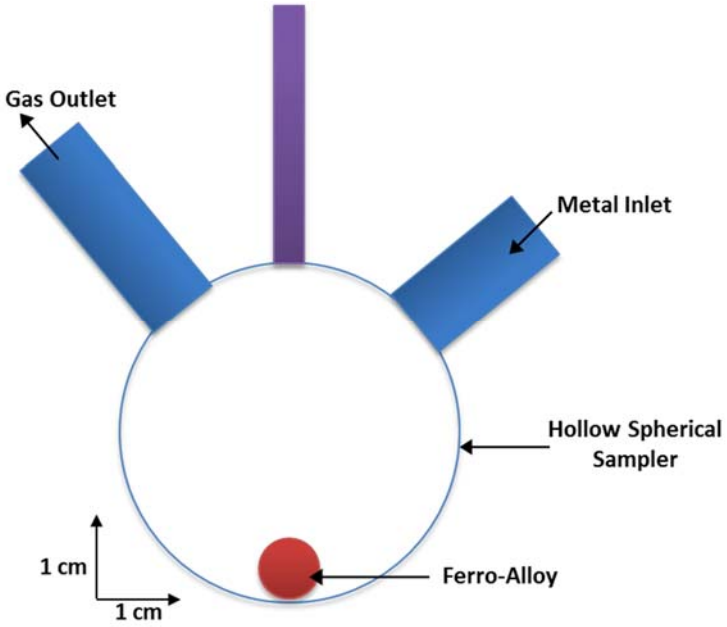

Figure 1. Schematic diagram of the samplers used for dissolution studies

Ferro-alloys are typically added to steel at a ratio on the order of 1:100 (10 kg/tonne). The amount of ferro-alloy added depends on the oxygen content of steel and the target steel chemistry along with a recovery factor. In this work, a much smaller volume of steel (as compared to the ladle) was used to replicate the industrial process with a higher ferroalloy to steel ratio (1:50). This was done to cover the range of chemistry variation that can be expected during the dissolution and micro-scale mixing period in the ladle after ferroalloy addition. Keeping the ferroalloy/metal ratio high and the solidification time short effectively quenches in the early stage inclusion compositions that would presumably evolve to different compositions in a ladle with lower Si or Mn in the steel. Any stable inclusions formed at this stage could also serve as heterogeneous nucleation (and growth) sites for subsequent inclusion phases.

Ferro-alloy pieces of maximum dimension approximately 20 mm for Fe75Si and 10 mm for FeMn, with a weight of 5 gram were added to the sampler before filling with steel. Table 1 shows the composition of the ferroalloys added for these experiments. Three types of additions were made a) 5 gram ferro-silicon; b) 5 gram ferro-manganese and c) 2.5 gram ferrosilicon + 2.5 gram ferro-manganese.

Table 1. Composition of ferro-alloys added

Wt %	C	Si	S	Mn	P	Ca	Al	Fe
Fe75Si	<0.1	73-78	<0.02	-	<0.04	<0.6	<1.5	<27
FeMn	0.078	0.28	0.025	97.08	0.026	-	-	2.5

The sampler was dipped into a crucible containing liquid steel, at 1873 K, under induction heating. The crucible size was 10 cm internal diameter and 20 cm height containing 7 kg of liquid steel. An inert atmosphere was maintained during the experiments by blowing argon at the rate of 1 lit/min over the liquid steel in the crucible to minimize oxidation.

The initial chemistry of the steel added to the sampler is shown in Table 2. After the sampler was filled with liquid steel, it was taken out of the crucible and air cooled. A filled sampler contained 240 gram of steel.

Table 2. Initial steel chemistry

Elements	Fe	C	Si	S	Mn	P	Cu	Cr	Al
Wt.%	99.65	0.05	0.07	0.0060	0.17	0.00	0.00	0.01	0.00

Figure 2 shows the sequence of events that presumably takes place in the sampler during the experiment. A similar dissolution mechanism was described by Argyropoulos[9]. The steel inside the sampler will solidify faster close to the edges as compared to the center. Solidification will gradually progress towards the center. Ferro-alloy particles will undergo dissolution and then micro-mix in the liquid steel. All these processes compete with each other to provide for different composition and solidification environments for inclusion formation and evolution. Further, inclusions will continue to undergo phase transformation even after all the steel has solidified.

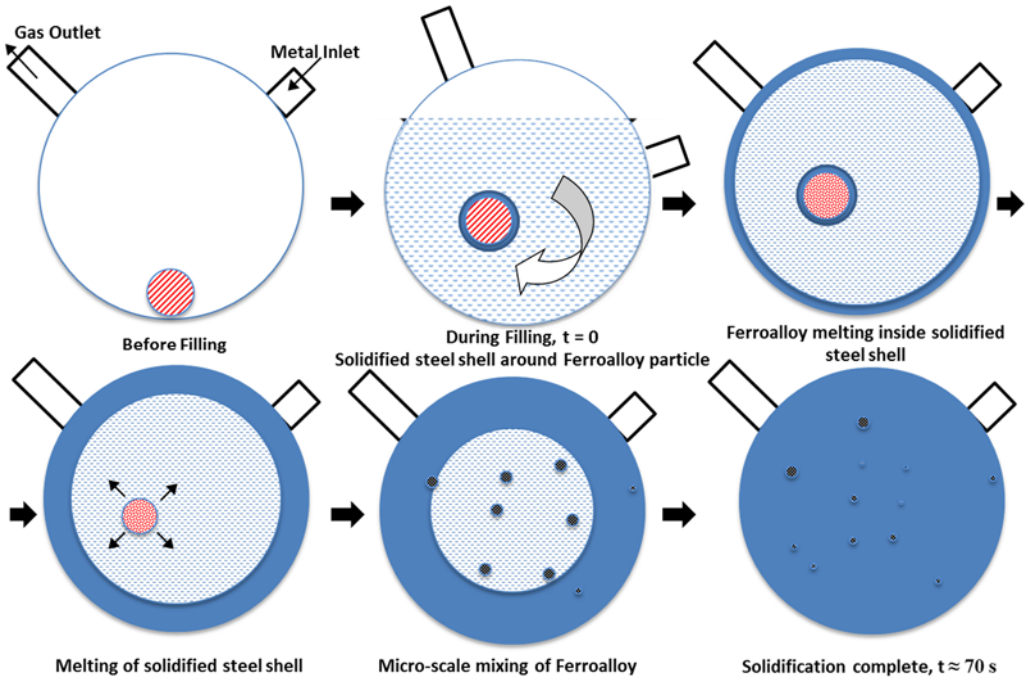

Figure 2. Schematic diagram showing the dissolution/diffusion sequence expected inside the sampler for a ferro-alloy lighter than steel

As the sampler is dipped into liquid steel, a layer of steel solidifies outside the ceramic shell as shown in Figure 3. Based on the properties of the steel and the ceramic

shell (Table 3), the time required for the steel to completely solidify inside the sampler was estimated to be about 70 seconds.

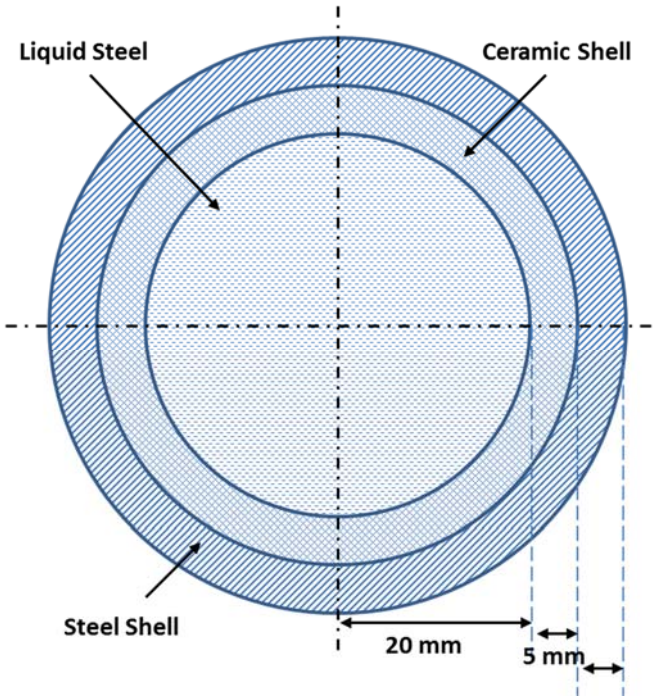

Figure 3. Representation of the sampler volume used for the solidification time calculation

The solidified spherical steel ball obtained from the sampler was cut along the center in the vertical direction. The inclusion distribution across this cross-section was studied using automated scanning electron microscope (ASPEX). Inclusions were analyzed for size, shape, number-density and composition variation across the cross-section. Samples were analyzed using arc spectroscopy for chemistry variation of the steel. Total oxygen content in steel was measured using a Leco oxygen analyzer.

Table 3. Data used for solidification calculations[5)]

	Liquid steel	Ceramic shell	Solid steel
Thermal Conductivity (W/m.K)	43.095	3.5	34.518
Heat Capacity (J/kg.K)	729.96 + 0.03T	1500	384.95 + 0.18T
Density (kg/m^3)	7050	2020	7268
Heat of Fusion for Steel (J/kg)		246557	

3. THERMODYNAMIC MODELING OF STEEL-INCLUSION SYSTEM

For this study, complete equilibrium cannot be achieved in the reactor volume due to the insufficient time available for diffusion and mixing. Inclusions of different composition and morphology would form depending on the local concentration and solidification time. Modeling all the inclusion chemistries in the current reactor model requires detailed thermodynamic approach and will be a part of further study. In this work, inclusions formed in steel assuming overall equilibrium was calculated and their solidification was modeled. The inclusions formed as a result of these calculations were compared to the inclusions observed in the steel. Thermodynamic software FactSage 6.4[19)] was used to model inclusion formation and evolution for different ferro-alloy additions. The expected equilibrium inclusion compositions were predicted using the "Equilib" module of FactSage, considering the steel, slag, solid-solutions, and all possible liquids, solids and gases as the possible phases. The databases used in this study were: FSstel (compound and solution database for steel), FactPS (gas species, solid and liquid compound database) and FToxid (compounds and solutions for oxide databases). These calculations were carried out for the three types of ferro-alloy additions.

4. RESULTS AND DISCUSSIONS

Chemical analysis of the steel was performed across the sampler cross-section and a range of values was obtained for Si and Mn content. The results obtained are presented in Table 4.

Table 4. Chemical analysis result (wt. %) after dissolution experiment for different ferro-alloy additions

Ferro-alloys	C	Si	S	Mn	P	Fe	Al	Total O
Fe75Si	0.07	0.81-0.87	0.01	0.05	0.04	98.50-98.90	0.001	0.254
FeMn	0.05	0.03-0.08	0.01	0.67-8.88	0.01	90.93-99.03	0.001	0.228
FeMn+Fe75Si	0.03	0.38-0.45	0.01	0.80-1.20	0.04	98.17-98.60	0.001	0.139

Other residual elements like P, S and Al were also observed in the steel. These elements were found in trace amounts in the inclusions. Amount of manganese showed the maximum variation indicating that FeMn dissolution was not complete. The spectroscopy results showed Mn content as high as 8.88 %, which is much higher than the expected Mn content (~2%) after complete dissolution and mixing. Un-dissolved FeMn particles were observed in the microscopic analysis (Figure 9 (b)).

In automated SEM-EDS analysis, an area of 250 mm^2 was scanned to count up to 20,000 inclusions for each sampler cross-section. The analysis was performed at 2000X magnification with 0.5 μm as the minimum inclusion size. The total scanned area was divided into 'fields' of dimensions 80 μm by 80 μm that were analyzed in a randomized order. The analysis continued until either the maximum particle count was reached or the complete area was scanned. The weighted average of inclusion composition was calculated using the following equation

$$WeightedAverage\ \%\ Y = \frac{\sum_{field} inclusionarea \times \%Yininclusion}{\sum_{field} inclusionarea} \quad (1)$$

where, Y represents any elemental constituent of the inclusion.

Effects of ferro-alloy dissolution on inclusion evolution were studied using inclusion size and composition measurements from the SEM-EDS analysis. For compositional analysis, inclusions greater than 2 μm were considered in order to minimize the effect of matrix contribution. From the inclusion analysis data, the composition variation of inclusions per mm along the height and the width was calculated using the weighted average formula (equation 1).

Prior to the dissolution studies, a steel sample was acquired using an empty reactor volume (sampler) to identify the type of inclusions present initially in the steel. Typical inclusions observed in the sampler before any additions are included as Figure 4. Most of these inclusions were FeO-MnO-SiO_2 based liquid inclusions with about 6% (± 3) SiO_2 and 10% (± 4) MnO.

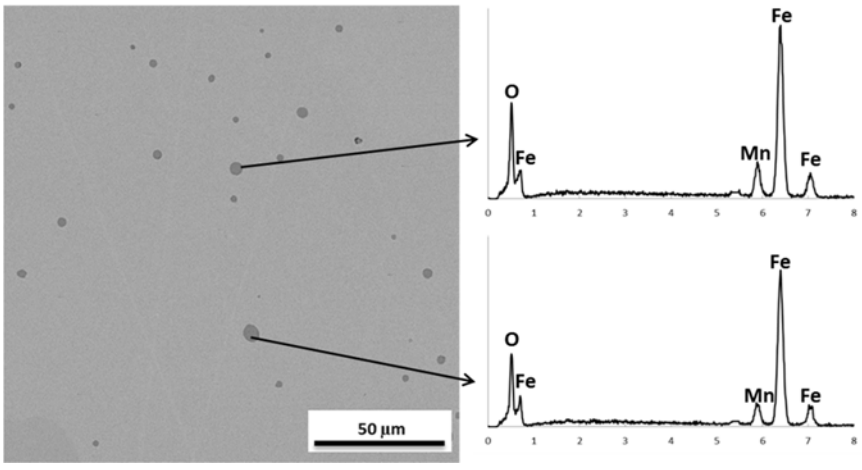

(a) FeO-MnO based inclusions

Figure 4. Types of inclusions observed before the ferro-alloy addition

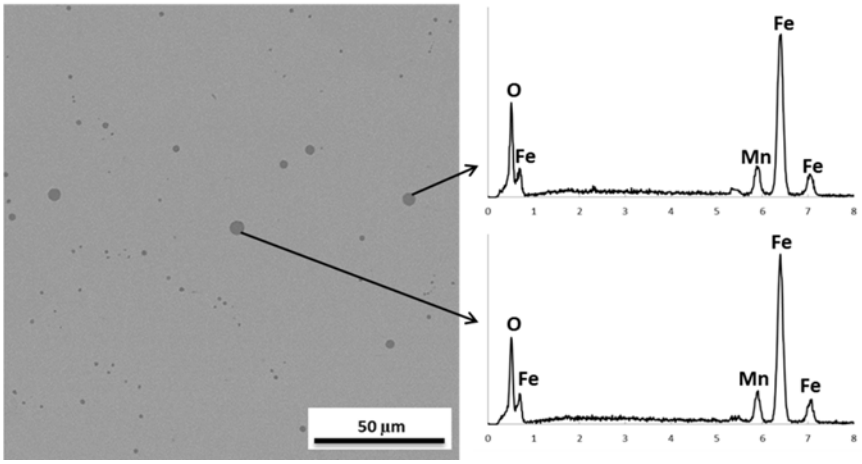

(b) FeO-MnO based inclusions

Figure 4. Types of inclusions observed before the ferro-alloy addition cont.

4.1. Type 1: Fe75Si Addition

When steel flows into the sampler through the metal inlet (Figure 1 and Figure 2), the Fe75Si pieces sitting at the base of the sampler presumably rose in the steel due to a lower density compared to steel. The flow of liquid steel will have some effect on their motion. As Fe75Si particle comes in contact with liquid steel a shell of solidified steel forms. The Fe75Si particle, having a lower melting point (1589 K (1316ºC)[11]) than steel, melts internally. As soon as the outer steel shell melts the diffusion and micro-scale mixing process begins. The silicon from the ferro-alloy reacts exothermically with the steel[11], which accelerates the dissolution process. The following exothermic reactions can be expected during the dissolution,

$$x\,Fe + y\,Si = Fe_xSi_y \quad (2)$$

$$Si + 2[O] = SiO_2 \quad (3)$$

About 5 gram of Fe75Si was added to 240 gram of steel, which would result in a final composition of 1.5% Si by weight on complete dissolution. At this composition, the silicon should completely dissolve in the steel which was verified by the absence of any un-dissolved particles. However, the measured chemistry (Table 4) was less than expected due to overflow of the steel out of the gas outlet of the sampler during filling. A change in the steel chemistry (Si up to 0.2% and Mn up to 0.05%) in the ladle was observed after the experiment. The particles observed in the sampler due to Fe75Si dissolution were mainly oxide inclusions with an average chemistry shown in Table 5.

Table 5. Average SiO_2 and FeO concentration in inclusions (wt. %) formed after Fe75Si dissolution and micro-mixing. Other components (CaO, Al_2O_3, MnO and S) were less than 2%.

Size range	SiO_2	FeO
2 -3 μm	23 ± 8	76 ± 5
3 - 5 μm	34 ± 12	64 ± 7
5 - 10 μm	44 ± 14	54 ± 9
>10 μm	49 ± 17	48 ± 10

The FeO to SiO_2 ratio in the inclusions decreases strongly with increasing size. A possible explanation is that the smaller inclusions formed first at higher oxygen potentials and so the FeO-SiO_2 phase was richer in FeO. Since the inclusions are two-phase (solid SiO_2 and FeO-SiO_2 slag), this may reflect a higher fraction of solid SiO_2 in the inclusions.

To minimize the matrix effects, composition was only measured for inclusions over 2 μm in size. For these inclusions, the average composition varied between 18-35% of Si (Figure 5). In the vertical direction, larger inclusions with higher average Si content

(~30-35%) were observed close to the bottom as the ferro-alloy dissolution started at that location. Further along the vertical direction, the average Si content and size was more consistent. In the horizontal direction, the inclusion Si content was observed to be highest close to the center and dropped gradually along the edges (Figure 5 (b)). Ideally this maximum should have been at the center of the sampler but the direction of flow of steel into the sampler presumably caused the shift observed.

The average diameter variation of the inclusions was studied across the cross-section for the full range of inclusion sizes (Figure 5). Most of the inclusions (~70%) were less than 2 μm in diameter throughout the sampler volume. So, the standard deviation shown was due to the presence of large inclusions. Therefore, while plotting these graphs, the standard deviation was shown only in the positive direction. It was observed that the average inclusion size varied between 1.5 – 2.5 μm with maximum value close to the bottom-center in the sampler (Figure 5). This location of the maximum value could be the starting point from where the micro-mixing begins, giving the longest time for growth. At the edges, the inclusions observed were smaller in size (< 2.0 μm) where the steel came into contact with the cooler refractory surface and solidified faster than the remaining steel in the sampler. Figure 6 shows some inclusions observed in the sampler.

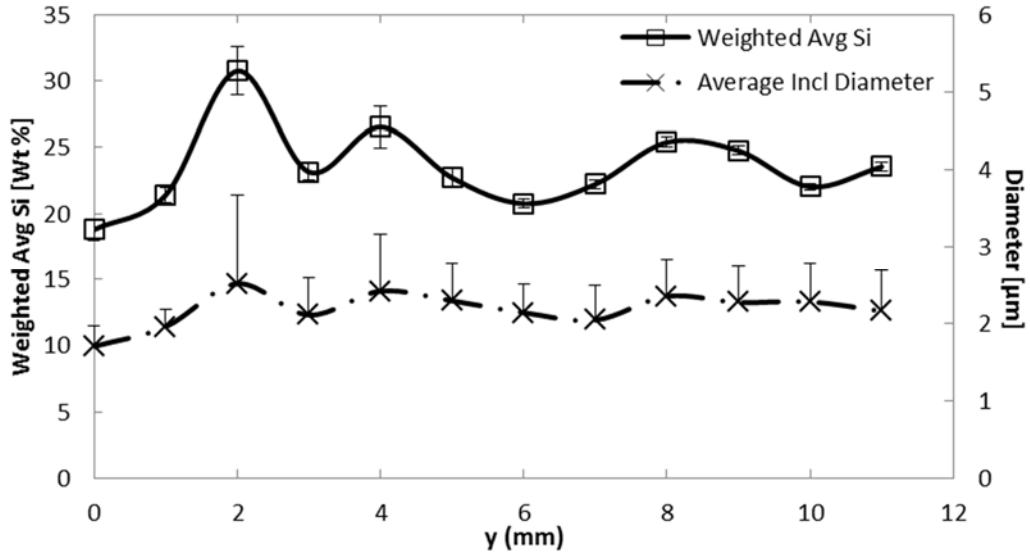

(a)

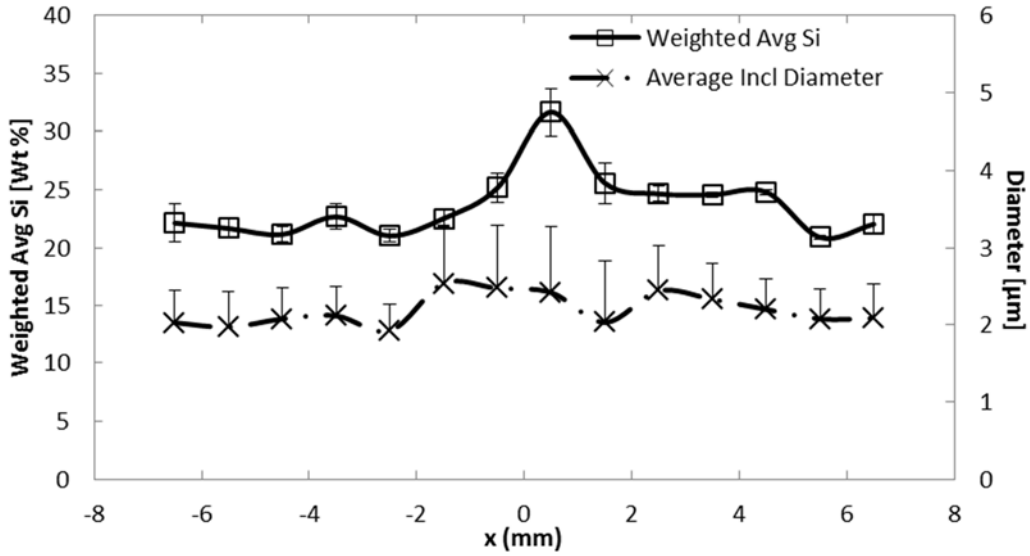

(b)

Figure 5. Results of inclusion analysis across the spherical sampler cross-section after Fe75Si dissolution. Inclusion Si content (for >2.0 µm) and diameter variation (for inclusions of all sizes) along the a) vertical and b) horizontal dimension of the sampler.

Theoretically, for a Fe75Si particle in the steel, a local maximum concentration of 75 wt. % Si can be achieved. However, as the particle dissolves this maximum decreases.

The final Si concentration achieved is about 0.9 wt. % (Table 4). Equilibrium calculations can be performed for all the local concentrations to predict which inclusions are expected. Thermodynamic predictions, with expected steel chemistry after Fe75Si addition and assuming complete homogenization, showed the formation of predominantly SiO_2 (solid) with some liquid phase inclusions at 1873 K. These liquid phase inclusions were predicted to have SiO_2 (~70%) with Al_2O_3 (<10%), FeO (3-5%) and MnO (3-5%) as the significant minor components. Majority of the inclusions were observed with this liquid phase within SiO_2 inclusions (Figure 6 (a) and Figure 6(c)). Also, as the temperature drops, cristobalite (SiO_2) phase precipitation was predicted within the inclusions. An example of this can be seen in Figure 6 (a), where the SiO_2 rich dark phase precipitated in a glassy slag matrix. Further decrease in temperature would lead to the precipitation of mullite ($3Al_2O_3.2SiO_2$) at 1759 K and pure iron (Fe) precipitation at 1738 K. An example of Fe precipitation was observed as white globules in a slag matrix (Figure 6 (c)). The equilibrium calculations also showed the presence of stable liquid slag phase even at low temperatures (< 1673 K) resulting in rounded inclusions. Liquid inclusions with varying FeO-SiO_2 content were also observed in the analysis. The evolution of these inclusions can be observed in Figure 7.

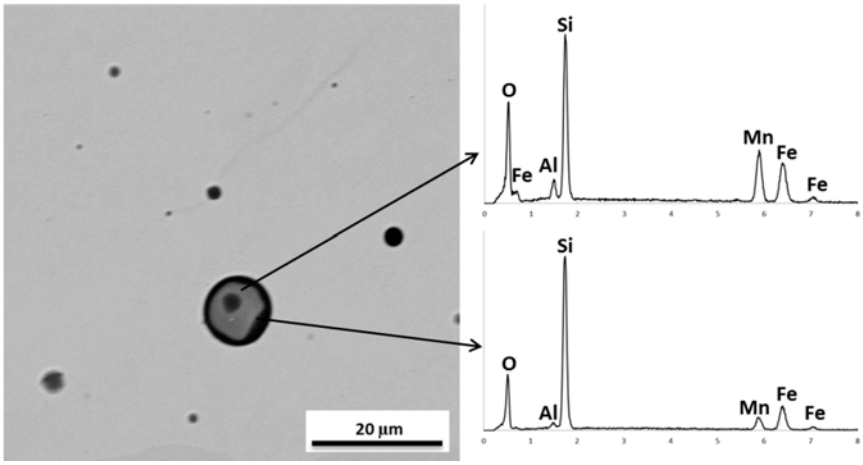

(a) Liquid phase (SiO_2-MnO-FeO-Al_2O_3) within SiO_2 inclusion

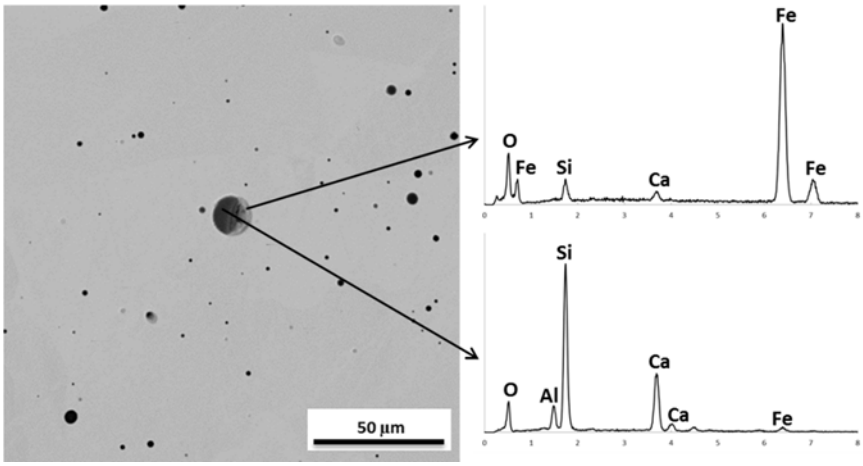

(b) High FeO within SiO_2 inclusion

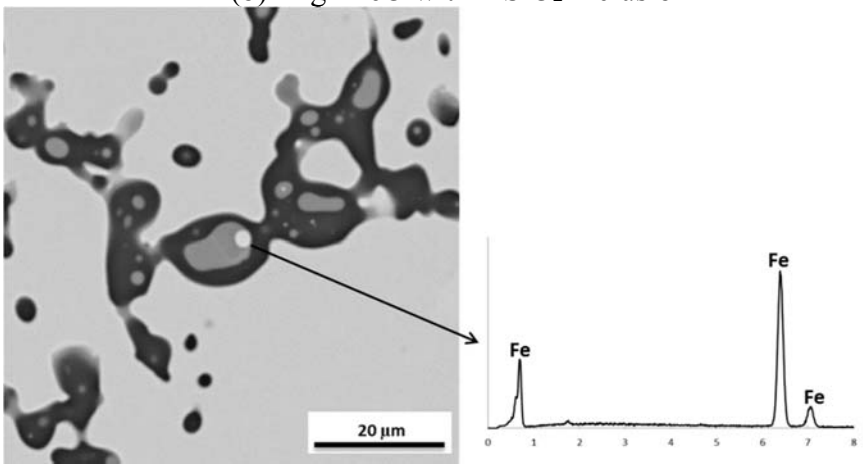

(c) Fe particle within SiO_2-CaO-Al_2O_3 inclusion

Figure 6. Types of inclusion observed after Fe75Si dissolution

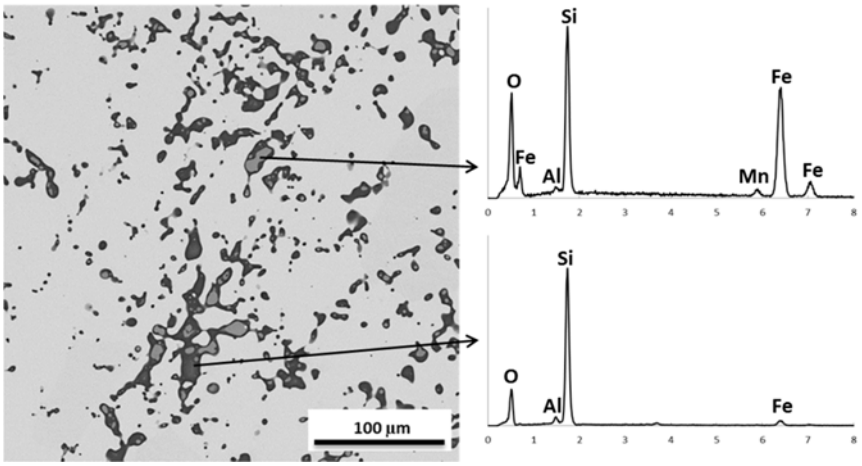

(d) Precipitates formed near the bottom of the sampler

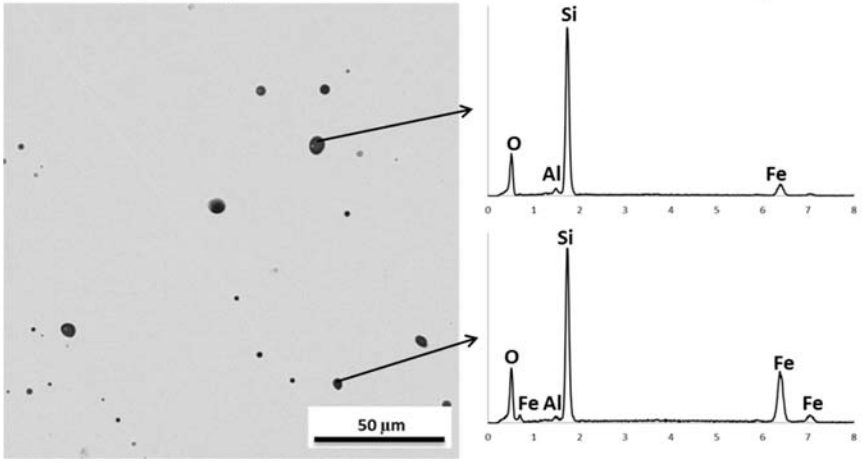

(e) Inclusions with variable FeO-SiO_2 content

Figure 6. Types of inclusion observed after Fe75Si dissolution cont.

Prior to Fe75Si addition, the steel contained about 0.2% total oxygen with dissolved oxygen measured around 0.05% (500 ppm). At this composition FeO-SiO_2 liquid phase would form in steel.[20] Before Fe75Si dissolution, the [Si] was low (starting from 0.07%) and the total oxygen was high (starting from 0.2 %), which would lead to the presence of FeO-SiO_2-MnO (liquid) inclusions. Figure 7 (a) shows the phase diagram for the FeO-SiO_2-MnO system with the initial inclusion chemistry predicted by thermal equilibrium identified. The phase diagram was plotted using FToxid database of

FactSage at P_{O2} = 1.01x10^{-4} MPa (0.001 atm). The phase diagram did not change significantly with lowering the P_{O2} and the chosen pressure was below the Fe/FeO ratio. As micro-mixing of the Fe75Si occurred in the sampler volume, [Si] increased in the metal around the inclusions, and the [O] dropped. The liquid phase shifts toward silica-saturation. The reaction takes place at the surface of the existing inclusions forming a Si-rich ring around the inclusions as can be seen in Figure 6 (a). Further, [Si] in steel would react with the FeO inside the inclusion to form more SiO_2 and pure Fe which can be trapped in the inclusion (Figure 6 (c)). Figure 7 (b) shows this possible mechanism of inclusion evolution with increasing SiO_2 content at 1873 K.

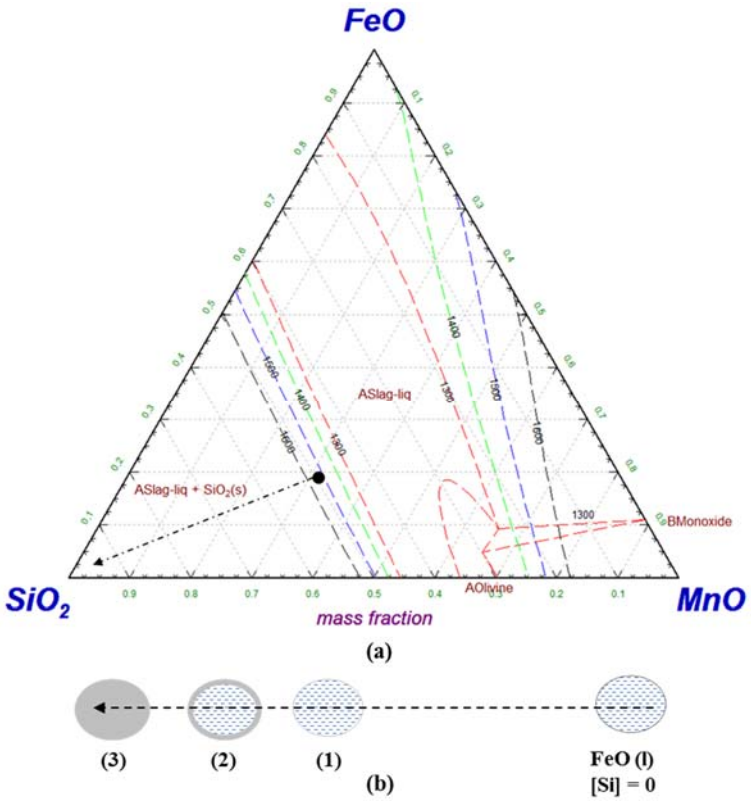

Figure 7. (a) Phase diagram for FeO-SiO_2-MnO system using FactSage with P_{O2}= 1x10^{-4} MPa showing the starting composition of inclusion predicted by thermodynamic equilibrium calculation, (b) Mechanism of inclusion evolution

FactSage calculations indicate that for complete mixing (equilibrium), the majority of inclusions should be SiO_2 (s). The number of liquid inclusions should be small with very low (<5%) FeO content. However, inclusions with high FeO (~50%) were observed in the sample (refer to Table 5 and Figure 6 (d)) confirming that equilibrium was not reached during the solidification time (70 seconds) as the diffusion through the outer SiO_2 layer will be slow.

4.2. Type 2: FeMn addition

FeMn has a comparable density (7180 kg/m^3) to steel (7200 kg/m^3)[11], so the floating behavior for these particles will be different compared to Fe75Si. When steel flows into the sampler, through the metal inlet (Figure 1 and Figure 2), the FeMn pieces sitting at the base of the sampler will not rise quickly in the steel. FeMn has a melting point of 1539 K[11], so its dissolution behavior will be similar to Fe75Si but the reaction following the melting of the steel shell would be less exothermic. The dissolution time for FeMn has been observed by previous researchers to be higher compared to Fe75Si. For a particle of 12 mm in size, the dissolution time for FeMn observed was 6 seconds compared to 2-3 seconds for Fe75Si particle of the same size.[11] After the addition of 5 gram FeMn to 240 gram of steel with initial chemistry shown in Table 2, the final composition would be 2.0% Mn by weight in steel. At this composition, manganese dissolves completely in steel. However, spectroscopy data (Table 4) showed regions with Mn content up to 9% suggesting that complete dissolution of the FeMn particle was not achieved. Most of the inclusions (>2μm) observed were oxide inclusions with an average

chemistry shown in Table 6. The chemistry of these inclusions was quite variable and did not really change much with size.

Table 6. Average MnO and FeO concentration in inclusions (wt. %) formed after FeMn dissolution and micro-mixing. Other components (CaO, Al_2O_3, SiO_2 and S) were less than 5%

Size range	MnO	FeO
2 -3 μm	23 ± 18	74 ± 20
3 - 5 μm	27 ± 21	70 ± 24
5 - 10 μm	25 ± 21	72 ± 24
>10 μm	36 ± 27	55 ± 28

Figure 8 shows the results obtained from the inclusion analysis after FeMn dissolution and micro-mixing with the same calculation methodology as was applied to Fe75Si. Weighted average manganese content in the inclusions (>2 μm) was observed to be higher (>35%) close to the bottom of the sampler (Figure 8 (a)). In the horizontal direction, the manganese content of inclusions showed large Mn rich (>50%) inclusions near the center (Figure 8 (b)). At the edges, the Mn content was observed to be lower (Figure 8). Since dissolution (melting) of FeMn was slower compared to Fe75Si, the time available for Mn to micro-mix across the sample and form inclusions was smaller. As the steel solidification will be faster at the edges, these regions will have low Mn content in the inclusions. Inclusions with variable chemistries and morphologies were observed in the sampler after FeMn dissolution as shown in Figure 9.

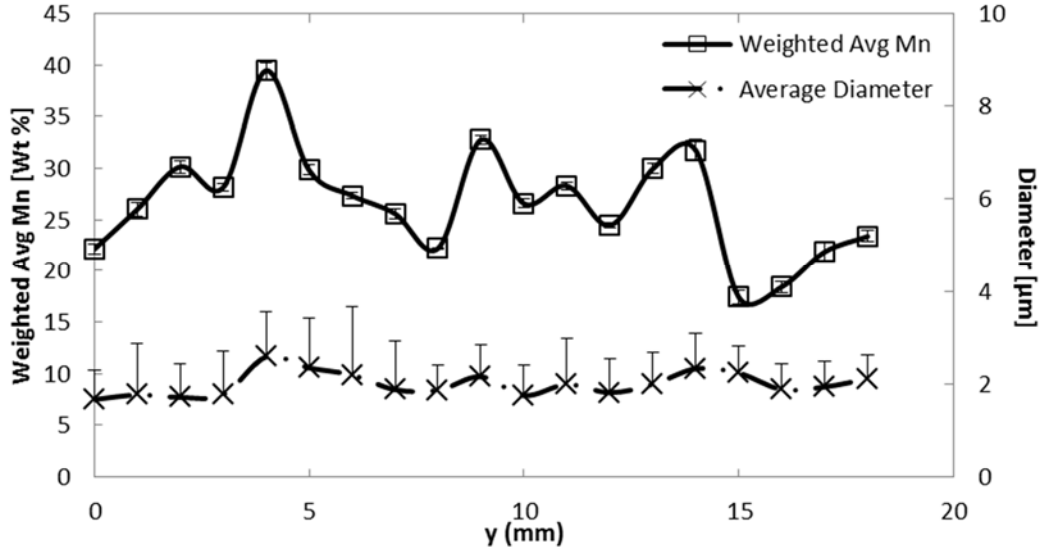

(a)

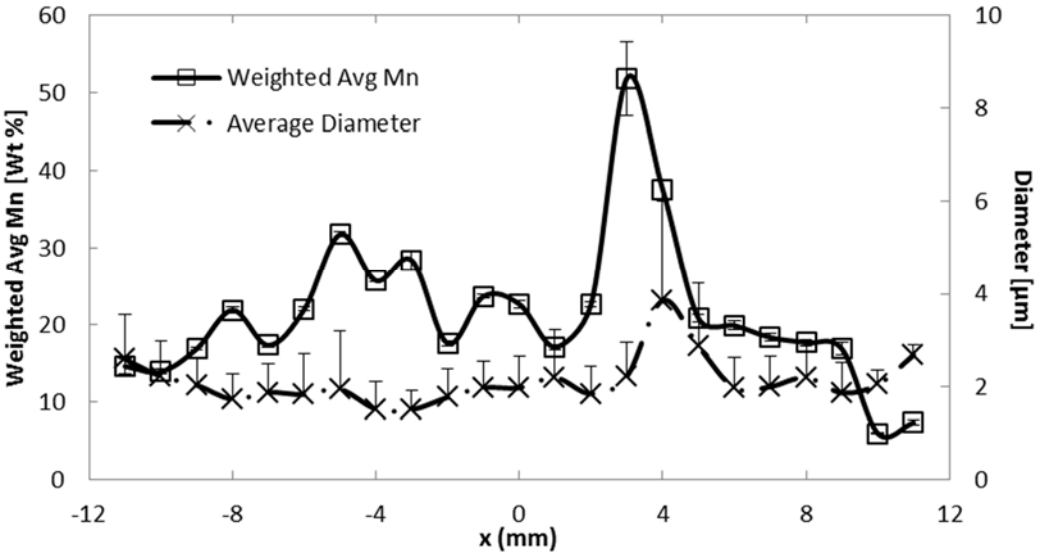

(b)

Figure 8. Results of inclusion analysis after FeMn dissolution and micro-mixing across the spherical sampler cross-section. Inclusion Mn content (for >2.0 µm) and diameter variation (for inclusions of all sizes) along the a) vertical and b) horizontal dimension of the sampler.

Thermodynamic predictions (with expected steel chemistry after FeMn addition and assuming complete homogenization) showed the formation of liquid inclusion phase

with high MnO (60-80%) content at 1873 K with SiO_2 (20-35%) as the other major component. The predicted equilibrium content of FeO in these inclusions was higher (5-10%) compared to Fe75Si addition. However, the Al_2O_3 content was lower (0.5-2.5%) because the amount of liquid inclusion phase predicted was ten times higher compared to Fe75Si dissolution. Large MnO-SiO_2 inclusions were observed in the samples (Figure 9 (b)). As the temperature would drop to 1773 K, a solid monoxide (MnO with varying FeO) phase would precipitate out of the slag. An example of this can be seen in Figure 9 (c) in which the MnO-FeO phase was present in the liquid phase. The monoxide phase was also predicted to precipitate out of steel at 1808 K which was close to the liquidus temperature of steel. These inclusions were observed as finer spherical inclusions (Figure 9 (a)).

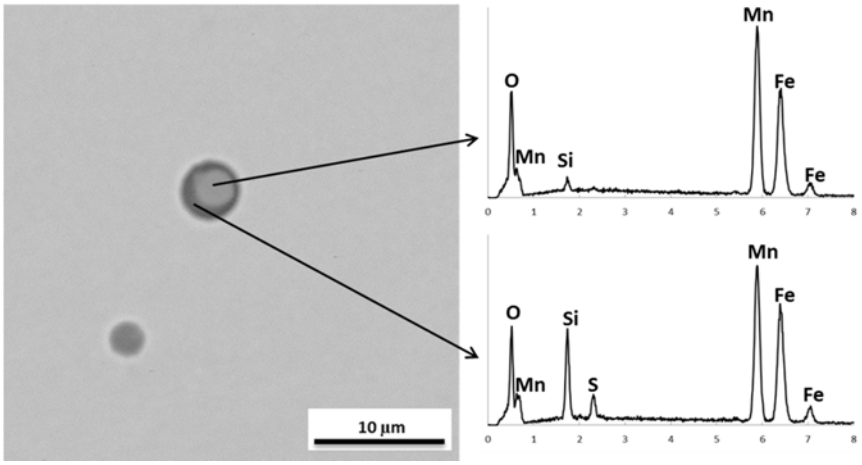

(a) Round particles of MnO within slag

Figure 9. Types of inclusion observed after FeMn dissolution

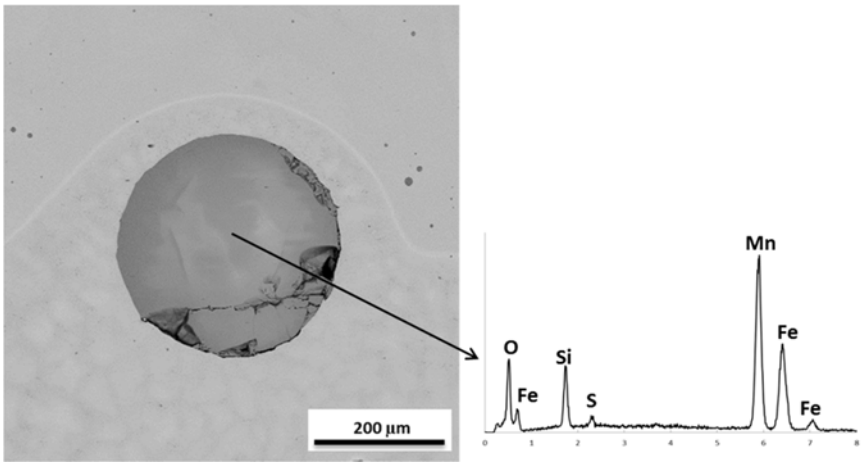

(b) Large MnO-SiO_2 inclusion

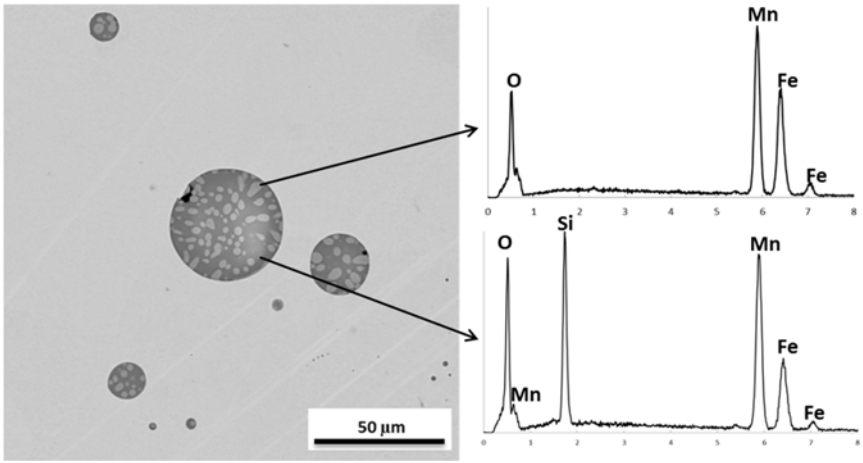

(c) Typical slag inclusion with precipitated MnO-FeO phase

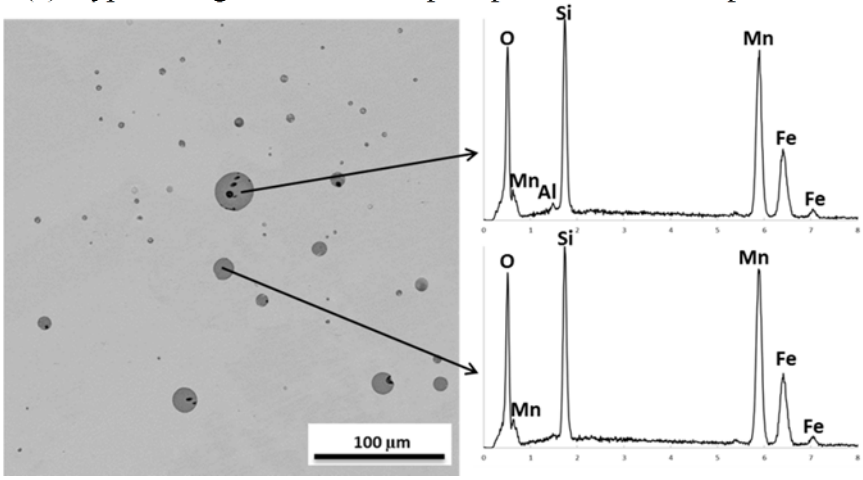

(d) Array of small inclusions with varying FeO-MnO content

Figure 9. Types of inclusion observed after FeMn dissolution cont.

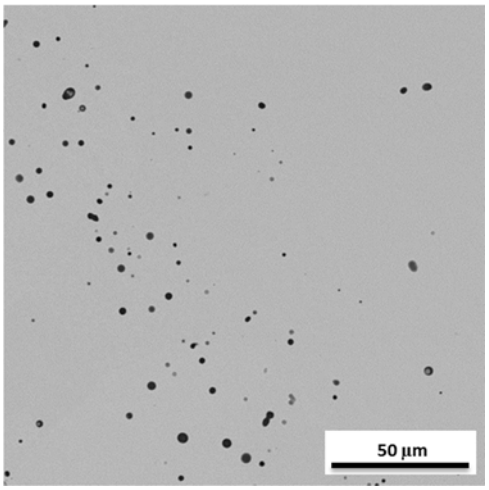

(e) Inclusions formed as a result of solute segregation during solidification
Figure 9. Types of inclusion observed after FeMn dissolution cont.

The phase diagram for FeO-SiO_2-MnO system indicated liquid phase inclusions (with FeO > 60%) at 1873 K (Figure 10 (a)). Before FeMn dissolution and micro-mixing, the [Mn] was low (starting from 0.17%) and the total oxygen (0.2 %) in steel was high (with 500 ppm dissolved oxygen), which would lead to the formation of FeO-MnO-SiO_2 (liquid) inclusions as marked in Figure 10 (a). As micro-mixing of the FeMn proceeded in the sampler volume, the liquid inclusions increased in MnO content, ultimately leading to precipitation of a MnO-FeO solid solution phase. The phase diagram suggested that a significant amount of MnO (greater than 45%) would be required for the solid solution to precipitate. Liquid phase inclusions with variable MnO content would form as the existing inclusions come in contact with Mn rich steel. Depending on the solidification rate these inclusions can be trapped in the steel as seen in Figure 9 (d). As more MnO adds to the existing inclusion, it mixes completely to form liquid phase. Figure 10 (b) shows the possible mechanism of inclusion evolution with

increasing MnO content. Figure 9 (c) shows an example of inclusions with morphology formed by this proposed mechanism (Figure 10 (b)).

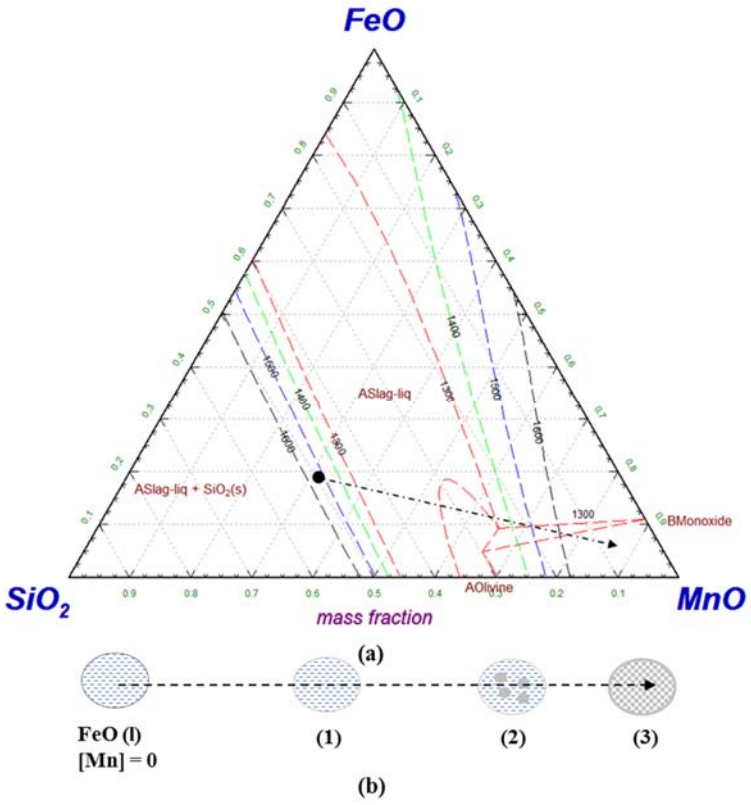

Figure 10. (a) Phase diagram for FeO-SiO_2-MnO system using FactSage with $P_{O2}=1x10^{-4}$ MPa showing the starting composition of inclusion predicted by thermodynamic equilibrium calculation, (b) Mechanism of inclusion evolution

FactSage calculations showed that for complete mixing (equilibrium), the majority of inclusions should be liquid phase at 1873 K. At this temperature the monoxide phase (solid-solution) inclusions would only form at Mn contents above 7%. Locally this Mn concentration was achieved in the sampler volume resulting in the formation of monoxide phase inside liquid inclusion.

4.3. Type 3: Fe75Si + FeMn addition

For the third type, equal amounts (2.5 gram each) of Fe75Si and FeMn were placed in the sampler. As discussed in the previous sections, FeMn is of similar density whereas Fe75Si has smaller density compared to steel. As steel flows, FeMn particles should stay at the bottom and Fe75Si particles should rise in the steel. As the melting points for both these alloys are much lower compared to that of steel, their dissolution process is similar. However, FeMn particles take longer to dissolve than Fe75Si particles. So, the micro-mixing of Si would start before Mn. Inclusion population fraction as a function of concentration ranges is shown in Figure 11.

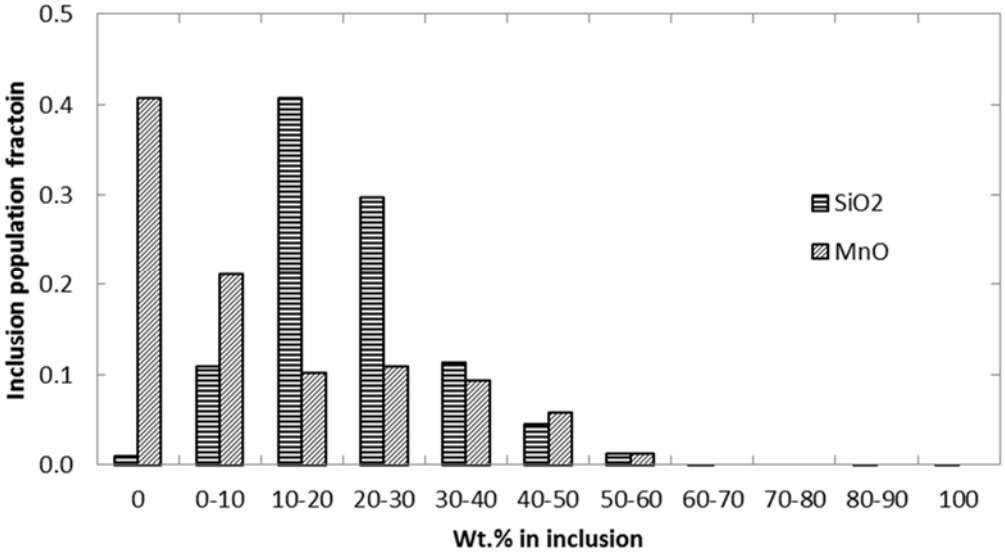

Figure 11. Inclusion population fractions in different concentration ranges for Fe75Si+FeMn addition

The figure shows typical bell shaped behavior for SiO_2 with most of the inclusion containing 10-30 wt. % SiO_2. No such behavior was observed for MnO with 40% of the inclusions containing no MnO. This is reflected in the average inclusion chemistry for this addition shown in Table 7. For MnO content the standard deviation in concentration is larger than the average values because of the presence of inclusions without any MnO.

Table 7. Average SiO_2, MnO and FeO concentration in inclusions (wt. %) formed after Fe75Si + FeMn dissolution and micro-mixing. Other components (CaO, Al_2O_3 and S) were less than 1%

Size range	SiO_2	MnO	FeO
2 - 3 μm	18 ± 8	11 ± 14	71 ± 14
3 - 5 μm	26 ± 12	12 ± 15	61 ± 16
5 - 10 μm	32 ± 17	16 ± 17	52 ± 18
>10 μm	27 ± 12	28 ± 18	45 ± 21

Comparison of average inclusion diameter in the vertical direction showed large inclusions with maximum variation near the center of the sampler where solidification would occur last (Figure 12 (a)). At the top and the bottom, the inclusions were smaller, presumably because they were trapped in the solidifying steel. In the horizontal direction, the largest inclusions were found off of the center (Figure 12 (b)) where the Mn+Si content was also high. The typical inclusions formed for this case can be seen in Figure 12.

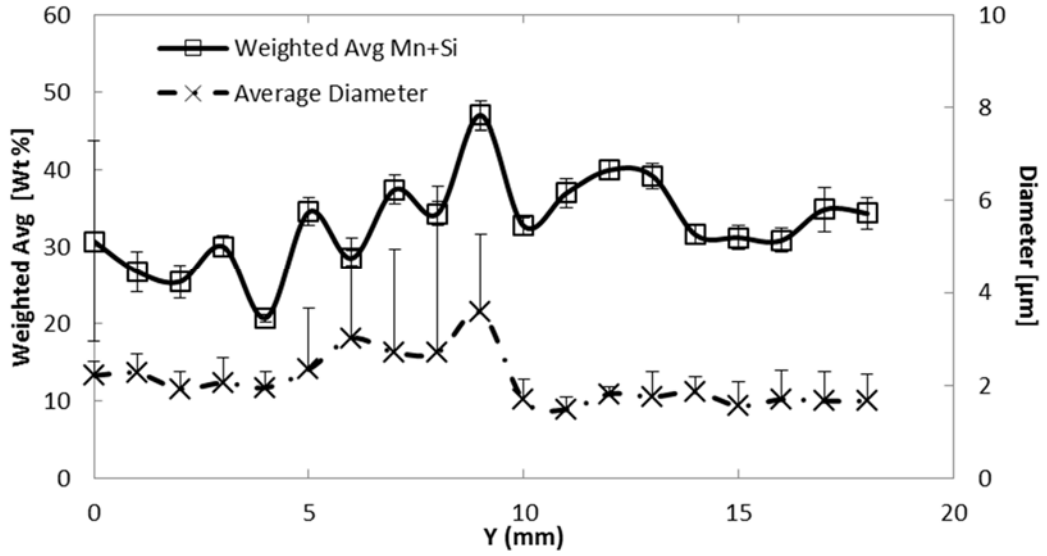

(a)

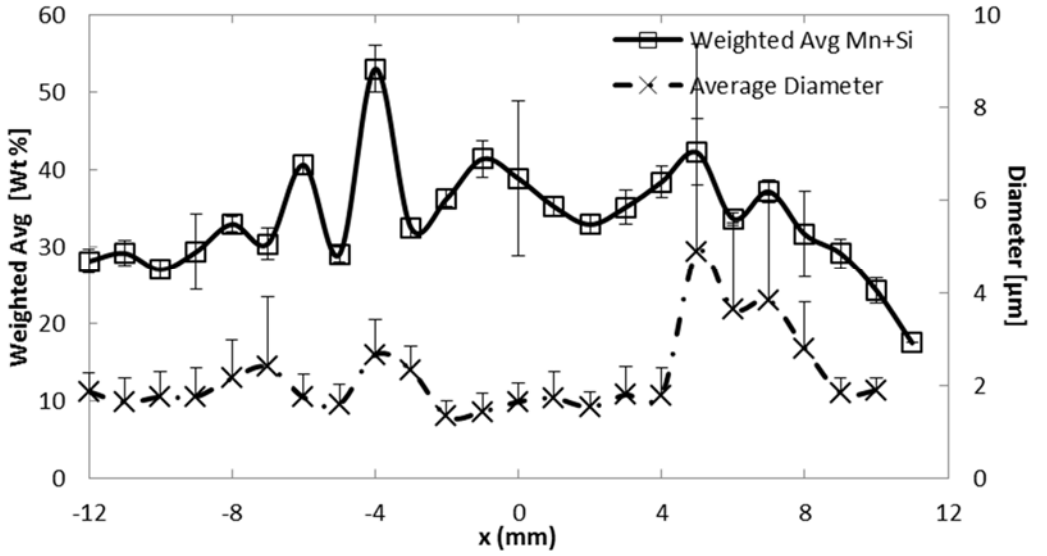

(b)

Figure 12. Results of inclusion analysis after FeMn+Fe75Si dissolution and micro-mixing across the spherical sampler cross-section. Inclusion Mn+Si content (for >2.0 µm) and diameter variation (for inclusions of all sizes) along the a) vertical and b) horizontal dimension of the sampler.

Thermodynamic predictions, with expected steel chemistry after Fe75Si and FeMn addition assuming complete homogenization, showed the formation of a liquid

phase with high SiO_2 (55-60%) and MnO (25-35%) content at 1873 K. Other constituents were FeO (~5%) and Al_2O_3 (5-7%). The solid cristobalite (SiO_2) phase was also predicted to form in steel at this temperature. The amount of the cristobalite phase was predicted to increase with decreasing temperature. The SiO_2-rich liquid phase itself would precipitate out cristobalite phase at about 1738 K. This can be observed in the elemental map shown in Figure 14 and the typical inclusions shown in Figure 13.

In Figure 13 (a) and Figure 13 (b), MnO-SiO_2 inclusions with SiO_2-rich phase around the inclusions can be observed. These were the most common inclusions presumably formed similar to the FeO-SiO_2 inclusions shown in Figure 7 (b). Figure 13 (c) showed an example of a MnO-SiO_2 inclusion with an Fe metal droplet inside with a SiO_2-rich outer layer. This inclusion could possibly form as a result of the following reaction:

$$2(FeO)_{inclusion} + Si_{steel} = Fe(l) + SiO_2(s) \quad (4)$$

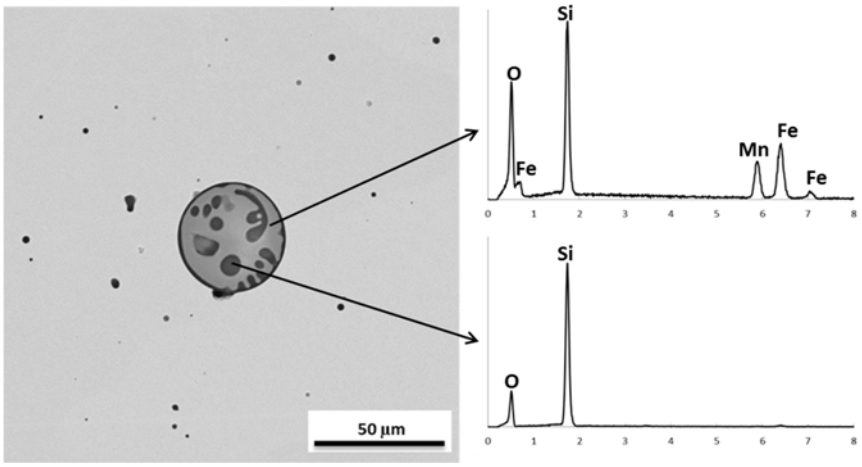

(a) MnO-SiO_2 inclusions with of SiO_2 rich region

Figure 13. Types of inclusion observed after FeMn+Fe75Si dissolution

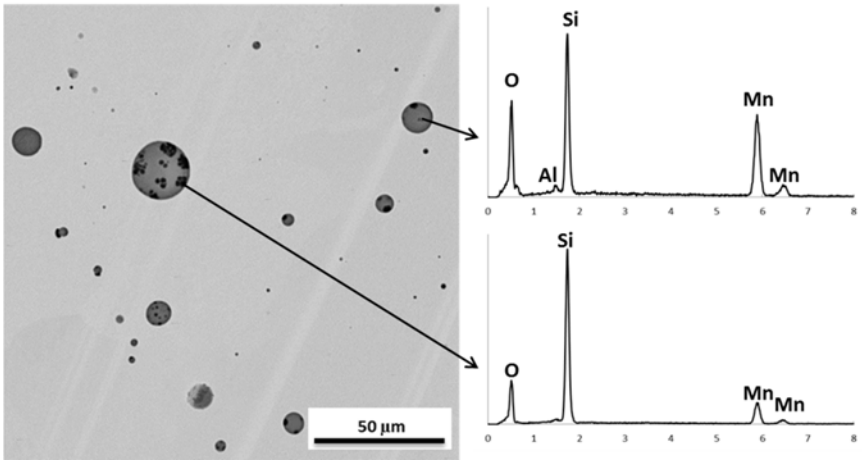

(b) Typical liquid inclusion with SiO_2 rich region as the darker phase.

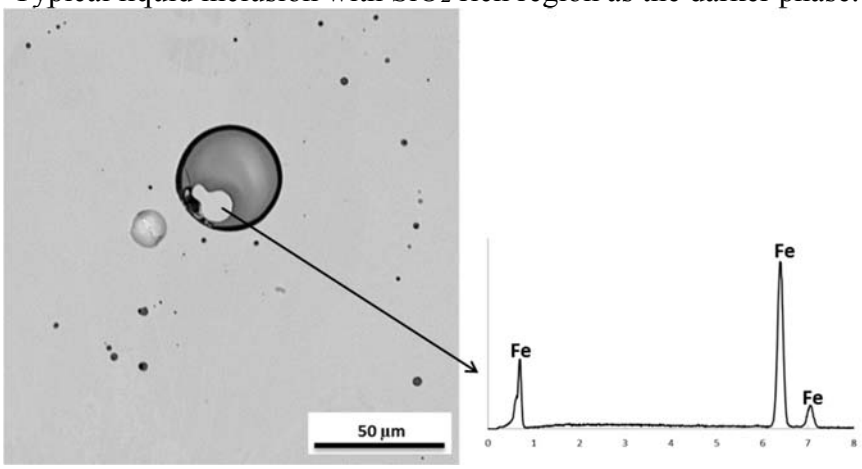

(c) Fe particle inside a typical MnO-SiO_2 inclusion

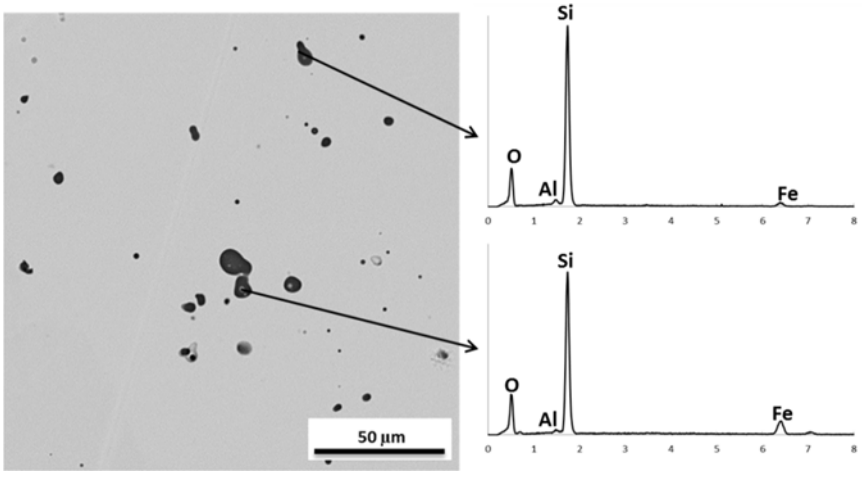

(d) Array of small SiO_2 inclusions with varying FeO content and negligible MnO

Figure 13. Types of inclusion observed after FeMn+Fe75Si dissolution cont.

The Fe liquid formed would be trapped inside the inclusion due to the solid layer of a SiO_2 rich phase. This behavior was observed in some inclusions. Inclusions with pure a Fe droplet trapped inside were also observed in the case of Fe75Si addition, but these inclusions were more prominent with the Fe75Si+FeMn addition. Small SiO_2 inclusions with varying FeO content were also observed near the bottom of the sampler and were presumably precipitated from the rapidly solidifying steel (Figure 13 (d)).

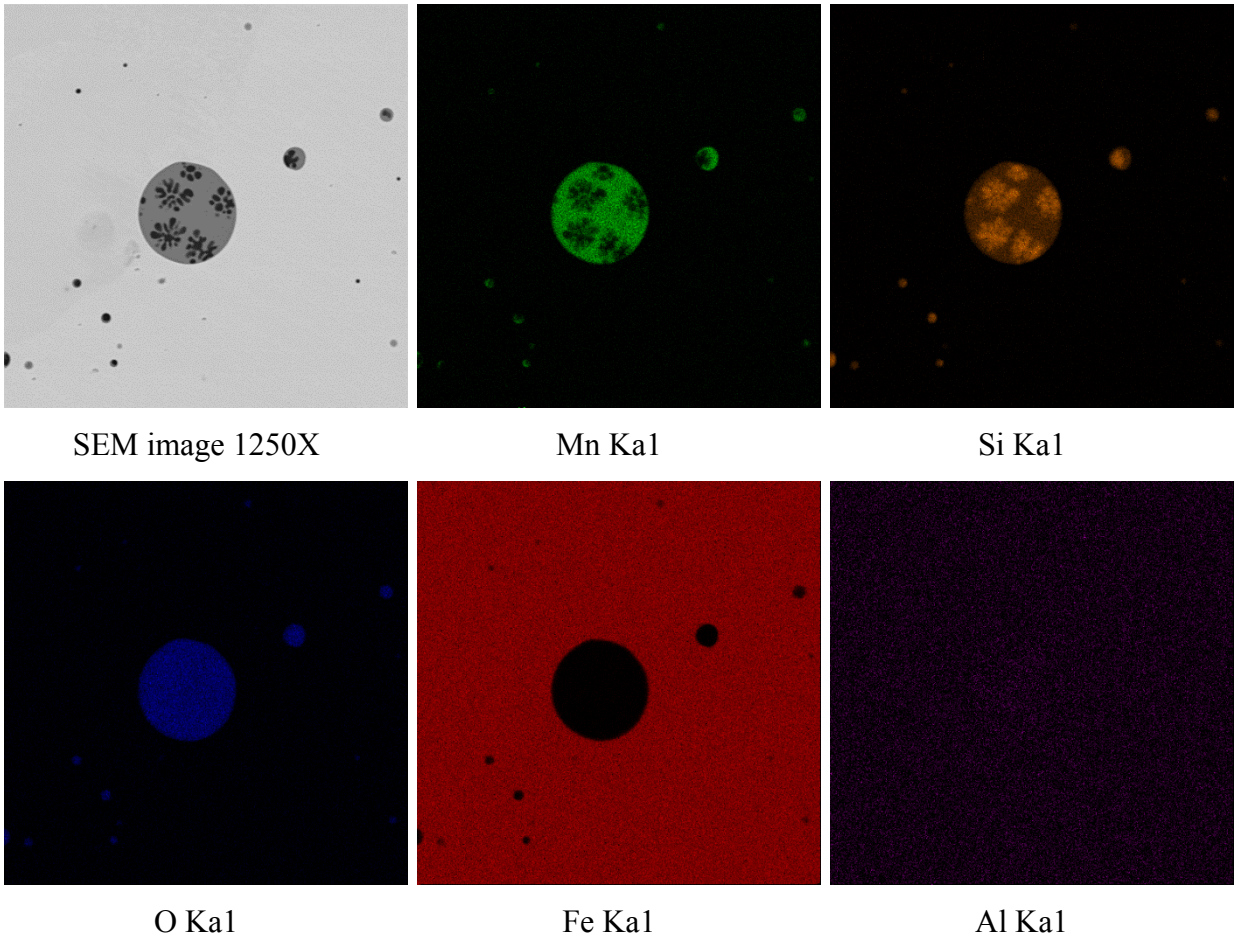

Figure 14. Characteristic X-ray map of constituent elements one of the typical inclusions observed in the Fe75Si+FeMn dissolution

5. CONCLUSIONS

A methodology to study the formation and evolution of inclusions soon after ferroalloy additions (for alloying or de-oxidation) has been developed. The present work revealed the evolution of inclusions formed in low carbon steel during and immediately after ferroalloy dissolution. The three cases studied were additions of ferro-silicon, ferro-manganese and a combination of both. Different dissolution behaviors were presumed based on work by Argyropolous[9)] for the ferroalloy additions. Ferro-silicon (less dense than steel) floated in the bath and dissolved rapidly compared to ferro-manganese (comparable density with steel) which took longer time to rise and dissolve.

The composition of liquid inclusions varied depending on the ferro-alloy used as did the morphology. The results are summarized below:

1. For all three ferroalloy additions, inclusion formation began with an FeO-rich phase due to the high initial oxygen content in steel. As the deoxidizer was mixed into the liquid steel, it reacted with both the oxygen dissolved in the steel and at the surface of FeO-rich inclusions.
2. For the Fe75Si addition, Si reacted at the surface of the inclusion forming an SiO_2 rich layer which can slow down the further transformation of these inclusions.
3. For the FeMn addition, solid solution of FeO-MnO was precipitated inside the liquid inclusions. As these inclusions are liquid and have no solid interface, they will be easier to transform.

4. For the Fe75Si+FeMn addition, de-oxidation will be more effective reducing the FeO in the existing inclusions to Fe. These inclusions form liquid MnO-SiO_2 layer on the outside.
5. All inclusions were liquid, with the possible exception of the ones that had high SiO_2 concentration on the surface. During processing the liquid inclusions would have time to transform. However, the solid inclusions would be difficult to transform but could serve as nucleation sites for later stage inclusion growth.

Inclusions in their initial stage of evolution were quenched in a sampler volume which resulted in the development of an understanding of mechanisms for inclusion formation. In the case of de-oxidation or alloy addition in a ladle, most of these transient inclusions would transform and equilibrate with steel, given sufficient time. The contact time between steel and inclusions in a ladle is of the order of 30 minutes compared to the 70 second time scale of this work. However, the SiO_2 layer (possibly solid) on the outside of some small inclusions would prevent them from transforming. These inclusions can further act as heterogeneous nucleation sites for secondary inclusions in subsequent processes. An approach like this can help in predicting early stage inclusion which will eventually help in understanding the nucleation and growth of inclusions in the later stages.

ACKNOWLEDGEMENT

The authors would like to express their sincere appreciation and gratitude for the late Professor Kent D. Peaslee for providing guidance and support for this research and for always being an inspiration for us.

REFERENCES

1) R. Kiessling: "Non-metallic inclusions in steel"- Part III, 2nd edn, The Institute of Materials, London, (1978), O1.

2) L. F. Zhang and B. G. Thomas: *Metall. Mater. Trans. B*, 37 (2006), 733.

3) M. Nadif, J. Lehmann, M. Burty and J. F. Domgin: Proc. 7th Int. Conf. on Clean Steel, Hungarian Mining and Metall. Soc., Balatonfured, Hungary, (2007), 38.

4) L. Zhang and B.G. Thomas: XXIV National Steelmaking Symp., Morelia, Mich, Mexico, (2003), 138.

5) L. Zhang: *J. Iron Steel Res. Int*., 13 (2006), 1.

6) M. M. Pande, M. Guo, X. Guo, D. Geysen, S. Devisscher, B. Blanpain and P Wollants: *Ironmaking and Steelmaking*, 37 (2010), 502.

7) S. Abraham, R. Klein, R. Bodnar and O. Dremailova: *MS&T*, 2 (2006), 89.

8) S. Abraham, R. Klein, R. Bodnar and O. Dremailova: *MS&T*, 2 (2006), 109.

9) S. A. Argyropoulos: Electric Furnace Proc., Detroit, Mich., USA, 41 (1983), 81.

10) S. A. Argyropoulos and R. I. L. Guthrie: Steelmaking Conf. Proc, Iron & Steel Soc. of AIME, Pittsburgh, PA, USA, (1982), 156.

11) Y. E. Lee, H. Berg and B. Jensen: *Ironmaking and Steelmaking*, 22 (1995), 486.

12) L. Zhang and B. G. Thomas: *ISIJ Int*., 43 (2003), 271.

13) S. Ganguly and S. Chakraborty: *Ironmaking and Steelmaking*, 35 (2008), 524.

14) D. Mazumdar and R. Guthrie: *ISIJ Int*., 35 (1995), 1.

15) K. Wasai, K. Mukai and A. Miyanaga: *ISIJ Int*., 42 (2002), 459.

16) M. Wakoh and N. Sano: *ISIJ Int*., 47 (2007), 627.

17) M. Van Ende, M. Guo, J. Proost, B. Blanpain and P.Wollants: *ISIJ Int*., 50 (2010), 1552.

18) M. Van Ende, M. Guo, J. Proost, B. Blanpain and P.Wollants: *ISIJ Int*., 51 (2011), 27.

19) C.W. Bale, P. Chartrand, S.A. Degterov, G. Eriksson, K. Hack, R. Ben Mahfoud, J. Melancon, A.D. Pelton and S. Petersen: *Calphad Journal*, 26 (2002), 189.

20) E.T. Turkdogan: "Fundamentals of Steelmaking", 1st edn, The Institute of Materials, London, (1996), 111.

II. INCLUSION MODIFICATION IN Si-Mn KILLED STEELS USING TITANIUM ADDITION

Vivek Thapliyal

Abhishek Kumar

David G. C. Robertson

Jeffrey D. Smith

Materials Science and Engineering

Missouri University of Science & Technology

Rolla, MO

Phone - 573-341-6469,

E-mail – vtty6@mst.edu

Published in ISIJ International

ABSTRACT

Modification of inclusions by titanium (Ti) additions in low-alloyed Si-Mn killed steels was studied by measuring the inclusion count and chemistry. Mn-Si-Al-S-O based inclusions were observed in the steel, after Si-Mn de-oxidation, to which ferro-titanium (FeTi) additions were made. Thermochemical software (FactSage) was used to study the equilibrium between steel and inclusions and subsequent modification due to Ti addition. Inclusion count and chemistry in the steel were measured at different time intervals after the FeTi additions. $MnO\text{-}SiO_2$ inclusions transformed to $TiO_2\text{-}MnO\text{-}SiO_2$ based inclusions with Ti replacing both Mn and Si in the inclusions. Si removal was more prominent from the inclusions compared to Mn. When more FeTi was added to the steel the inclusions further decreased in their Mn and Si content and Ti based inclusions with Al and Mn content less than 10% and Si content less than 5% were formed. MnS inclusions were also observed in the steel and formed as a result of segregation during solidification.

Key Words: inclusion modification; ferro-titanium addition; thermodynamic modeling

1. INTRODUCTION

Non-metallic inclusions are undesired particles that impact mechanical properties and surface quality of steel. They may also cause processing difficulties such as nozzle-clogging and break-outs during casting.[1,2] Inclusions need to be removed or modified to achieve optimal steel properties. The main objective of inclusion modification techniques is to convert existing solid inclusions to liquid inclusions that can either be removed by coalescence and floatation or deformed in the solidified steel.[3-6] Further, liquid inclusions would be easy to deform thus preventing failure during casting. The inclusions that were liquid may be solid at deformation temperatures but being round in shape as solids would cause fewer problems during deformation.[3,7] Calcium treatment in aluminum-killed steels is a known technique for the modification of solid Al_2O_3 inclusions to form liquid calcium aluminate inclusions.[2,8,9]

In the past, several techniques have been employed for inclusion modification and removal. Liquid inclusions coalesce to form larger inclusions and are easier to remove. These inclusions can attach to refractory surfaces or get entrapped by the liquid slag. Slag properties can be optimized in order to enhance the entrapment and absorption of non-metallic inclusions.[10] Argon bubbling, [11,12] magnetic stirring, [13] and optimization of top slag, [1,4,10] are ways to remove inclusions. Inclusion floatation occurs because of differences between densities of non-metallic inclusions and molten steel, however many inclusions are too small for the floatation to be effective. It is important for these small inclusions to coalesce and become larger in order to float. Electromagnetic or gas stirring can increase inclusion coalescence/agglomeration and floatation. Inclusions can be

modified by adding materials (Ca, Ti etc.), which chemically combine with the existing inclusions to form liquids at steel making temperatures (1550-1650°C).[1)]

Si-Mn de-oxidation is widely used in steelmaking prior to casting. It has an advantage over aluminum de-oxidation in that the primary inclusions are generally liquid.[14)] In Si-Mn killed steels, expected inclusions are a combination of MnO, SiO_2 and Al_2O_3.[15)] Impurities in the ferro-alloys and refractories are the sources of Al_2O_3in these inclusions.

Figure 1 shows SiO_2-TiO_2-MnO phase diagram plotted using FactSage 6.4[16)] at 1250°C and oxygen partial pressure of 10^{-5} atm. Kang et al.[17)] reported that SiO_2-TiO_2-MnO phase equilibria depend on the oxygen potential. While plotting the ternary diagram the oxygen partial pressure was varied between 10^{-5} - 0.21 atm (expected in this study) but no significant difference was observed. The ternary diagram shows the liquid phase region (Slag-liq) enlarged by the addition of TiO_2 to MnO-SiO_2 binary system. Amitani et al.[18)] report similar behavior at 1300°C and 1500°C. Thus, the use of FeTi after Si-Mn de-oxidation has the potential to form liquid inclusions with an even lower melting point and ease the inclusion removal process. The purpose of this study was to determine the effect of Ti on the evolution of inclusion composition, size and removal. Inclusion modification can also be used to help precipitate target phases in the solid state by providing the necessary precipitation sites – so-called “Oxide Metallurgy”.[19)] Ti-addition has been studied by researchers to modify MnO-SiO_2 inclusions and enhance MnS precipitation.[18,20)] These precipitates work as nuclei for inter-granular ferrite formation from austenite.[18,20)]

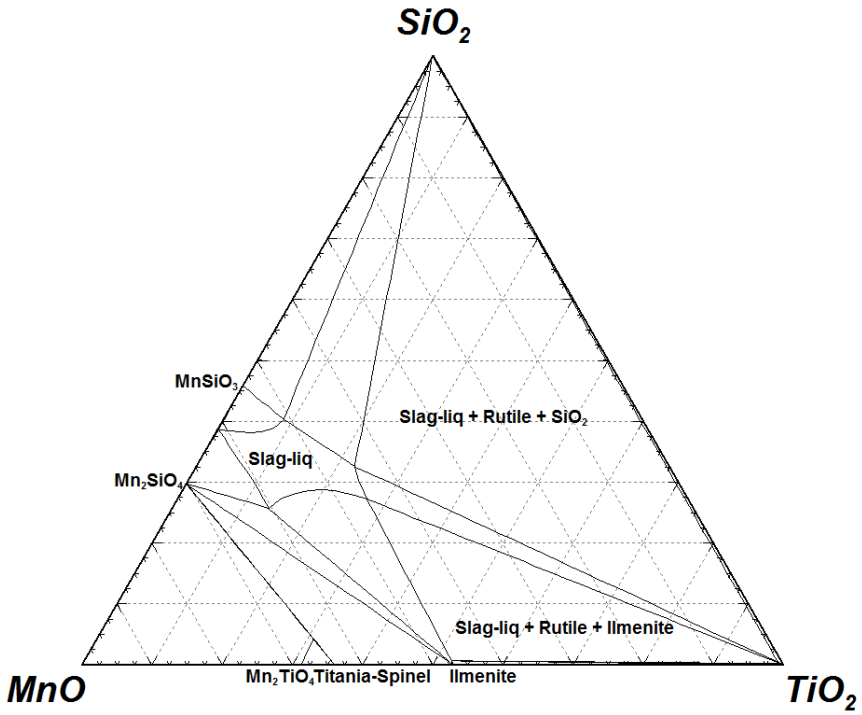

Figure 1. MnO-SiO_2-TiO_2 phase diagram plotted at 1250°C and $P_{O2} = 10^{-5}$ atm using FToxid – FACT oxide database of FactSage

In the present study inclusion modification in low-alloy Si-Mn de-oxidized steel using Ti addition was studied. Inclusion chemistry and morphology variation were evaluated as a function of the amount of Ti added as well as time after addition. The modification was modeled using thermodynamic software FactSage and the calculations were compared to the experimental values.

2. EXPERIMENTAL PROCEDURE

Experiments were conducted in an induction furnace with a crucible of size 10 cm internal diameter and 20 cm height. Induction iron (7 kg) was melted and ferro-alloy additions were made. Temperature of liquid steel was maintained around 1600°C (± 5°C). Argon was blown at the rate of 1 liter/min over the liquid steel and under a refractory blanket to minimize oxidation.

The initial chemistry of the induction iron is shown in Table 1. Ferro-silicon (Fe75Si) and ferro-manganese (FeMn) additions were made to de-oxidize the induction iron and form steel (Table 1) containing MnO-SiO_2 based inclusions. Total oxygen in the steel after the Fe75Si + FeMn addition was measured to be 170 ppm (0.017 wt. %) using LECO O and N analyzer (TC 500).

Table 1. Initial chemistry of induction iron and steel (after Mn-Si addition) used for the experiment (balance Fe) measured using arc-spectroscopy

Wt. %	C	Si	Mn	P	S	Cr	Ni	Al	Cu	Ti
Induction iron	-	-	0.21	0.04	0.01	0.07	0.04	0.004	0.04	-
Steel	0.03	0.13	0.68	0.04	0.01	0.06	0.04	-	0.04	-

FeTi additions were made to the deoxidized steel and the impact on inclusions was analyzed. Compositions of all the ferro-alloys used in this study are shown in Table 2.

Table 2. Ferro-alloy compositions used for this study (balance Fe)

Wt. %	C	Si	S	Mn	P	Ca	Al	Ti
Fe75Si	<0.1	73-78	<0.02	-	<0.04	<0.6	<1.5	-
FeMn	0.078	0.28	0.025	97.08	0.026	-	-	-
FeTi	0.1	0.1	0.01	0.2	0.01	-	0.2	70

Multiple FeTi additions were made to the liquid steel and samples were taken at different time intervals. Table 3 shows the sampling chart for the samples taken during the experiment along with additions made.

Table 3. Sampling Chart

Time of addition	Additions	Sample A	Sample B	Sample C
0 min	17 g Fe75Si+38 g FeMn Si (0.18 wt. %), Mn (0.53 wt. %)	+2 min	+5 min	
10 min	2 g FeTi, Ti (0.02wt. %)	+1 min	+3 min	+5 min
20 min	2 g FeTi, Ti (0.02 wt. %)	+1 min	+3 min	+5 min
30 min	3 g FeTi, Ti (0.03 wt. %)	+1 min	+3 min	+5 min

Samples were analyzed using arc spectroscopy to measure steel chemistry at each sampling step. LECO analyzer was used to measure the oxygen and sulfur content of steel. Inclusion chemistry and morphology were studied using automated scanning electron microscopy (ASPEX).

3. THERMODYNAMIC MODELING OF INCLUSION TRANSFORMATION

Data for inclusion chemistry, obtained from SEM-EDS, was used for modeling inclusion transformation with FeTi additions. Composition of the inclusions in terms of Al, Ca, Mn, S, Si and Ti was obtained from SEM-EDS, whereas, Fe and O concentration could not be measured accurately using this method. So, the oxygen was calculated stoichiometrically assuming primary oxides for the elements selected. For Ti, a 2:1 molar combination of TiO_2 and Ti_2O_3 ($TiO_{1.75}$) was assumed, which was similar to that calculated by thermodynamic software. The oxygen value was also adjusted for the sulfur content in the inclusion by balancing oxygen and sulfur anions to the metal cations.

Inclusions were divided into major categories based on the prime components and further sub-divided into sub-types based on the composition range. For each of the sub-types, average inclusion chemistry was calculated. This averaged data was used along with the steel chemistry for equilibrium calculations.

Equilibrium calculations were carried out at 1600°C using thermodynamic software FactSage. To assess whether a given sub-type of inclusion was in equilibrium with the steel, it was reacted with the steel and the composition change was monitored. The stability (equilibrium with steel) of each inclusion sub-type was studied using the "Equilib" module of FactSage, considering the steel, slag, solid-solutions, and all possible liquids and solids as the possible phases. The databases used in this study were: FSstel (compound and solution database for steel), FactPS (gas species, solid and liquid compound database) and FToxid (compounds and solutions for oxide databases, with S in the oxide slags). The ratio of steel used for the equilibrium calculation per 100 g of inclusion was also varied. Based on the composition, steel to inclusion ratio of 1000:1

was selected. As Fe and O content of the inclusion were not measured accurately, any transfer of Fe and O from the steel to inclusion was allowed. However, any significant transfer from the inclusion phase to the steel indicated the non-equilibrium (instability) of the inclusion phase. Figure 2 (a) shows a representation of the FactSage model used to determine inclusion-steel equilibrium. To study inclusion modification with Ti addition, its local equilibrium with steel was modeled. For each of these calculations 1 g of inclusion, of chemistry measured before addition, was reacted with 1000 g of steel of chemistry measured immediately after each addition as shown in Figure 2 (b)

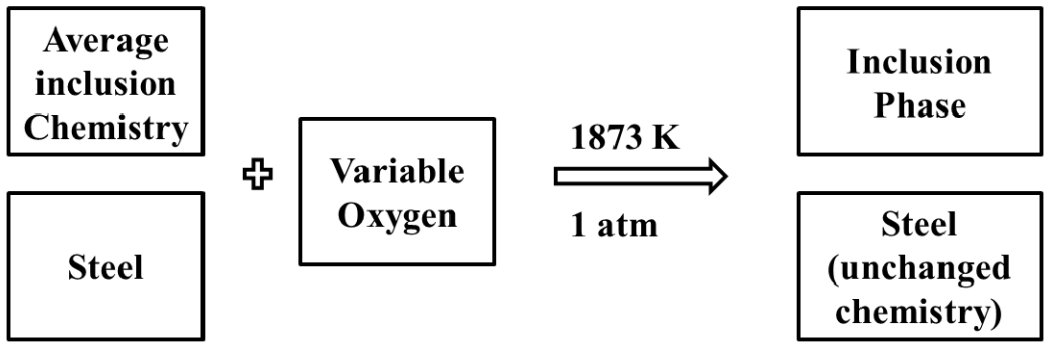

(a)

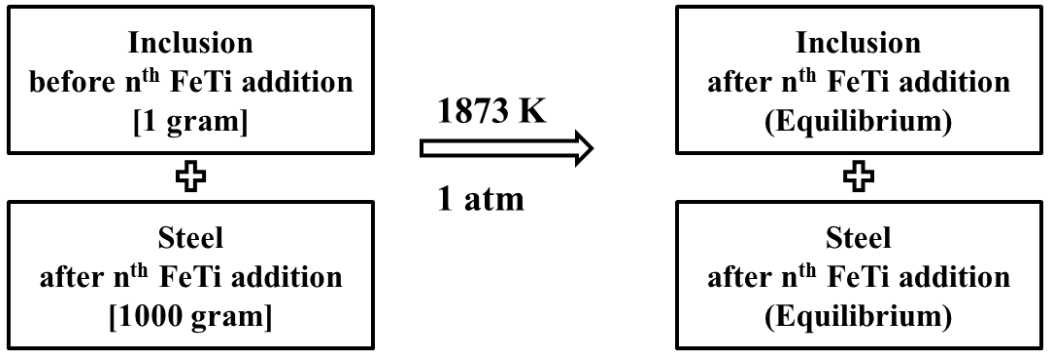

(b)

Figure 2. Representation of thermodynamic FactSage model (a) to determine inclusion-steel equilibrium and (b) to determine inclusion transformation with FeTi addition for n = 1, 2 or 3

4. RESULTS AND DISCUSSIONS

Inclusion behavior and transformation were studied by plotting inclusion chemistries obtained from SEM-EDS on a ternary diagram. The inclusion chemistries had 6 major components namely Al, Ca, Mn, S, Si and Ti. To plot the inclusion chemistries on a ternary diagram three major elements were selected. The fourth significant element was plotted using color scale where the color corresponds to concentration. The inclusions were plotted as circles where the size of each circle represented the inclusion size.

4.1. Inclusions in Mn-Si Deoxidized Steel

In the case of samples taken after the Fe75Si + FeMn addition, Mn, Si and S were chosen as the three components for the ternary plot. Al was chosen as the fourth element for coloring the inclusion composition points. Few Ca rich inclusions (~ 3%) (Table 4) were also observed in these samples, whereas Ti was observed as an impurity in the samples.

Table 4. Type of inclusions with analysis (wt. %) observed after 5 minutes of Fe75Si + FeMn addition (balance O, with Ca and Ti as minor species)

Type	Population%	Diameter (μm)	S		Mn		Si		Al	
			min	max	min	max	min	max	min	max
Oxide	3%	2.3 ± 1.6	0	5	0	5	0	5	0	15
	1%	0.8 ± 0.5	0	5	0	5	35	45	5	15
	8%	1.4 ± 0.5	0	5	15	55	5	35	0	5
	10%	2.3 ± 1.5	0	5	15	45	15	35	5	15
	6%	Other Compositions								
Mixed	9%	1.2 ± 0.6	5	15	15	45	15	25	0	5
	3%	0.9 ± 0.2	5	15	15	25	25	35	0	5
	1%	0.9 ± 0.3	5	15	15	25	25	35	5	15
	18%	1.1 ± 0.4	5	15	25	45	15	25	0	5
	5%	1.1 ± 0.5	5	15	35	55	5	15	0	5
	6%	Other Compositions								
Sulfide	7%	0.9 ± 0.2	15	25	25	45	15	25	0	5
	1%	0.6 ± 0.2	15	25	25	35	15	25	5	15
	6%	0.9 ± 0.4	15	25	35	55	5	15	0	5
	5%	0.8 ± 0.3	25	35	25	55	5	25	0	5
	2%	0.7 ± 0.4	35	45	45	65	0	5	0	5
	9%	Other Compositions								

On the Mn-Si-S ternary plots shown in Figure 3, inclusions measured after 2 and 5 minutes of the Mn-Si addition (Fe75Si + FeMn) are plotted. Minute difference can be observed in these plots indicating that the inclusion distribution was stable after 2 minutes and behaved the same during mixing and solidification processes. There is also a "scatter" towards MnS that is common to all times, presumably due to MnS formation/precipitation in interdendritic liquid during solidification. This latter trend was observed to be independent of the sampling time. Based on the ternary diagram, Mn content in larger inclusions (>3 μm) was almost constant (50-60%). Most of these inclusions were oxides (Mn-Al-Si-O). The sulfur-rich inclusions were observed to be

smaller (<1 μm) in size. Average inclusion chemistries of the prominent inclusions observed in the steel 5 minutes after the Mn-Si additions are summarized in Table 4.

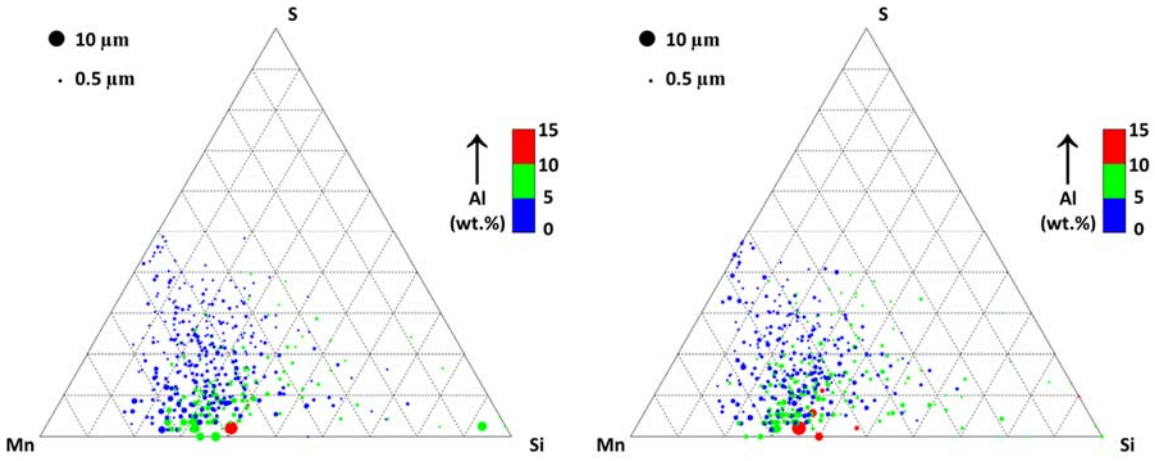

(a) After 2 minutes (b) After 5 minutes

Figure 3. Inclusion composition map after Fe75Si + FeMn addition shown on Mn-S-Si ternary with Al concentration on the color scale for inclusions with low Ca (<10%)

As shown in Table 4, the inclusion population can be divided into three major categories namely: “oxides”, “mixed” and “sulfides” with the sulfur being the distinguishing element. Further among these categories, there are composition ranges for Mn, Si and Al. “Other compositions” is the fraction of inclusions of each type that do not fall into the ranges specified. Only those ranges were specified which contained more than 1% of the total inclusions. The percentage values indicate the population percentage of inclusions in each of these categories. The zero values in the table are the detection limit for the SEM-EDS.

As shown in the ternary diagram (Figure 3) and confirmed by Table 4, sulfide inclusions were the smallest of all the inclusions. In contrast, the largest inclusions were

the MnO-SiO_2 based inclusions with some Al_2O_3. Sulfur-rich inclusions were either purely MnS inclusions or MnS as predominant phase in oxide inclusions. In case of mixed inclusions, MnS precipitated on existing oxide inclusions whereas sulfide inclusions formed as a result of sulfur segregation during solidification. As a result, the average inclusion size was higher for mixed inclusions than the sulfide inclusions. MnS precipitation will first occur in steel on cooling at around 1400°C (predicted by FactSage). In comparison, the heterogeneous nucleation of MnS on existing oxide inclusions could take place at higher temperature. Similar behavior has been reported by other researchers.[18,20)]

Typical oxide inclusions formed after Mn-Si additions are shown in Figure 4. Most of these inclusions were spherical in shape owing to the fact that these inclusions were liquid at steelmaking temperature. Al was significant in these inclusions in addition to Mn and Si. Most of the inclusions observed were 1-3 μm in size (Table 4).

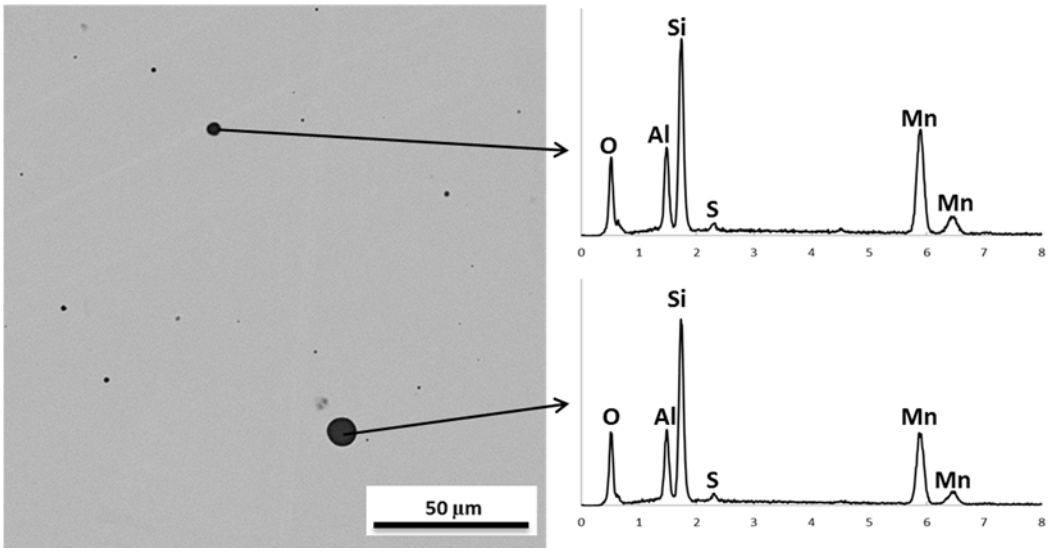

Figure 4. Typical Mn-Si-Al-O based oxide inclusion obtained 5 minutes after Fe75Si + FeMn addition

Thermodynamic calculations based on the model described earlier (Figure 2(a)) were performed to determine steel-inclusion equilibrium. Table 5 shows the sample results using steel and inclusion compositions obtained 5 minutes after Fe75Si + FeMn addition (Table 1 and Table 4). The inclusion chemistries shown in Table 5 were from four typical ranges of inclusion compositions observed in the steel. "Oxide (1)" and "Oxide (2)" inclusions were chosen as two widely different oxide inclusion compositions within the ranges observed in Table 4. When these inclusions are reacted with steel there is only a small amount of reaction required to equilibrate the inclusions (Table 5), so that despite their different compositions they can be considered to be close to equilibrium with the steel. The calculation for the "Mixed" inclusion shows that the inclusion would lose all its sulfur to steel and its overall mass reduces by about 30%. For the "Sulfide" inclusion this reduction in mass is about 45%. Therefore, the inclusions in the categories "Mixed" and "Sulfide" were not in equilibrium with steel at 1600°C.

Table 5. A representative result for the thermodynamic calculations for steel-inclusion equilibrium at 1600°C

			Inclusion composition (wt. %)			
Type		Steel	Oxide (1)	Oxide (2)	Mixed	Sulfide
Initial	S	0.01	4.5	2.7	14.5	20.9
	Mn	0.68	21.3	28.6	28.5	23.6
	Si	0.13	27.9	23	22.1	16.9
	Al	-	4.4	5.6	2.8	3.4
	100 g inclusion + 100,000 g steel					
Final	Slag weight (g)		100.2	97.6	72.5	55.6
	S		0.0	0.0	0.0	0.0
	Mn		26.1	26.5	23.5	26.3
	Si		21.5	20.3	22.2	20.1
	Al		5.2	6.9	5.1	7.5
	Prediction		Equilibrium	Equilibrium	Non-equilibrium	Non-equilibrium
	Change in inclusion		FeO gain	MnO loss	Sulfides dissolve	Dissolution

Oxide inclusions after the Fe75Si + FeMn addition were predicted to be in equilibrium with steel. For the range of inclusions shown in Table 4, liquid phase (slag) inclusions of composition MnO (25-50%), SiO_2 (30-60%), Al_2O_3 (5-10%) and FeO (5-10%) were predicted using the model. Mixed inclusions, were observed as liquid phase inclusions with MnS and FeS as significant components. These inclusions were not at equilibrium with the steel at 1600°C. Sulfide inclusions were observed to be liquid phase inclusions with more than 50% FeS and MnS. For inclusions with greater than 40% sulfur content, solid MnS inclusions were also observed. These inclusions were also not at equilibrium with the steel at 1600°C and were predicted to dissolve completely. This suggests that the mixed and sulfide inclusions formed in steel on cooling.

To study sulfur content in the inclusions of mixed and sulfide type, equilibrium and Scheil-Gulliver cooling studies were done for these inclusions using FactSage. For

these calculations, the average chemistries were used. Solid MnS was predicted to form at about 1375°C for equilibrium cooling. Above this temperature, the maximum sulfur content in the slag in equilibrium with steel was 4%. So, to achieve the amount of S observed in the inclusions solid MnS precipitation is required. Scheil-Gulliver cooling suggested MnS formation started at about 1400°C for these inclusions.

4.2. Effect of FeTi Addition on Mn-Si Based Inclusions

FeTi additions were made to the Mn-Si containing steel to observe the changes in the existing inclusions. The steel chemistry was measured and inclusion population was analyzed at different time intervals after the FeTi additions as shown in Table 6. Ti content in the steel was highest at one minute after the addition and it decreased with time. This suggests that Ti content decreased in the steel by removal of Ti-based inclusions.

To plot the ternary diagram for the inclusion population after FeTi addition, Ti, Mn and S were chosen as the key elements based on concentration. The silicon content of inclusions was selected for the color scale. Ca and Al were less significant (<10%) components for the majority (~80%) of inclusions.

Table 6. Steel chemistry after different additions with C - 0.032, P - 0.039, S - 0.009, Cr - 0.064, Ni - 0.04, Al -<0.001, Cu - 0.042 and Fe - balance (all values in wt. %)

Additions	Time	Si	Mn	Ti	O
2 g FeTi	1 min	0.12	0.66	0.014	0.017
	3 min	0.12	0.66	0.011	0.0174
	5 min	0.13	0.65	0.011	0.0194
2 g FeTi	1 min	0.11	0.58	0.020	0.0194
	3 min	0.12	0.58	0.021	0.0224
	5 min	0.11	0.56	0.012	0.0255
3 g FeTi	1 min	0.11	0.54	0.031	0.0245
	3 min	0.10	0.52	0.022	0.0205
	5 min	0.10	0.51	0.020	0.0281

On the Ti-Mn-S ternary plots shown in Figure 5, inclusions measured after 1 minute, 3 minutes and 5 minutes after the first titanium addition were plotted. From these plots (Figure 5) it can be seen that immediately after Ti addition the majority of inclusions contained high concentration of Ti. With increase in mixing time the inclusion compositions tended to move away from high Ti towards Mn.

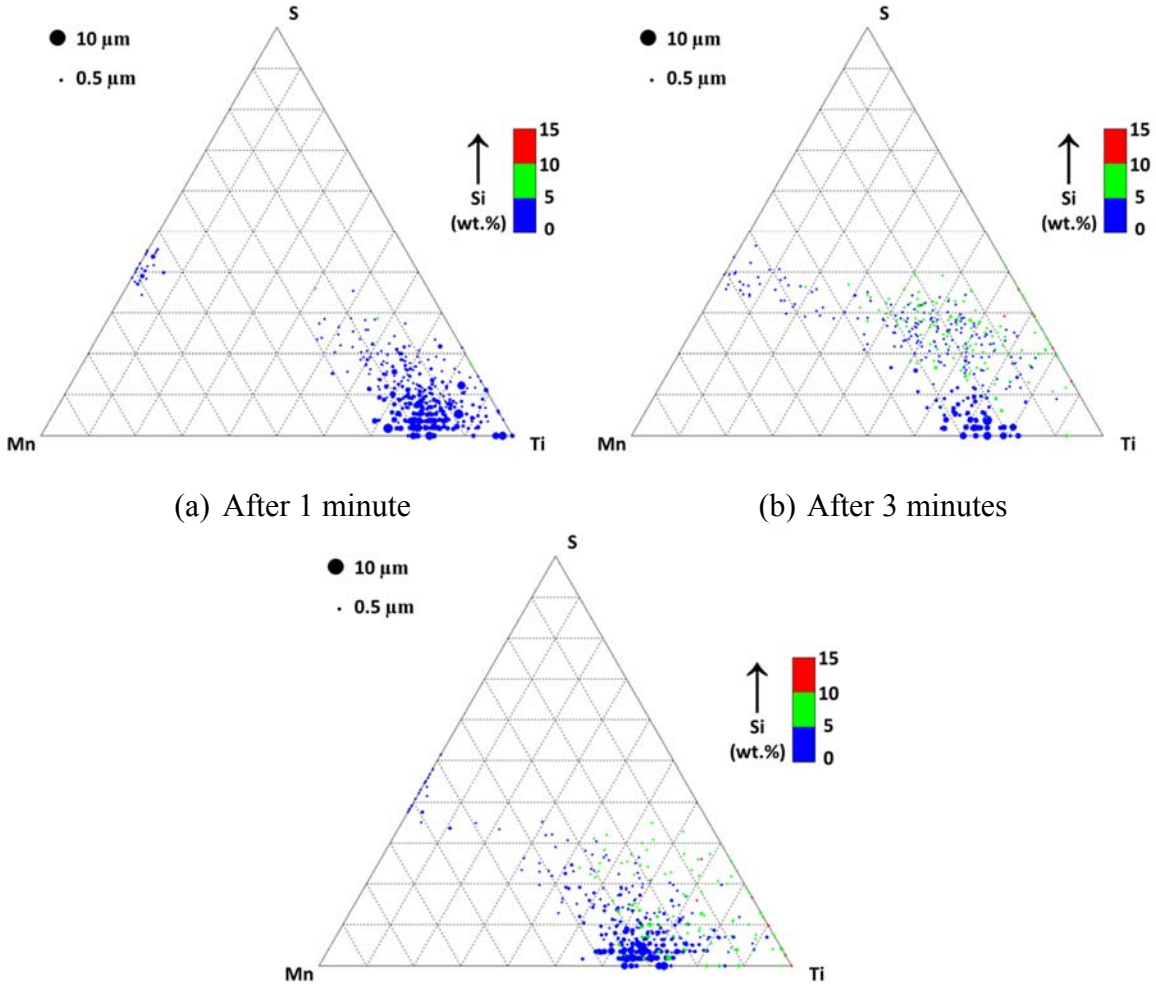

(a) After 1 minute

(b) After 3 minutes

(c) After 5 minutes

Figure 5. Distribution of inclusion composition (wt. %) with time after first FeTi addition for inclusions with low Ca and Al(<10%)

Before any FeTi addition, the average Si content in the inclusions was around 35%. But after the FeTi addition almost all the inclusions were reduced to less than 10% Si. In contrast, the Mn content of the inclusions decreased from about 50-60% to about 30% after the FeTi addition. This suggests that Ti affects SiO_2 more severely than MnO as TiO_2 has a higher affinity for MnO than SiO_2 in the molten oxide phase. TiO_2 and SiO_2 are immiscible solids below 1550°C whereas MnO can form ilmenite and Ti-spinel

solid solutions showing higher affinity for TiO_2.[21,22] Also, MnS inclusions, containing less than 10% Ti or in some cases negligible Ti, were observed, strengthening the hypothesis that these inclusions were formed during solidification. The Mn to S ratio in the inclusion is constant as can be seen from the ternary diagrams. This suggests that MnS precipitation resulted in the formation of these inclusions. With increasing time sulfide inclusions containing Ti also precipitate.

Some inclusions (~15%) with significant amount of Ca and Al (>10%) were also present in the Mn-Si deoxidized steel. These inclusions had low sulfur concentration and were liquid phase (spherical). After the Ti addition these inclusions decreased in number with increasing mixing time. This behavior can be attributed to removal due to floatation after coalescence.

The prominent inclusion types observed in the steel 5 minutes after the first FeTi additions are summarized in Table 7. The oxide inclusions formed were the largest in size, whereas the sulfide inclusions were the smallest inclusions similar to the previous observations. Ti and Mn were the major components of these inclusions.

Table 7. Type of inclusions and their analysis (wt. %) observed after 5 minutes of first FeTi addition (balance O with Ca as minor species)

Type	Population%	Diameter (μm)	S		Mn		Ti		Si		Al	
			min	max	min	max	min	max	min	max	min	max
Oxide	3%	0.6 ± 0.2	0	5	0	5	35	55	5	15	5	15
	1%	0.8 ± 0.2	0	5	0	5	45	55	0	5	0	5
	8%	2.7 ± 1.4	0	5	5	25	25	45	5	15	0	5
	8%	1.0 ± 0.4	0	5	5	15	35	55	0	5	0	5
	1%	1.0 ± 0.6	0	5	5	15	35	45	5	15	5	15
	11%	1.3 ± 0.5	0	5	15	25	35	45	0	5	0	5
	8%	Other Compositions										
Mixed	3%	0.6 ± 0.2	5	15	0	15	35	45	5	15	5	15
	3%	0.7 ± 0.2	5	15	5	25	25	45	5	15	0	5
	7%	0.8 ± 0.3	5	15	5	15	35	55	0	5	0	5
	11%	0.8 ± 0.3	5	15	15	25	25	45	0	5	0	5
	2%	0.9 ± 0.5	5	15	25	35	25	35	0	5	0	5
	10%	Other Compositions										
Sulfide	2%	0.5 ± 0.1	15	25	5	15	25	35	5	15	5	15
	6%	0.6 ± 0.2	15	25	15	35	25	35	0	5	0	5
	1%	0.6 ± 0.2	15	25	15	25	25	35	5	15	0	5
	3%	0.7 ± 0.4	35	45	55	65	0	5	0	5	0	5
	11%	Other Compositions										

A typical oxide inclusion formed after the first FeTi additions are shown in Figure 6. Ti was the major component in these inclusions along with Mn, Si and Al. These inclusions were also spherical in shape having regions of varying Ti-Mn-Si-Al content. This behavior was a result of precipitation of different phases during solidification. The micrograph shows a Ti rich phase precipitated inside the Ti-Mn-Al-Si inclusion. This was possibly pseudobrookite (Ti_3O_5), which were also predicted by thermodynamic calculations.

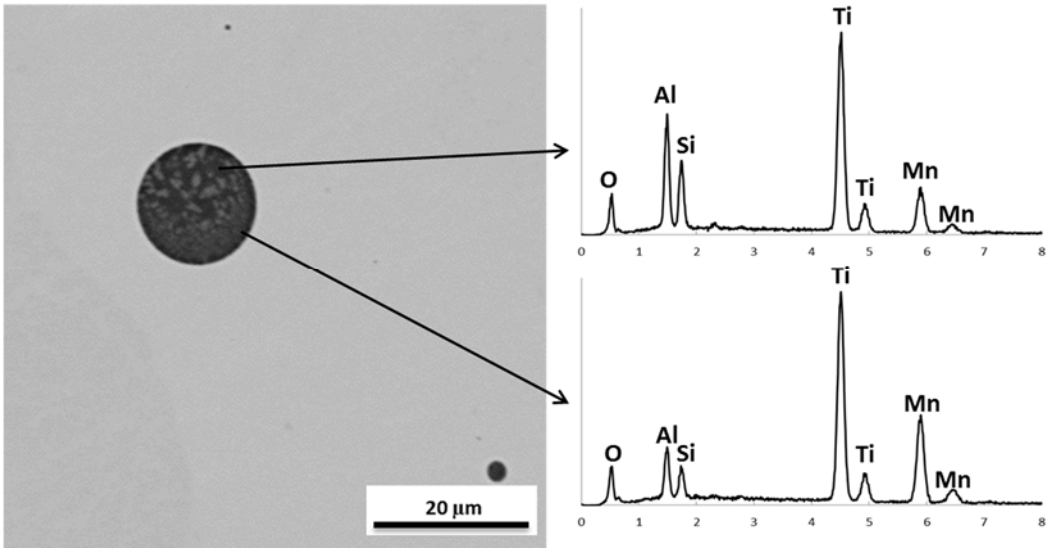

Figure 6. Typical Ti-Mn-Al-Si-O oxide inclusion,with Ti rich phase as precipitates, observed 5 minutes after first FeTi addition

Thermodynamic model described in Table 2 (b) was used to study inclusion transformation on FeTi addition. Table 8 shows a sample calculation using inclusion compositions from different categories similar to Table 5. The inclusion chemistries obtained 5 minutes after Fe75Si + FeMn addition (Table 4) and steel composition obtained 1 minute after the first FeTi addition (Table 6) were used. The oxide inclusions transformed by gaining TiO_x and losing MnO, SiO_2 or both. The drop in Si content of the inclusion was more than the Mn content similar to the behavior observed experimentally. Similar to the previous case mixed and sulfide inclusions were predicted to dissolve at 1600°C.

Table 8. A representative result for the thermodynamic calculations to show inclusion transformation on FeTi addition at 1600°C

			Avg. inclusion composition (wt. %)			
Type		Steel	Oxide (1)	Oxide (2)	Mixed	Sulfide
Initial	S	0.01	2.5	1.7	9	32.6
	Mn	0.66	27.9	18.9	32.4	33.3
	Si	0.13	26.6	29.9	20.8	13.7
	Ti	0.02	0.2	0.5	0.3	0.1
	Al	-	3.2	6.3	5.7	7
	100 g inclusion + 100,000 g steel					
Final	Slag wt. (gram)		91.7	99.8	74.5	30.7
	S		0.0	0.0	0.0	0.0
	Mn		20.7	20.1	17.7	4.0
	Si		11.5	11.4	8.2	1.2
	Ti		19.8	18.2	23.2	31.5
	Al		4.5	7.2	8.7	19.0
	Prediction		Equilibrium	Equilibrium	Non-equilibrium	Non-equilibrium
	Change in inclusion		$MnO\text{-}SiO_2$ Loss/ TiO_x gain	SiO_2 loss/ TiO_x gain	Sulfides dissolve	Dissolution

As the oxide inclusions were reacted with steel containing higher Ti (0.02%), after the first FeTi addition, they were predicted to form Mn-Ti-Si-Al type oxide inclusions. The equilibrium calculations predicted TiO_x content of about 30% with Mn:Ti ratio close to 1:1, whereas, as per the experimental data (Table 6) Mn:Ti ratio was close to 1:2 suggesting that complete equilibrium was not achieved after 5 minutes. For the mixed inclusions, the sulfide concentration of the inclusions dropped to less than 1% and their predicted behavior (after the sulfide loss) was similar to the oxide inclusions. After the second FeTi addition, ternary plots were drawn using the same settings as were used for the first additions. Figure 7 shows the mapping of the inclusions on the ternary plot.

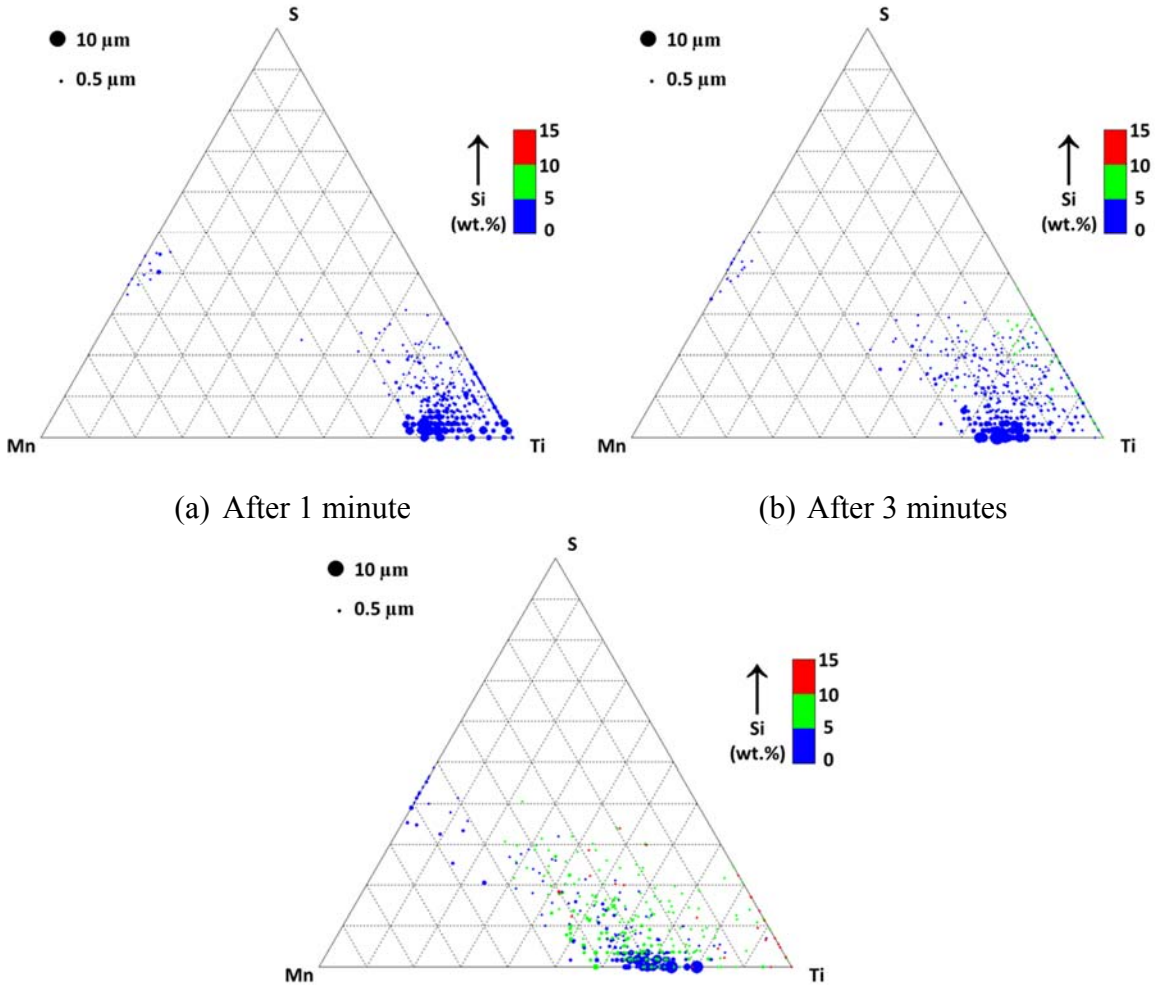

(a) After 1 minute

(b) After 3 minutes

(c) After 5 minutes

Figure 7. Distribution of inclusion composition (wt. %) with time after second FeTi addition for inclusions with low Ca and Al(<10%)

Similar to the first FeTi addition, the Ti/(Ti+Mn+S) ratio increased towards 100% immediately after the addition and with time shifted to about 70% by gaining Mn. This could happen as a result of the following equilibria:

$$3(MnO)_{inclusion} + 2[Ti] = (Ti_2O_3)_{inclusion} + 3[Mn] \quad (1)$$

$$2(MnO)_{inclusion} + [Ti] = (TiO_2)_{inclusion} + 2[Mn] \quad (2)$$

The high Mn content in the steel drives the reaction (1 and 2) in the reverse direction which is aided by the high affinity of MnO to TiO_2/Ti_2O_3. The SiO_2 content in the inclusions was negligible just after the second FeTi addition, although some re-oxidation of silicon took place with time probably during multiple sampling steps which caused an increase in the Si content in the inclusions observed in the final sample (Figure 7). A gain in total oxygen content was observed with subsequent sampling steps as shown in Table 6. An example of SiO_2 rich inclusion is shown in Figure 8. Also, the MnS behavior was similar, to the previous case, in addition to the formation of some titanium sulfide inclusions. Other inclusions, richer in Ca and Al (>10%) further decreased after the second FeTi addition.

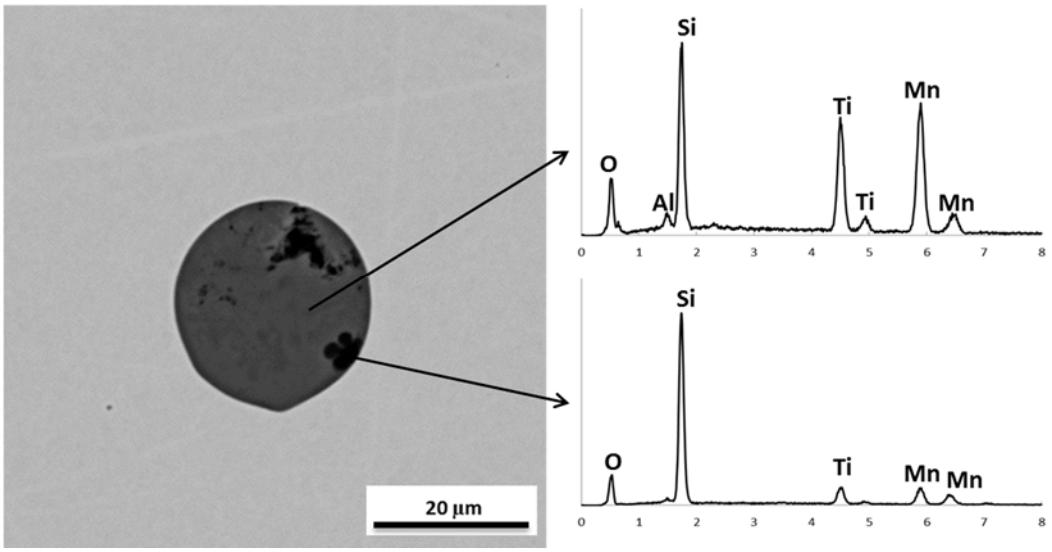

Figure 8. SiO_2 precipitate in Si-Mn-Ti-Al-O inclusion observed 5 minutes after second FeTi addition

The prominent inclusion types observed in the steel, 5 minutes after the second FeTi additions are summarized in Table 9. Similar to the previous case, the oxide inclusions formed were the largest in size, whereas the sulfide or mixed inclusions were the smallest. Some oxide inclusions with only Ti and Mn were observed to have an average diameter of about 5 μm (Figure 7).

Table 9. Type of inclusions and their analysis (wt. %) observed after 5 minutes of second FeTi addition (balance O with Al and Ca as minor species)

Type	Population %	Diameter (μm)	S		Mn		Ti		Si	
			min	max	min	max	min	max	min	max
Oxide	2%	0.6 ± 0.1	0	5	0	5	35	45	5	15
	5%	1.7 ± 1.4	0	5	5	15	35	55	0	5
	7%	0.7 ± 0.2	0	5	5	15	35	45	5	15
	8%	1.0 ± 0.4	0	5	15	25	25	45	5	15
	21%	1.9 ± 1.5	0	5	15	25	35	45	0	5
	7%	Other Compositions								
Mixed	2%	0.5 ± 0.1	5	15	0	5	35	45	5	15
	6%	0.6 ± 0.2	5	15	5	15	25	45	0	5
	1%	0.5 ± 0.1	5	15	5	15	35	45	0	5
	7%	0.7 ± 0.2	5	15	15	35	25	45	0	5
	12%	0.7 ± 0.2	5	15	25	45	25	45	5	15
	4%	Other Compositions								
Sulfide	5%	0.5 ± 0.1	15	25	5	35	25	35	5	15
	2%	0.5 ± 0.2	15	25	15	35	25	35	0	5
	2%	0.7 ± 0.3	15	25	25	45	15	25	0	5
	1%	0.8 ± 0.4	35	45	55	65	0	5	0	5
	8%	Other Compositions								

Similar to the previous case, inclusion transformation due to the second FeTi addition was studied thermodynamically using the model shown in Figure 2 (b). Inclusion chemistries obtained 5 minutes after the first FeTi addition (Table 7) were

reacted to steel composition obtained 1 minute after the second FeTi addition (Table 6). Oxide inclusions were predicted to gain Ti and lose Si to steel and form liquid phase inclusions with about 5-10% Mn and Al depending on their initial composition. These inclusions were predicted to have about 80% TiO_x and less than 5% FeO. The SiO_2 content was predicted to be negligible (<1%). The ternary plot drawn after the second FeTi addition shows this behavior after 1 and 3 minutes of the addition (Figure 7 (a) and (b)). The equilibrium calculations confirm that re-oxidation was the source of the Si rich inclusions observed experimentally (Figure 7 (c)).

From the ternary plots (Figure 9), the changes in inclusion chemistry with time after the third FeTi addition can be observed. Immediately after the FeTi addition the Si content of the inclusions dropped to zero which increased to less than 5% with time. The Ti/(Ti+Mn+S) ratio in the inclusions also dropped with time and after 5 minutes most of the inclusions had Ti/(Ti+Mn+S) ratios between 75% and 90%. The gain of Mn to Ti rich inclusions was significantly less compared to previous additions, suggesting that TiO_2/Ti_2O_3 (TiO_x) saturation was achieved in the inclusions. Further, the change in inclusion composition with time was not as significant as in the previous cases. The S rich inclusions were predominantly MnS.

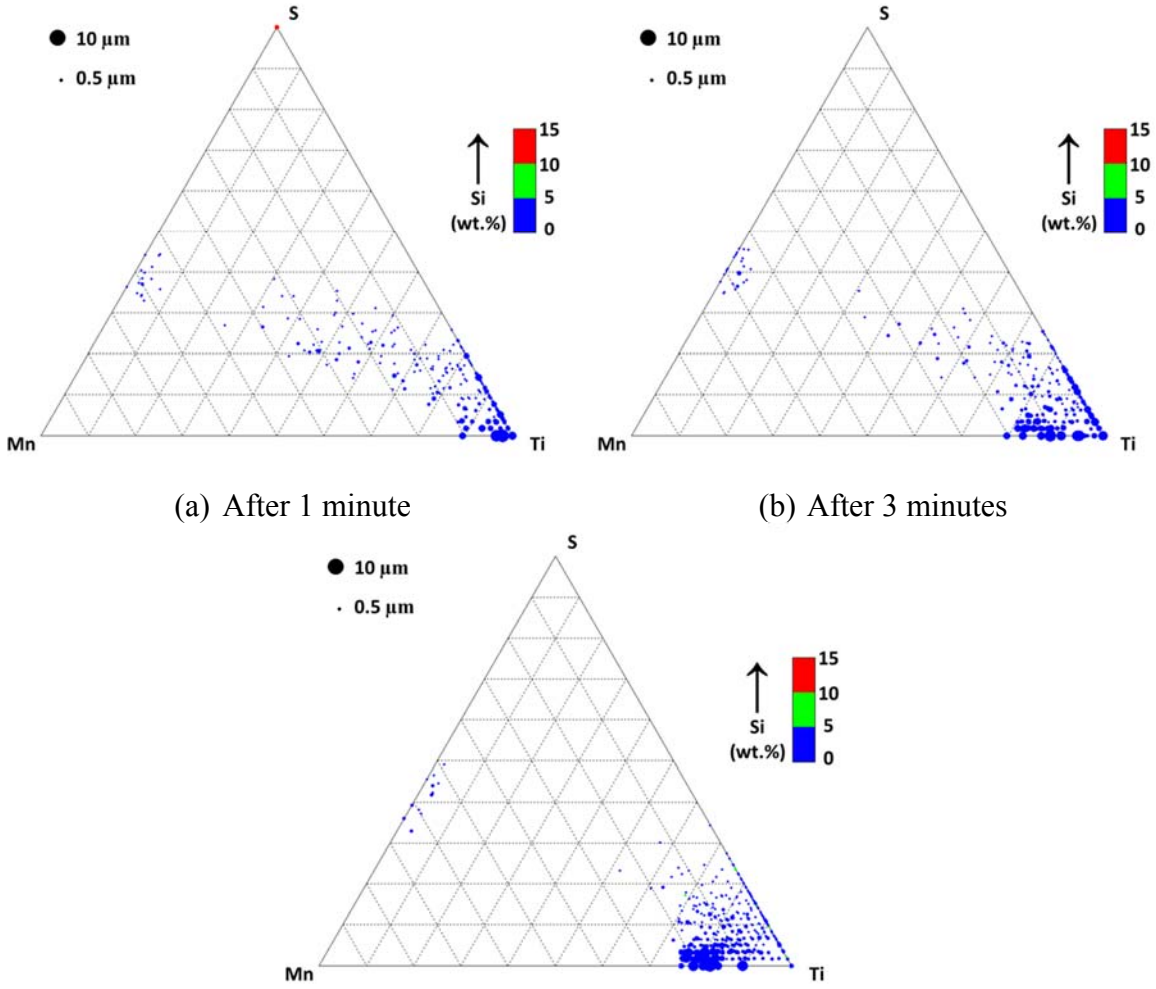

(a) After 1 minute

(b) After 3 minutes

(c) After 5 minutes

Figure 9. Distribution of inclusion composition (wt. %) with time after third FeTi addition for inclusions with low Ca and Al(<10%)

The prominent inclusion types observed in the steel 5 minutes after the third FeTi additions are summarized in Table 10. Almost all the Ti-based inclusions contained small amounts of Mn or Al or both. A few pure TiO_x inclusions were also observed. The Si content in all the inclusions was reduced to less than 5%. The amount of Al or Mn in the inclusions depended on the initial composition of the inclusions. With increasing Ti,

all the Mn can be removed from some of the inclusions. MnS precipitation on the existing Ti-Al-O inclusions during solidification could be the cause of the higher Mn content in the inclusions. Typical inclusions formed after the third FeTi addition, were similar in morphology to the inclusions observed earlier except for their higher Ti content.

Table 10. Type of inclusions and their analysis (wt. %) observed after 5 minutes of third FeTi addition (balance O with Ca and Si as minor species)

Type	Population %	Diameter (μm)	S		Mn		Ti		Al	
			min	max	min	max	min	max	min	max
Oxide	15%	0.8 ± 0.3	0	5	0	5	45	65	0	5
	3%	0.8 ± 0.4	0	5	0	5	45	55	5	15
	27%	1.9 ± 1.5	0	5	5	15	45	55	0	5
	3%	3.8 ± 2.9	0	5	5	15	45	55	5	15
	4%	Other Compositions								
Mixed	17%	0.6 ± 0.2	5	15	0	5	45	65	0	5
	6%	0.5 ± 0.1	5	15	0	5	45	55	5	15
	11%	0.7 ± 0.3	5	15	5	15	35	55	0	5
	3%	Other Compositions								
Sulfide	1%	0.4 ± 0.1	15	25	0	5	45	55	0	5
	1%	0.7 ± 0.5	35	45	55	65	0	5	0	5
	9%	Other Compositions								

As per the thermodynamic calculations, when the oxide type inclusions were reacted with steel of higher Ti concentration (third FeTi addition) liquid slag inclusions with about 85% TiOx content were predicted confirming the experimental data represented in Figure 9. MnO and Al_2O_3 content were predicted to be around 5%. In the slag phase, SiO_2 content was predicted to be less than 1%, MnO was around 5% and TiOx was 85%. Oxide inclusions that initially had only Ti and Mn were predicted to form solid Ti_3O_5.

Overall with increasing FeTi addition, the TiO_x content increased in the inclusions from 30% to 85%. The inclusions were predicted to form liquid phase at 1600°C and solid Ti_3O_5 phase was predicted only after the third FeTi addition. Ti addition affected the Si and Mn content of the inclusions but the Al content remained constant. The MnO in inclusions decreased gradually with each step whereas the SiO_2 content was calculated to drop to less than 1% after the first FeTi addition. Sulfide content less than 1% was in equilibrium with steel at 1600°C and would increase only on cooling.

The oxide inclusions increased from about 25% (after Fe75Si + FeMn addition) to 45% (after third FeTi addition) showing that all the inclusions were not affected by Mn and S segregation. Presumably the oxide inclusions were not "pushed" by the solid/liquid interface, and so were isolated in solid steel early in the solidification process. Many inclusions were present in the solidified steel before significant segregation occurred in the remaining liquid and therefore remained as oxide. The mixed/sulfide inclusions must have formed at lower temperatures and in inter-dendritic regions with Mn and S segregation. Hence only a fraction of the inclusions are of the types mixed and sulfide. The high fraction of oxide inclusions after the third FeTi addition and hence the formation of solid Ti_3O_5 inclusions suggests that too much FeTi was added. So, to achieve inclusion modification (without any solid inclusions), adding a small fraction of FeTi in steps would be more effective.

After each ferro-alloy addition and a mixing time of 5 minutes, number of inclusions and coverage area were calculated and shown in Figure 10 (a). From the plot it can be observed that the inclusion count dropped after the first FeTi addition along with the inclusion coverage. This behavior would be a result of removal of larger inclusions.

After the second FeTi addition, the inclusion count increased slightly with a greater increase in the inclusion coverage indicating increase in inclusion size. Increase in inclusion size can be attributed to coalescence of liquid inclusions. The inclusions at this stage were smaller in number and coverage than those observed after the initial Fe75Si + FeMn addition. After the third addition, the number of inclusions dropped but the coverage increased owing to similar coalescence behavior. The average inclusion size would be much larger compared to the inclusions observed after Fe75Si + FeMn addition. This behavior suggested that the inclusions were agglomerating to form larger inclusions.

Figure 10 (b) shows the amount of the different elements in the inclusions divided by the total elements in the samples in ppm values at 5 minutes after different ferro-alloy additions. It was observed that the addition of FeTi resulted in drop of Mn and Si content of the inclusions. The drop was more predominant in case of Si than Mn as explained earlier. Mn and Si content in the inclusions would be replaced by the Ti from the FeTi added which was also confirmed by the thermodynamic calculations. Thermodynamic calculations showed no change in the Al and Ca component of inclusions due to the FeTi addition. The sulfur content of the inclusions also dropped with addition of FeTi.

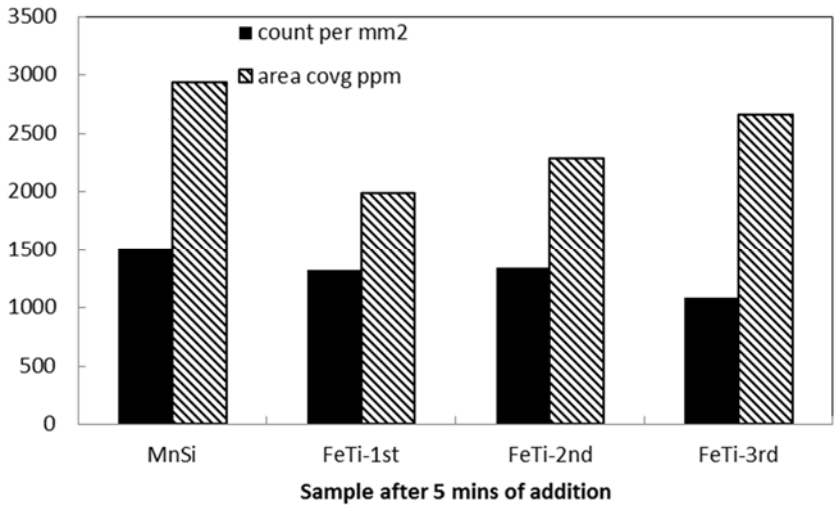

(a)

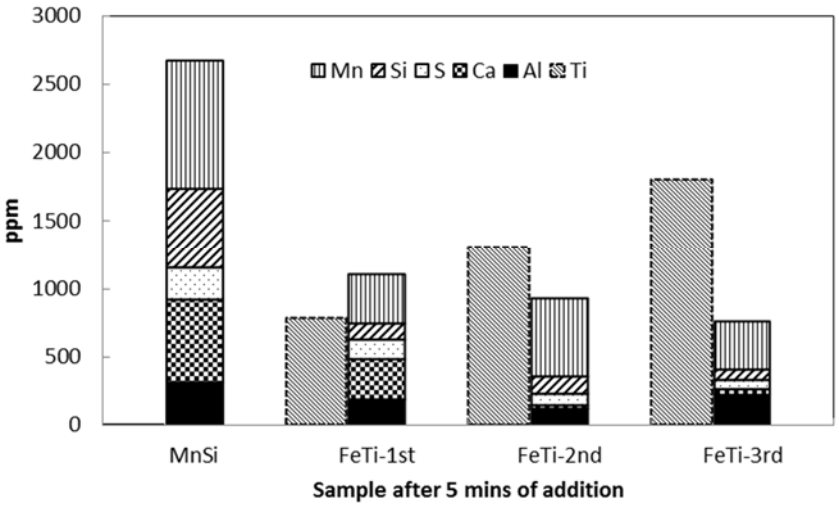

(b)

Figure 10. Inclusion variations at different stages in the experiment: (a) inclusion count per mm^2 and area of inclusions per mm^2 (coverage) and (b) amount (in ppm) of each element in the inclusions.

5. CONCLUSIONS

In the present study, Mn-Si-Al-O based solid/liquid inclusions were modified with Ti additions. Experiments and thermodynamic modeling was performed to assess the effects of Ti addition on inclusions in Mn-Si killed steel. Inclusion composition was plotted using a quaternary system to observe inclusion evolution with time. Inclusions were divided into categories based on their compositions and these compositions further used to study thermodynamic equilibrium with steel. The following conclusions can be drawn from this study:

1. FeTi addition transformed all the existing inclusions in the Mn-Si killed steel by enriching the inclusions with Ti to form liquid inclusions.
2. Both Si and Mn were removed from the inclusions with FeTi addition. Si removal was more predominant than Mn. Si content was reduced to less than 5% after the second FeTi addition and was almost negligible after the third addition. However, Mn was not removed completely. This behavior can be attributed to the higher affinity of Ti-oxide for MnO than SiO_2. FeTi addition should be added in small fraction to achieve effective modification with the inclusions remaining liquid.
3. The Al content in the inclusions did not change compared to the initial composition. Most of the inclusions formed at temperature were Ti-Al-Mn-O based complex inclusions. These inclusions precipitated Ti-rich phase on solidification. MnS also precipitates on these inclusions.
4. Sulfide inclusions were formed as a result of MnS formation during solidification. This phase can precipitate on existing oxide inclusions to

form mixed inclusions, since MnS was observed in inclusions both as a separate phase or in solution. Due to changes in composition on cooling and solidification (with Mn and S segregation), about 1/3rd of the inclusions were mixed and about 1/6th were sulfides. The relative amounts of these inclusions would depend on the relative oxygen and sulfur levels in the steel.

5. Ti addition can be used to modify inclusions in Si-Mn killed steels especially low Mn steels where solid SiO_2 inclusions are a major cause of concern.

ACKNOWLEDGEMENTS

The authors would like to express their sincere appreciation and gratitude for the late Professor Kent D. Peaslee for providing guidance and support for this research and for always being an inspiration for us.

REFERENCES

1) L. Zhang and B.G. Thomas: *ISIJ Int*., 43 (2003), 271.

2) K. Rackers and B.G. Thomas: 78th Steelmaking Conf. Proc., Iron and Steel Society, Warrendale, PA, (1995), 723.

3) L. Zhang and B.G. Thomas: XXIV National Steelmaking Symp., Morelia, Mich, Mexico, (2003), 138.

4) L. Zhang, S. Taniguchi and K. Cai: *Metall. Mater. Trans. B*, 31 (2000), 253.

5) L. Zhang and S. Taniguchi: *International materials reviews*, 45 (2000), 59.

6) B. H. Yoon, K. H. Heo, J. S. Kim and H. S. Sohn: *Ironmaking Steelmaking*, 29 (2002), 214.

7) Y. Murakami, S. Kodama and S. Konuma: *International Journal of Fatigue*, 11 (1989), 291.

8) M. Lind and L. Holappa: *Metall. Mater. Trans. B*, 41 (2010), 359.

9) R. B. Tuttle, J. D. Smith and K. D. Peaslee: *Metall. Mater. Trans. B*, 36 (2005), 885.

10) S. Chakraborty and Y. Sahai: *Metall. Mater. Trans. B*, 23 (1992), 135.

11) L. Zhang, J. Aoki and B. G. Thomas: *Metall. Mater. Trans. B*, 37 (2006), 361.

12) B.G. Thomas, A. Dennisov, and H. Bai: 80th Steelmaking Conf., ISS, Warrendale, PA, (1997), 375.

13) Y. Miki, B.G. Thomas, A. Denissov and Y. Shimada: *Iron & steelmaker*, 24 (1997), 31.

14) E.T. Turkdogan: “Fundamentals of Steelmaking”, The Institute of Materials, London, (1996), 285.

15) E. B. Pretorius and R. Marr: 53rd Electric Furnace Conf. Proc., Iron and Steel Society, Orlando, (1995), 407.

16) C.W. Bale, P. Chartrand, S.A. Degterov, G. Eriksson, K. Hack, R. Ben Mahfoud, J. Melancon, A.D. Pelton and S. Petersen: *Calphad Journal*, 26 (2002), 189.

17) Y. Kanga, I. Jung and H. Lee: *Calphad Journal*, 30 (2006), 226.

18) H. Amitani, K. Morita and N. Sano: *ISIJ Int*., 36 (1996), S26.

19) Z.T. Ma and D. Janke: *Acta Metallurgica Sinica*, 11 (1998), 79.

20) H. Kim, H. Lee and K. Oh: *ISIJ Int*., 42 (2002), 1404.

21) M. Kiviö and L. Holappa: *Metall. Mater. Trans. B*, 43 (2012), 233.

22) G. Eriksson and A.D. Pelton: *Metall. Mater. Trans. B*, 24 (1993), 795.

III. A KINETIC MODEL FOR VACUUM TANK DEGASSING

Vivek Thapliyal

Simon N. Lekakh

David G. C. Robertson

Jeffrey D. Smith

Materials Science and Engineering

Missouri University of Science & Technology

Rolla, MO

Phone - 573-341-6469,

E-mail – vtty6@mst.edu

To be submitted for publication in ISIJ International

ABSTRACT

Vacuum tank degassing is used as a unit process in secondary steelmaking to remove nitrogen, hydrogen, carbon, sulphur, oxygen and other elements from steel. Even though the pressure inside the vacuum tank degasser (VTD) is low, the actual pressure felt by the liquid metal varies with depth of the ladle due to the metallo-static effects. The melt is always stirred by argon, so that over time the whole volume of steel experiences the low pressure at the top surface of the melt. The pressure in the vacuum chamber and the argon flow rate both vary with time. A detailed kinetic model of the process has been developed taking into account the stirring of the melt by argon, the mass transfer into the rising argon bubbles, the steel/slag/gas reactions at the top surface of the melt, and spontaneous formation of CO bubbles in the upper regions of the melt where the pressure is low enough for CO bubble growth to occur. A particular feature of the model was that the chemistry of the reactions was very accurately modelled by using FactSage 6.4. This kinetic model provides a valuable tool to study the reactions occurring at different local conditions in the VTD.

Key Words: Vacuum tank degassing, steel, modeling

1. INTRODUCTION

Vacuum degassing is widely used as a secondary steelmaking process to achieve low concentrations of nitrogen, hydrogen, carbon, sulphur, and other elements in steel. Ruhrstahl Heraeus (RH) degasser and vacuum tank degasser (VTD) are the two most widely used reactors for this purpose. Researchers have used various models to study the degassing process in both these reactors.[1-8] Most of these models focus on the de-carburization (de-C) process.

Previously, a dynamic model for the VTD using computational fluid dynamic software (FLUENT 6.2[9]) and process simulator software (METSIM[10]) was developed by the authors.[1] The databases and "extent of reaction" feature available in METSIM were utilized for de-C reaction. It was identified that for a more sophisticated model the following changes were required: (a) incorporation of changes in the flow pattern due to spontaneous CO evolution, (b) variation of mass transfer rate to reaction interfaces, with different argon (Ar) flow rates, (c) extension of the model to include non-metallic inclusion formation and steel cleanliness, and (d) utilization of thermodynamic databases available in FactSage 6.4[11].

In the present study, a dynamic model for the VTD has been developed by using databases and macro-language available in FactSage software. This allowed to include solid compounds and solid-solutions in the equilibrium calculations along with all the possible gases. Van Ende et al.[2] developed a kinetic model for the RH degassing process by utilizing the macro-language feature available in FactSage to link thermodynamic databases to the process parameters. A similar approach has been utilized by researchers to study steel/refractory/inclusion and steel/refractory interactions.[12,13]

Computational fluid dynamics (CFD) has been used to provide data for the melt flow, which was driven by the injection of argon. Processing data from a typical heat in industrial practice were used as input to the CFD calculations. The pressure above the melt and the argon flow rate were important inputs which varied with time during a heat.

Sampling during VTD processing without disrupting the vacuum is difficult. Therefore, a dynamic model which could predict steel chemistry during processing in the VTD, would be very useful. The system was simplified by dividing the melt volume into zones. The volume of the zones and the melt flow between the zones was determined based on the CFD calculations. Thermodynamic calculations were performed for different local conditions in these zones using FactSage. The results were compared to industrial data for model verification.

2. VTD MODEL CONCEPT

In a VTD, vacuum is applied to liquid steel in a ladle. Even though the applied pressure during the VTD processing can be as low as $1x10^2$ Pa, the local pressure (pressure applied + metallo-static pressure) in the melt is much higher. Also, the local pressure is not the same throughout the ladle volume. At the bottom of a ladle (with liquid metal height ~3 m) the metallo-static pressure is $2x10^5$ Pa. The effect of the applied vacuum is observed only in the top region. During the degassing process, CO gas-bubbles are generated in this top region which causes mixing. Mixing is further increased by flowing Ar into the ladle through porous plugs at the bottom of the ladle. The present model was designed to represent the conditions within the ladle by dividing the ladle volume into multiple zones. Figure 1 shows a representation of the model having the following zones:

(a) Zone-0 – Liquid steel in this zone was in contact with slag. This zone supplied liquid steel to steel/slag/gas interface. Ferro-alloy additions were made in this zone. Spontaneous de-C also occurred in this zone.

(b) Zone-1 – In this zone, degassing reactions occurred in steel under local pressure. A fraction of material entering this zone was assumed to participate in the spontaneous de-C reaction. The fraction of steel undergoing de-C was equilibrated at the local pressure shown as FEM 1 (Figure 1). This zone was not in line with the Ar plume and has predominantly downward flow.

(c) Zone-2, Zone-3 and Zone-4 – These were the regions without any spontaneous degassing reactions due to high local pressure ($>0.5x10^5$ Pa).

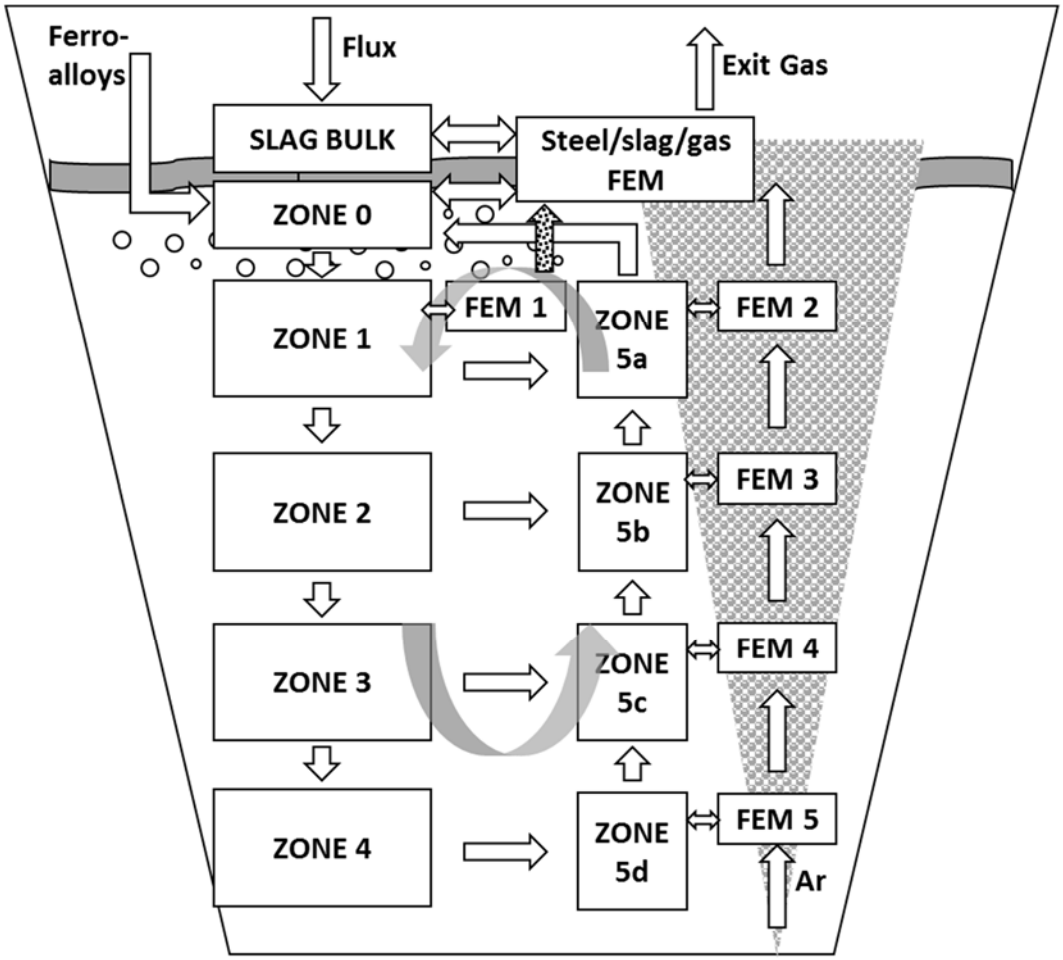

Figure 1. Illustration of VTD multi-zone model. Zone-5 which forms the zone over the Ar-plug was further divided into 4 parts parallel to Zones 1, 2, 3 and 4. FEM 1 represents fraction of steel for which spontaneous CO formation is calculated every time-step. FEM's 2-5 represent steel/gas-bubble interfaces.

(d) Zone-5 – This zone was in line with the Ar plume and had predominantly upward flow. This zone was sub-divided into four layers each at the levels of zones 1-4. These zones supplied liquid steel to steel/gas-bubble interface.

(e) Slag-bulk – This zone supplied slag to the steel/slag/gas interface. Slag additions were made to this zone.

(f) FEM-steel-slag – This zone represented the steel/slag/gas interface. Thermodynamic equilibrium was computed at this interface.

(g) FEM-steel-gas – This zone represented the steel/gas-bubble interface. Four such zones were used each for zone-5 sub-divisions shown as FEM 2-5 in Figure 1.

In zones 0-5, homogenization of steel was also performed at every time-step. The steel represents liquid metal containing solid and liquid inclusions.

2.1. Determination of Zone Volumes and Mixing in the Ladle

The zone volumes and expected flow pattern in the liquid steel were established using CFD simulation, for which the volume of fluid (VOF) multiphase model and k-epsilon turbulent flow model were used in FLUENT. Three phases, namely liquid steel, Ar and carbon monoxide (CO) gas were used. The CFD simulations were run for 100 tonne ladle (14.7 m^3 of melt approximately). The melt domain was divided into 5 equal horizontal zones with permeable "interior" type boundaries whereas the top boundary was treated as a pressure outlet. Ar was injected into the ladle from two porous plugs at the bottom. The Ar flow rate was varied in the range 2 to 76 scfm. The results were evaluated to determine the average melt velocity in each volume and melt flow exchange between these volumes. Iso-surfaces for velocity $v_Z = 0$ (velocity in the vertical Z-direction) were plotted for each horizontal plane (Figure 2). Melt flow in the vertical direction was determined by multiplying the area of these iso-surfaces and the averaged negative or positive v_Z values. Volume for each zone was calculated by multiplying the iso-surface area with the height of each zone. These calculated melt flow rates and volumes varied with the Ar flow rates.

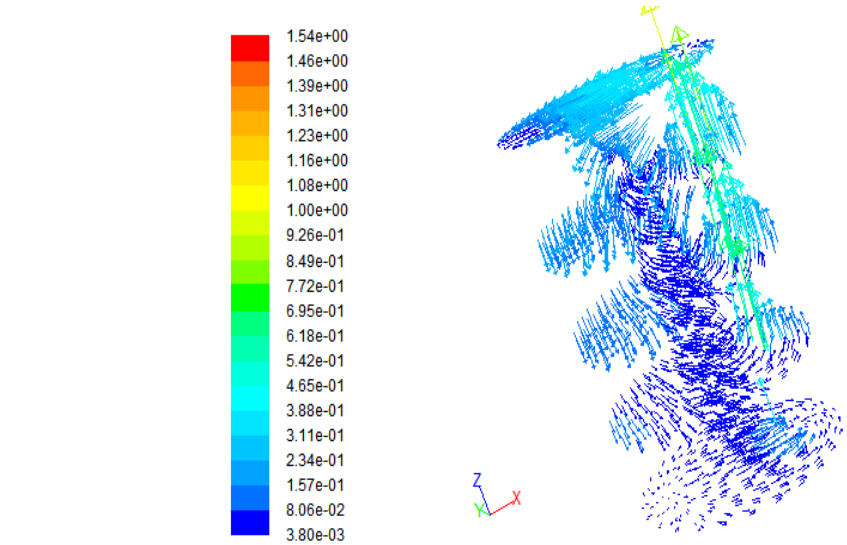

(a)

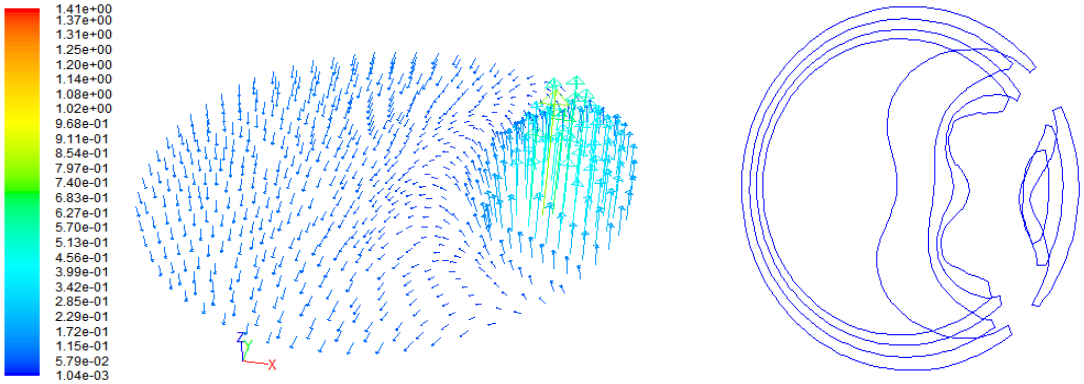

(b) (c)

Figure 2. Illustration of a) vector velocity in ladle domain and b) cross section, and c) position of iso-lines Vz=0 in different cross sections

Mixing times for different Ar flow rates (without internal CO evolution) were evaluated for the CFD model by introducing tracers to the top region. The concentrations at different levels were monitored. The time for complete mixing (mixing time) was assumed to be the time at which the standard deviation of the tracer concentration about

the mean equaled 1%. After CFD calculations, a reactor model (based on conservation of mass) was developed in Microsoft Excel (Microsoft Corporation, Redmond, WA) using CFD results. For this Excel model the VTD volume was divided into different zones (Figure 1) assuming ideal mixing in each zone, thus representing the model design used in the present work. The predicted mixing time calculated by CFD calculations and Excel reactor model were compared to published data using non-dimensional analysis [14] and found to be in good agreement (Figure 3).

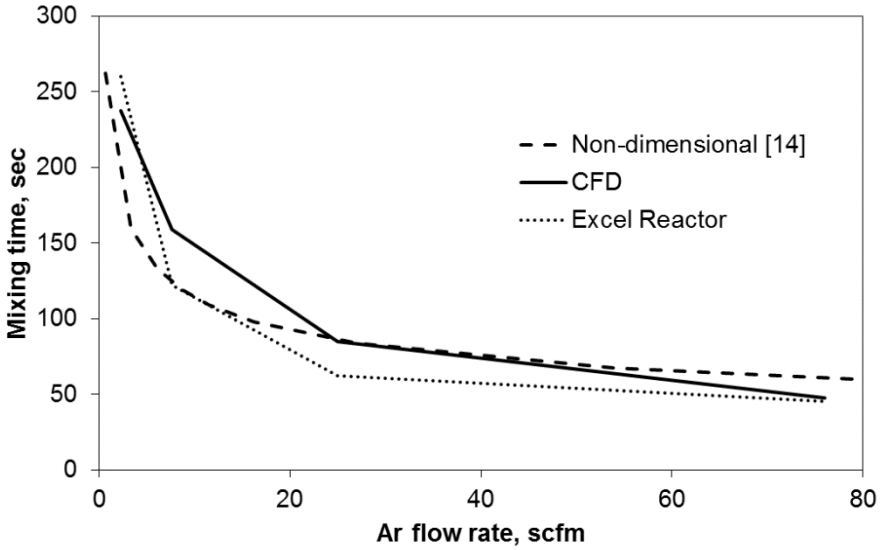

Figure 3. Mixing time for different Ar flow rates for different mixing models

2.2. Model Design

Based on the CFD results, the volume of each zone and flow between any two zones was determined as a function of Ar flow rate. To represent each zone, a structure similar to the basic reactor unit developed by Robertson[15] was used, as shown in Figure 4. This approach was also used in the previous work.[1] Each zone was designed with a

recirculating stream (bulk phase) which represents the volume of the zone. In the basic reactor unit the recirculating stream, flow from previous zone (feed stream) and flow from reaction interface (if any) are mixed together and then the aggregate flow stream is split into the recirculating stream, flow to the next zone and flow to the reaction interface. Each of the individual zones was assumed to be a perfectly mixed reactor. Basic reactor units for each zone were combined to form the complete model. Reaction interfaces were modeled by using separate units, shown as FEM in the Figure 4. Flow to these units was calculated by using mass transfer coefficients and interface area. Thermodynamic equilibrium was calculated for the volume per unit time using FactSage under local conditions. The reacted volume (with equilibrated composition) was returned back as input to the basic reactor unit. Each zone had a different local pressure, calculated by using the average depth of the zone. Additionally, a similar unit reactor was used for the slag phase. Thermodynamic equilibria at reaction interfaces were calculated at each time step.

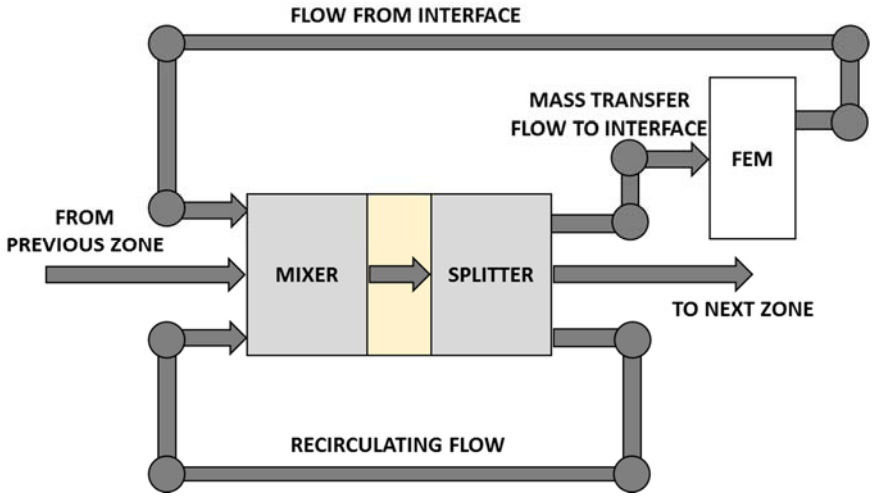

Figure 4. Illustration of general structure of each zone of the model. Each zone has one recirculating stream, which represents the volume of that zone.

To design this model, “Equilib” module of FactSage was used. “Equilib” files were created in FactSage for reactions taking place at the interface and during mixing in the bulk phase. The sequence of calculations was written using the macro language provided in the FactSage software. The macro was linked to a Microsoft Excel workbook to read input values and write outputs of the thermodynamic calculations. The stream flow-rates and pressure were provided as input to the “Equilib” files using the Excel workbook. The results of these calculations in terms of the volume and composition of reacted species were written as output into the Excel workbook. The output data at a given time-step was used as an input for the subsequent time-steps.

For thermodynamic calculations in FactSage the databases used were: a) FSstel database (solution database used for liquid steel), b) FactPS database (for gas species and solid compounds), and c) FToxid database (for slag solution, solid solutions and solid compounds). For equilibrium calculations at a reaction interface all possible gas phases, solids and solution phases were used. Whereas for mixing calculations, only the reacting phases were chosen as products. All the calculations were performed at 1600°C.

De-carburization of steel in a VTD occurs mainly by three mechanisms: i) spontaneous CO bubble evolution due to reduced pressure; ii) reaction at the steel/gas-bubble interface; and iii) reactions at the steel/slag/gas interface with an FeO containing slag. These three mechanisms have been modeled as follows:

2.3. Spontaneous Bubble Formation

Spontaneous CO gas bubble formation occurs in liquid steel when the equilibrium partial pressure of CO gas exceeds the local pressure as a result of the following reaction:

$$[C]_{steel} + [O]_{steel} = CO(gas) \quad (1)$$

This reaction occurs in the top zone in the ladle where the local pressure is low. At a given depth in the steel, local pressure is a sum of the applied pressure at the surface and the metallo-static pressure due to steel and slag depth, given by:

$$P_l = P_a + \rho_m g h_m + \rho_s g h_s \quad (2)$$

where,

P_l= local pressure in the melt

P_a = applied pressure above the surface

ρ_m = density of steel, 7200 kg/m^3

g = acceleration due to gravity, 9.81 m/s^2

h_m= depth of steel column above the point at which local pressure is being calculated, m

ρ_s = density of slag, 3500 kg/m^3

h_s = thickness of the slag layer above the melt, m

Researchers have suggested that CO bubbles can either self-nucleate (homogeneous nucleation) or nucleate over inclusions in the steel or the ladle wall.[16-19] Researchers have reported that for spontaneous growth of CO bubbles supersaturation pressure is required.[16,17] Anghelina et al.[16] have reported this supersaturation pressure to be equivalent to that required to offset the surface tension for a 1.1 mm CO bubble (~7x10^3 Pa). El-Kaddah et al.[19] reported the superstation required for CO bubble nucleation in levitated iron drops to be as low as 1x10^6 Pa at high oxygen potentials.

In the present work, it was assumed that CO bubble growth was the limiting condition as there were enough heterogeneous nucleation sites (inclusions and refractory surface). If the local pressure dropped below pCO (growth possible) then CO bubbles formed 'spontaneously', by some undefined mechanism. The CO bubble generation creates vigorous mixing in the top region. It was assumed that spontaneous CO bubble formation only occurs in zone 1 where the local pressure is low. In the lower zones (zone 2 - 4, 5b - 5d), the local pressure was greater than $0.5x10^5$ Pa. The amount of CO bubble formation would depend on the number of available nucleation sites and carbon diffusion in the melt. To account for this, it was assumed that a fraction ($1/5^{th}$) of liquid metal under-goes spontaneous de-carburization in one time-step. Even though the choice of this fraction is arbitrary it allows for an easy representation of this complicated process which is still a subject of debate among researchers.[16-19] This fraction can be varied and made a function of carbon diffusivity, inclusion density, CO super-saturation required for growth, stirring intensity and other such parameters which might affect spontaneous CO gas bubble formation.

2.4. Reactions at Gas Bubble Interface

Ar gas is injected into the ladle in a VTD to mix the decarburized steel at the top with the steel in the lower region. Ar stirring also enhances the steel/slag/gas reactions. Further, Ar with zero partial pressure of CO at the bottom picks up C and O from the liquid metal by providing a steel/gas-bubble interface for CO formation.

For iso-thermal conditions, the total volume of the gas increases with increasing height due to reduction in the local pressure. Total gas volume at a given depth in the melt can be calculated by the following equation:

$$V_h = \frac{(P_a + \rho_m g H_m + \rho_s g h_s) V_H}{(P_a + \rho_m g h_m + \rho_s g h_s)} \quad (3)$$

where,

V_h = total argon volume at a depth of h in the melt

H = total depth of the melt, m

V_H= initial argon volume

Bubbles also grow due to the purging of CO from the melt. The gas volume further increases due to the flux of material into the bubble. The mass transfer coefficient (k_b) was calculated using Higbie's surface renewal theory[20], given by:

$$k_b = 2\sqrt{\frac{D}{\pi t_c}} \quad (4)$$

where,

D = diffusivity of transferred species in the melt, (1×10^{-9} m^2/s)[21]

t_c = time of contact (s), which can be calculated by $t_c = {}^{d_b}/_{u_b}$, where d_b = bubble diameter (m) and u_b = relative bubble velocity (m/s)

The total mass transfer in the steel for reactions at the steel/gas-bubble interface was calculated by:

$$Q_b = k_b A_b \rho_m \quad (5)$$

where,

A_b = total bubble surface area in the zone

To determine the total surface area of the bubbles in a zone, bubbles in a zone were assumed to be of uniform size. The initial diameter (d_0) for the Ar bubbles can be calculated by using the equation given by Mori et al.[22]:

$$d_0 = \left(\frac{6\sigma d_n}{g\rho_m}\right) \quad (6)$$

where,

σ = surface tension of steel, 1.7 N/m[23,24]

d_n = pore diameter of the porous plug (0.015 m)[23]

Total number of bubbles entering the steel at a given time-step was calculated by dividing the total gas volume (determined by gas flow rate) by the initial bubble size. These bubbles grow as they rise in the melt and then fracture. Wichterle[24] has described a mechanism for break-up of gas bubbles rising in molten steel which was used in the present study. Using this mechanism the average bubble sizes were calculated at each time step for different Ar flow rates at different depths in the melt. The average bubble size was calculated to be in the range 0.012 – 0.022 m, which are in agreement with the values in the literature.[23-25] The average bubble size was the smallest for zone 5d and largest for zone 5a. The relative bubble velocity in steel used for the model was 0.35 m/s, which has been reported by researchers in the literature for the bubbles of 0.02 m

diameter.[23,25] The total number of bubbles increased as the gas moved up in the ladle thereby increasing the total steel/gas-bubble interface area.

Pure Ar was injected into zone 5d, where it reacted with steel and inclusions. The reacted gas and inclusions were then carried to zone 5c forming the steel/gas-bubble interface for this zone. This procedure was followed into zone 5b and 5a after which the inclusions were carried to the steel/slag/gas interface.

2.5. Reactions at the Steel/Slag/Gas Interface

The bulk slag (which consisted of slag, solid-solutions and solid compounds) was reacted with the steel present in the top layer (zone 0) and the reacted gases and inclusions rising in the melt. No argon bubbles were reacted at the steel/slag/gas interface as this gas was assumed to go out through the open eye. All the inclusions coming in contact with the steel were assumed to be trapped in the slag phase. The total mass transfer flow (Q_m) for the steel was calculated by the following equation:

$$Q_m = k_m A_s \rho_m \tag{9}$$

where,

k_m = mass transfer coefficient in steel, m/s

A_s = total surface area of the interface, m^2

The mass transfer coefficient (k_m) varies with the changing Ar flow rate. Peter et al.[26] proposed the mass transfer rate constant (k , representing the fraction of steel reacting with the slag during one time-step) to be a function of the stirring intensity. The

mass transfer coefficient (k_m) would be proportional to this rate constant (k). Their work was performed for ladle of the same size (~110 metric tonnes) and similar gas flow rates (0-15 scfm). Using this approach the mass transfer coefficient can be expressed as:

$$k = 0.018\varepsilon^{0.47} \tag{10}$$

where,

k = mass transfer rate constant in min^{-1}

ε = stirring power is in Watts per metric ton, which can further be calculated by the following equation[27]:

$$\varepsilon = 14.23 \left(\frac{\dot{V}T}{M}\right) \log\left(1 + \frac{H}{1.48P_a}\right) \tag{11}$$

where,

$\dot{V}$ = Ar flow rate at standard temperature and pressure in m^3/min

T = absolute steel temperature

M = steel mass in tonne

H = the total depth of the melt in m and P_a is in atmosphere.

The mass transfer coefficient for the slag phase was assumed to be the same as that for the steel. The calculations for the varying mass transfer coefficients, total bubble surface area and flows between zones as a function of pressure at the surface, Ar flow rate and steel depth were calculated in the Excel workbook at every time-step.

3. MODEL VERIFICATION

The model was designed for an industrial process where liquid steel was treated in a VTD after melting and de-phosphorization in an electric arc furnace (EAF). The typical steel composition immediately after tapping is shown in Table 1. A typical heat contained about 100 metric tonne steel. This is equivalent to 3 m total height of the melt for an average ladle diameter of 2.5 m.

Table 1. Initial steel composition showing only the major constituents (Fe balance)

Components	Mn	Si	C	N	O	P	S	Cr	Ti
wt. %	0.125	0.003	0.033	0.0085	0.0918	0.014	0.0663	0.126	0.01

Every attempt was made to minimize carry-over EAF slag. Table 2 shows an averaged composition of EAF slag for about 70 heats. The simulations were run for carry-over EAF slag 450 kg, 900 kg and 1350 kg. Further, 90 kg tap-hole sand (~ 100% SiO_2), 270 kg dolomite (~60% CaO, 30% MgO, 10% SiO_2) and 45 kg magnesia (~ 95% MgO, 5% $MgCO_3$) were added to the ladle after tapping to build a new slag.

Table 2. EAF slag composition showing only the major constituents

Components	Al_2O_3	CaO	SiO_2	FeO	MnO	MgO
Wt %	7	31	17	23	7	14

In the VTD the pressure was dropped from $1x10^5$ Pa to $1x10^3$ Pa in about 5 minutes. The pressure was further reduced to 100 Pa at about 10 minutes from the start

of VTD operation and maintained at this pressure for about 3 minutes before a steel sample was taken. After de-C ferro-silicon and silico-manganese were added to the steel. This was followed immediately by lime addition to the slag for de-sulfurization. For de-sulfurization pressure of 100 Pa was maintained in the VTD for about 30 minutes. During the VTD operation Ar was purged into the ladle via two porous plugs at the bottom. The total Ar flow-rate during the initial de-carburization period was varied in the range of 0-15 scfm. Figure 5 shows a typical pressure and total Ar flow-rate profile used during the de-C period in the VTD.

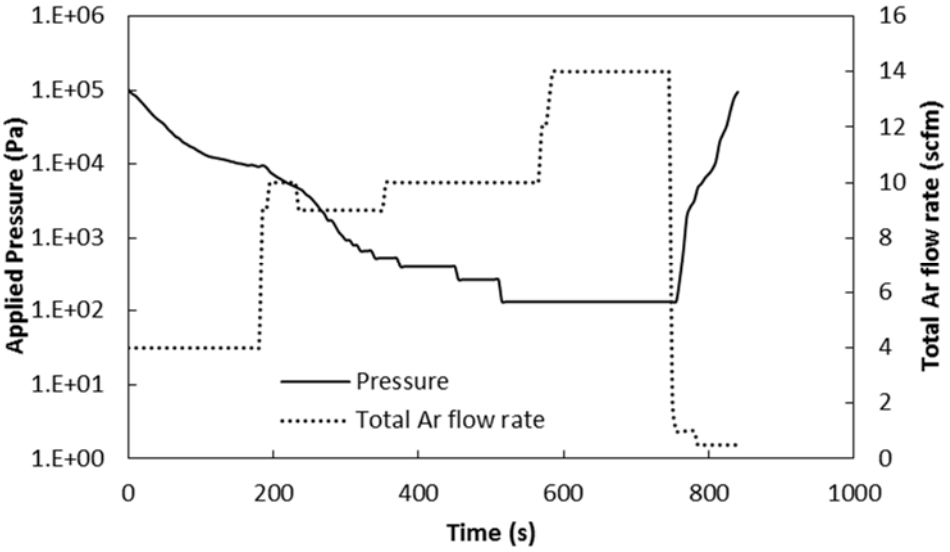

Figure 5. Profiles for applied pressure and total argon flow-rate (through two porous plugs) during de-carburization for Heat 1. Other heats have similar pressure and argon flow-rate histories.

Figure 6 shows simulation results as wt. % C in different zones inside the ladle for a particular heat. The comparison between the zones shows that the rate of de-C is the fastest for the zone with spontaneous CO bubble formation. The melt in this zone also

gets mixed with the steel already de-C in zone 0 due to steel/slag/gas interactions at the applied pressure. Industrial steel samples were only available at the start and end of de-C. The model prediction is close to the results obtained for the industrial samples. The simulation shown in Figure 5, was run for the VTD processing during degassing (pressure and Ar flow rates) for a particular heat (Heat 1 shown in Figure 5). Data for other heats, with similar VTD processing, has also been shown on the figure. The predicted de-C rate is in reasonable agreement with published experimental data.[28)]

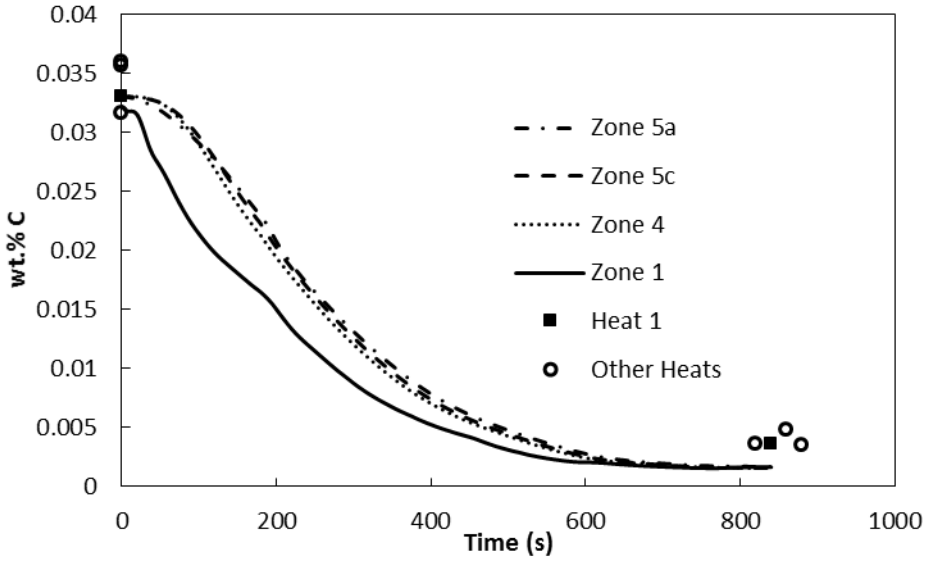

Figure 6. Comparison of C concentration in different zones of the ladle as predicted by the model for Heat 1. Other heats have similar VTD processing.

The model can be used to determine which of the de-C mechanism is more prominent. A comparison of amount of carbon removed by each of the mechanisms per unit time has been plotted in Figure 7. The weight of carbon removed per second was calculated from the gas phase exiting each zone. So, this value would depend on the Ar

flow rate at a given time. The de-C was more prominent through CO formation at steel/slag/gas interface due to the minimum local pressure. De-C at the steel/slag/gas interface is further enhanced by the presence of a highly oxidizing slag (FeO ~ 15-20%). Spontaneous CO bubble formation (in zone 1) subsided as the metal entering this zonewas already de-C in zone 0 at a lower local pressure. Towards the end, when the Ar flow was stopped the rate of reactions dropped significantly. This shows that, as is well-known, Ar purging is crucial to achieving required de-C in the VTD. The fluctuations observed in Figure 7 are a result of changes in Ar flow rate and pressure.

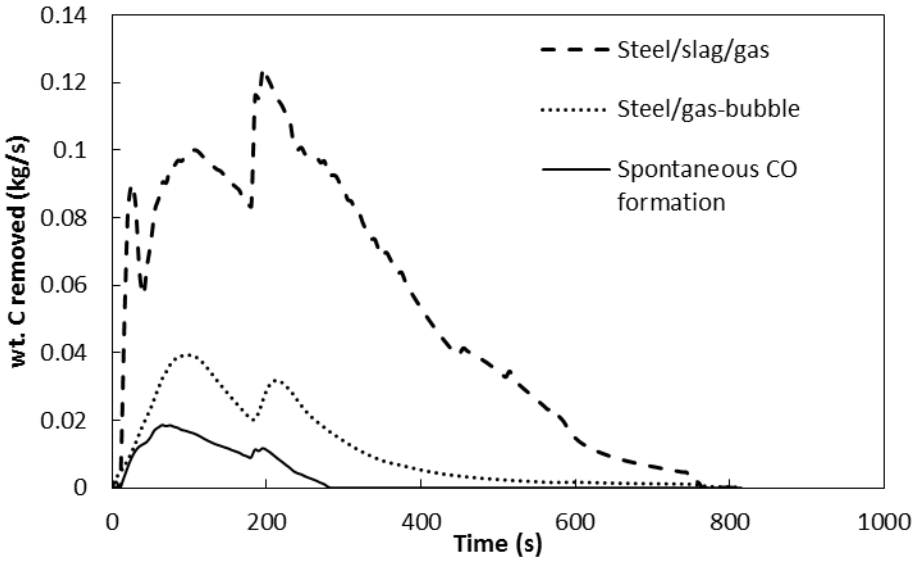

Figure 7. Comparison of de-carburization by the three mechanisms

Thermodynamic calculation for initial steel composition resulted in about 500 ppm slag in equilibrium with steel at 1600°C and $1x10^5$ Pa. This slag was assumed to be the total inclusion mass present in the steel. If we assume spherical inclusions of uniform

size of 2 μm diameter, the number of inclusions per cm^3 of steel volume is of the order of 10^8, which can act as nucleation sites for CO bubble nucleation.

The model calculates total inclusion mass and composition in each zone in the ladle at every time-step. The inclusions were assumed to be perfectly mixed with the steel and were involved in equilibrium calculation at each interface. Further, the inclusions coming in contact with the gas bubbles were assumed to be carried along with them finally separating at the top slag. This allows changes in the inclusion composition to be tracked as the conditions change during the process (Figure 8). The model predicted total inclusion mass to drop by 100 ppm in the zones 5 a-d and minimal change in zone 4. For zone 0 and zone 1 maximum drop in the total inclusion content was predicted (250-400 ppm).

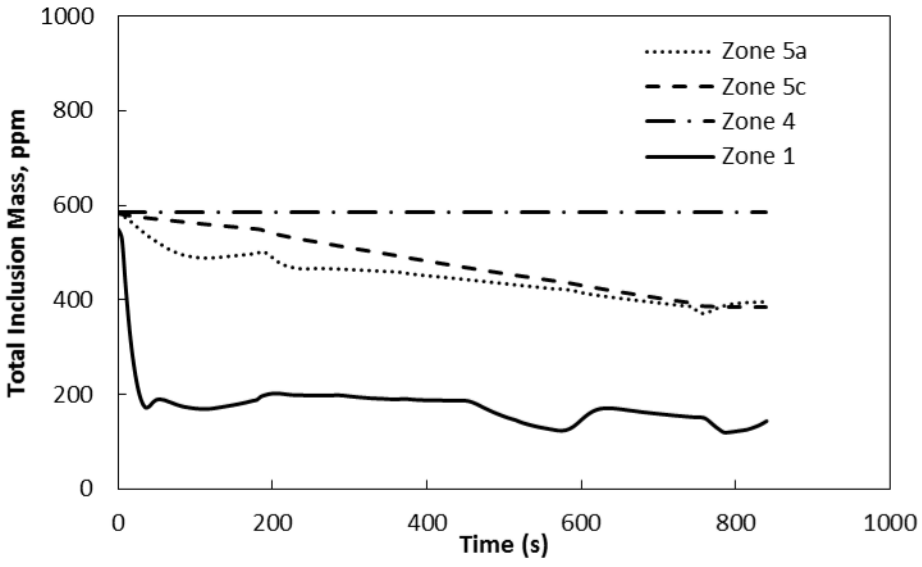

Figure 8. Comparison of total inclusion mass in ppm in different zones

4. CONCLUSIONS

A comprehensive model was developed using FactSage to calculate the state of the process under different conditions present during the operation in a VTD. All the possible reactions have been considered by including metal, slag, solid-solutions, solid compounds and all possible gases thus utilizing the full capabilities of the well-developed FactSage software and its databases. This model predicts steel, slag and inclusion composition in each zone throughout the VTD processing. The model also predicts the total inclusion concentration with time.

The present model utilizes the previously developed theories of bubble nucleation, growth and rupture during Ar purging to predict the mass transfer to the gas bubbles. Change in mass transfer to the steel/slag/gas interface has also been incorporated in the model. Even though a simple approach has been used for the spontaneous CO bubble formation, the model provides a valuable tool in determining the contribution of each mechanism towards overall de-carburization.

The model can be used as an online tool or run offline and used as a predictive tool.

The model provides a tool to see how concentration in the ladle varies throughout the whole volume. Parameters like mass transfer coefficients, rate constants, etc. can be easily entered into the model. The model was coupled with an Excel file, which is used for data entry, making the model flexible and easy to operate.

Steel/refractory interactions can also be added to the model. Further, the model can be extended to study de-sulfurization reactions in the ladle during VTD processing.

ACKNOWLEDGMENT

The authors would like to express their sincere appreciation of the late Professor Kent D. Peaslee for providing guidance and support for this research and for always being an inspiration to us.

REFERENCES

1) V. Thapliyal, S.N. Lekakh, K.D. Peaslee and D.G.C. Robertson: AISTech conf. Proc., ISS, Warrendale, PA, USA, (2012), 118.

2) M.A. Van Ende, Y.M. Kim, M.K. Cho, J. Choi and I.H. Jung: *Metallurgical and Materials Transactions B*, 42 (2011), 477.

3) H. Gaye, D. Huin and N. Bannenberg: Eleventh International Conference on Vacuum Metallurgy, ICVM 11, Antibes-Juan-les-Pins, France, (1992).

4) T. Kitamura, K. Miyamoto, R.Tsujino, S. Mizoguchi and K. Kato: *ISIJ Int*., 36 (1996), 395.

5) J.F. Domgin, P. Gardin, D. Huin, H. Saint-Raymond and F. Stouvenot: *Progress in Computational Fluid Dynamics An International Journal*, 4 (2004), 20.

6) D. Anghelina and G.A. Irons: 58th Ironmaking Conference, Chicago, IL, USA, (1999).

7) D. Anghelina and G.A. Irons: Iron & Steel Society International Technology Conference and Exposition 2003, Indianapolis, IN, USA, (2003).

8) H. Saint-Raymond, D. Huin and F. Stouvenot: *Materials Transactions, JIM*, 41 (2000), 17.

9) FLUENT 6.2: Fluent Inc., Lebanon, New Hampshire, Report, (2005).

10) METSIM Process Simulator: http://www.metsim.com, (2014).

11) C.W. Bale, P. Chartrand, S.A. Degterov, G. Eriksson, K. Hack, R. Ben Mahfoud, J. Melancon, A.D. Pelton and S. Petersen: *Calphad Journal*, 26 (2002), 189.

12) A. Kumar, V. Thapliyal and J. Smith: *Int. J. of Applied Ceramic Tech*., 11 (2014), 1001.

13) A. Kumar, V. Thapliyal, D.G.C. Robertson and J.D. Smith: *J. Am. Ceram. Soc*., (2015). doi: 10.1111/jace.13492.

14) K. Krishnapisharody and G. A. Irons: *Steel Research Int*., 81 (2010), 10.

15) D.G.C. Robertson: Proc. of the EPD Congress, T.M.S., Las Vegas, USA, (1995), 347.

16) D. Anghelina and G. A. Irons: AIST2003 Conf. Prof., ISS, Warrendale, PA, USA, (2003), 529.

17) T. Kitamura, K. Miyamoto, R. Tsujino, S. Mizoguchi and K. Kato: *ISIJ Int*., 36 (1996), 395.

18) S. Kitamura, M. Yano, K. Harashima and N. Tsutsumi: *Tetsu-toHagané*, 80 (1994), 213.

19) E. Kaddah and D.G.C. Robertson: Materials and Metallurgical Transactions B, 19 (1988), 831.

20) E. T. Turkdogan: "Physical Chemistry of High Temperature Technology", Academic Press, NewYork, (1980), 251.

21) D.G.C. Robertson, S. Wei and A. Raman: Chemical Process Metallurgy: The Elliott Symposium, G.R. St. Pierre, and P.J. Koros, Iron and Steel Society, Warrendale, PA, USA, (1990), 413.

22) K. Mori: *ISIJ Int*., 19 (1979), 552.

23) L. Zhang and S. Taniguchi: *International Materials Review*, 45 (2000), 59.

24) K. Wichterle: *Steel Research International*, 81 (2010), 356.

25) B.G. Thomas, A. Dennisov and H. Bai: 80th Steelmaking Conf., ISS, Warrendale, PA, 1997, 375.

26) J. Peter, K.D. Peaslee, D.G.C. Robertson and B.G. Thomas: AIST Tech 2004 Conf. Proc., ISS, Warrendale, PA, USA, (2004).

27) E.T. Turkdogan: "Fundamentals of Steelmaking", The Institute of Materials, London, (1996), 1.

28) J.F. Domgin, P. Gardin, D. Huin, H. Saint-Raymond and F. Stouvenot: *Progress in Computational Fluid Dynamics*, 4 (2004), 20.

2. SUMMARY

The present work discussed inclusion formation and evolution during the processing of thin-strip casting process. Thin-strip casting technology is still in its early phase of commercialization with many challenges including inclusion content of steel which can lead to problems like clogging, strip-breaks and surface defects. Inclusion engineering was studied for Mn-Si deoxidized steel focusing on inclusion evolution, transformation and modification by ferro-alloy additions. An understanding of how inclusions form and evolve during the process is key to finding possible methods of inclusion modification and removal.

A methodology to study the formation and evolution of inclusions soon after ferro-alloy additions (for alloying or deoxidation) has been developed. The knowledge of inclusion evolution in the early stages can help to understand the nucleation and growth of inclusions in the later stages. This methodology can be used for dissolution studies of other ferro-alloys as well. It can also be used to study the effect of the alloy additions to the inclusions already present in the steel. For thin-strip casting Mn-Si killed steels are preferred to achieve MnO-SiO_2 based liquid inclusions. In these steels ferro-silicon, ferro-manganese and silico-manganese are used. The dissolution behavior of ferro-silicon and ferro-manganese was studied in this work. Inclusions with solid SiO_2 at the interface were identified as possible heterogeneous nucleation sites for inclusions in the later stage of processing.

FeTi addition to transform Mn-Si-Al-O based inclusions in Mn-Si killed steel was studied. Even though most of the inclusions in Mn-Si killed steels are liquid at 1600ºC, their solidification during casting can cause problems. Transforming these inclusions by

Ti addition lowers their melting point. Thus, Ti addition has the potential of keeping the inclusions liquid during casting and rolling operation and by that, eliminating problems of strip break during casting and cracking during rolling. Ti addition can be very helpful in low Mn steels where solid SiO_2 inclusions are a major cause of concern. The new technique developed to represent inclusion composition (with more than three components) and size on a ternary diagram provides better visualization of inclusion population and can be used as a valuable tool to study inclusion evolution during steel processing.

In addition, a comprehensive model for Vacuum Tank Degassing (VTD), which is an essential component of thin-strip casting, was developed to estimate the removal of gaseous species from liquid steel. Removal of these species further helps in lowering the inclusion content of the steel. Using the model, compositional change in steel during VTD processing as well as inclusion content could be tracked. The model was able to replicate the industrial practice.

3. PROPOSED FUTURE WORK

Inclusion Formation Due to Ferro-Alloy Addition: Modification in the ping-pong sampler can be made by restricting the location of ferro-alloy particle inside the sampler. By restricting ferro-alloy motion, concentration variation of the alloying element in steel can be observed avoiding any variability in the dissolution process. In addition, thermodynamic modeling of inclusion formation can be performed for the range of composition obtained for the alloying element. Data for the model can be generated from the ferro-alloy dissolution experiment.

Inclusion Modification Using Ferro-Titanium Addition: In the previous experiments, to study modification of Mn-Si based inclusions by FeTi addition, it has been observed that too much FeTi was added which lead to their transformation to mainly Ti-Mn based inclusions. So, lower amount of FeTi can be added in steps for inclusion modification in Mn-Si killed steel. This experiment can also be used to determine the feasibility of FeTi addition to modify the solid SiO_2 inclusions observed in low Mn, Si-killed steels.

Inclusion Formation from Refractory Sources: To identify the inclusions from refractory sources, interactions of Mn-Si killed steel and the refractories used in thin-strip casting can be studied. Corrosion cup test can be performed by using the tundish refractory lining (MgO), core nozzle refractory (Spinel-C) and side-dam refractory (BN-ZrO_2-SiC). Mn-Si killed steel of typical chemistry at the LMF can be reacted at 1600°C with these refractories individually to study the formation of new inclusions as well as the evolution of existing inclusions. Further, the steel already reacted with one of the

refractories could be tested against other refractories. The modified or newly formed inclusions would be carried forward to interact with other refractories in the system.

VTD Model Verification: Trial heats can be run in the industry by varying argon and pressure profile into the VTD. This data can then be used in the model for verification. Such a study could be useful to determine the contribution of each mechanism towards decarburization in the VTD.

APPENDIX A.

DATA FROM AUTOMATED SCANNING ELECTRON MICROSCOPE

Effect of ASPEX settings on the EDS results was investigated. Following are the details of this study:

1. Effect of Spot Size

The spot control in ASPEX modifies the diameter and number of electrons in the beam striking the sample. The optimal spot setting depends upon the magnification. To assist in selecting a reasonable spot, a range of suggested spot sizes is displayed as a contrasting region on the background of the control. Smaller spot sizes are capable of producing higher quality images at high magnification. Larger spot sizes produce a larger, less noisy signal more appropriate for lower magnifications. The allowed range for spot size is 0.1 to 120%. The crossover of the condenser lens is represented by a value of 100%, and a typical working range is between 10 and 35%.

This study was performed for inclusions in the sample obtained after ferro-silicon (Fe75Si) addition. Figure 1 (a) shows typical inclusions formed on Fe75Si addition to the steel. Spot size was varied from 20% to 40% in steps of 5% to measure the chemistry and counts per second and real time.

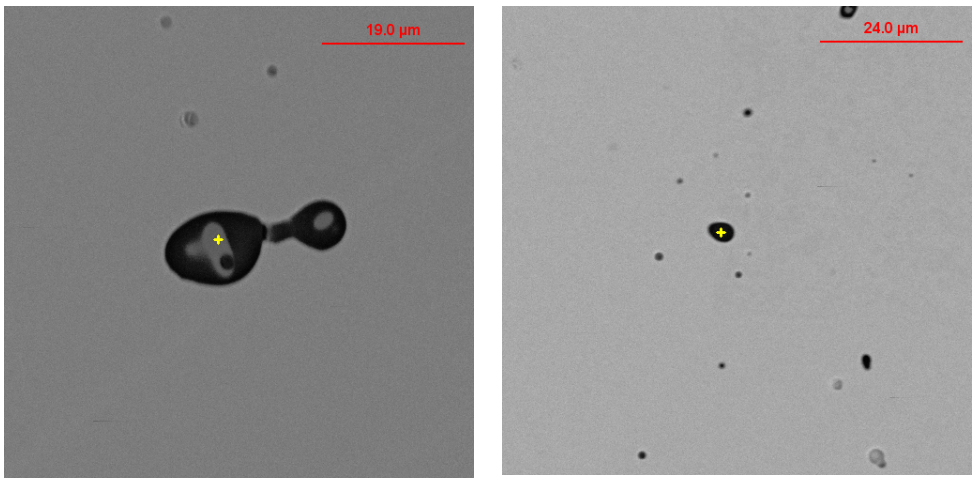

(a) FeSi Inclusion – 14 µm size (b) FeSi Inclusion – 4.5 µm size

Figure 1. Typical inclusions observed in steel after Fe75Si addition

Table 1. Inclusion composition for inclusion shown in Figure 1 (a) for different spot-sizes

Spot Size (%)	O (%)	Fe (%)	Si (%)
20	48.1	35.2	12.7
25	46.8	37	12.9
30	47.1	37.4	12.2
35	46.4	37.3	12.8
40	47	36.7	12.6
	47.08 ± 0.56	36.72 ± 0.80	12.64 ± 0.24

Table 2. Inclusion composition for inclusion shown in Figure 1 (b) for different spot-size

Spot Size (%)	O (%)	Fe (%)	Si (%)
20	52.9	9.4	34.5
25	52.5	8	36.3
30	52.3	8.6	36
35	54.2	8.3	34.4
40	51.9	8.5	36.5
	52.76 ± 0.79	8.56 ± 0.47	35.54 ± 0.90

Findings from the above analysis:

1. With the change in spot size, the composition of each element shows a minimal (±1.5%) variation.
2. The real time (time for EDS analysis) does not change with spot size. A variation of only 0.1 seconds was observed.
3. With increasing spot size the counts per second increases. It is advisable to have a high count per second without exceeding dead time beyond 50%.

2. Fe Content in the Inclusions:

After Fe75Si addition, large inclusion (17 µm) with a Fe rich area was observed. Elemental mapping also shows Fe-rich (Si depleted) region in the middle.

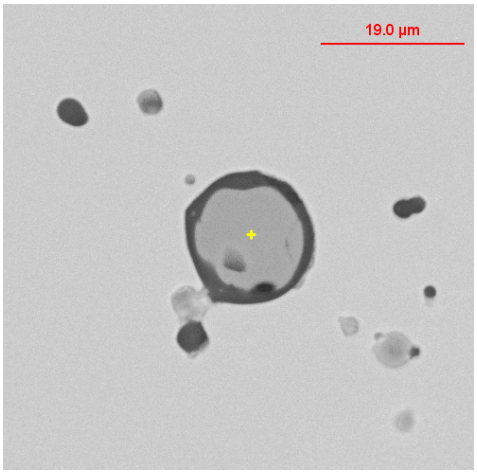

(a) SEM image of inclusion

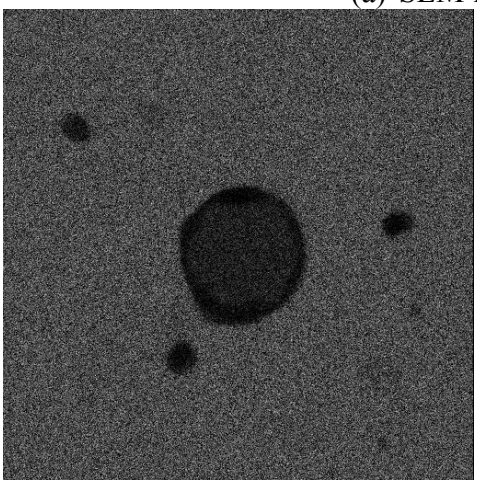

(b) Elemental map of Fe

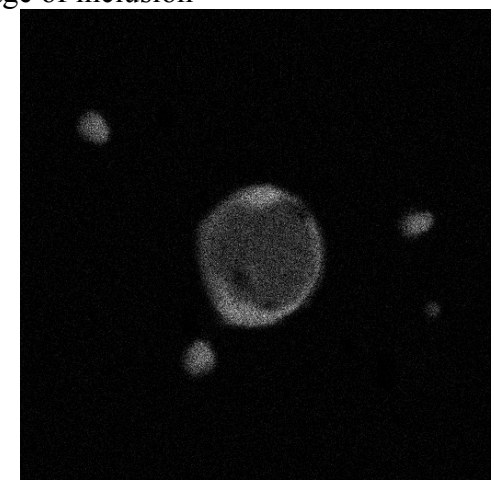

(c) Elemental map of Si

Figure 2. Inclusion with Si rich region surrounding a Fe rich core

Varying Fe content was observed in small inclusions (<2 µm). Figure 3 shows an example of small inclusions with varying Fe content after Fe75Si addition. Inclusion 2 is larger in size than inclusion 3 but has higher Fe content (Table 3). If Fe content was purely from the matrix then the inclusion chemistries should be reversed.

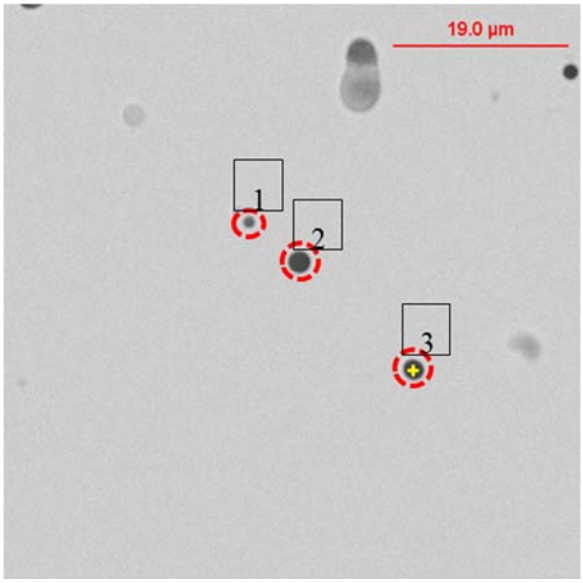

Figure 3. Inclusions with varying size and Fe content

Table 3. Inclusion composition for inclusion shown in Figure 3

Inclusion #	Diameter µm)	O (%)	Fe (%)	Si (%)
1	1.00	24	66.3	9.7
2	2.01	37.2	39.4	21
3	1.88	29	29	23.2

For ferro-manganese (FeMn) addition undissolved particles were observed in the steel. Figure 4 shows one such particle of size 800 µm. The particle shows two phases: light grey phase (marked as 1) with 93% Fe and dark grey phase (marked at 2) with only 38% Fe (43% Mn).

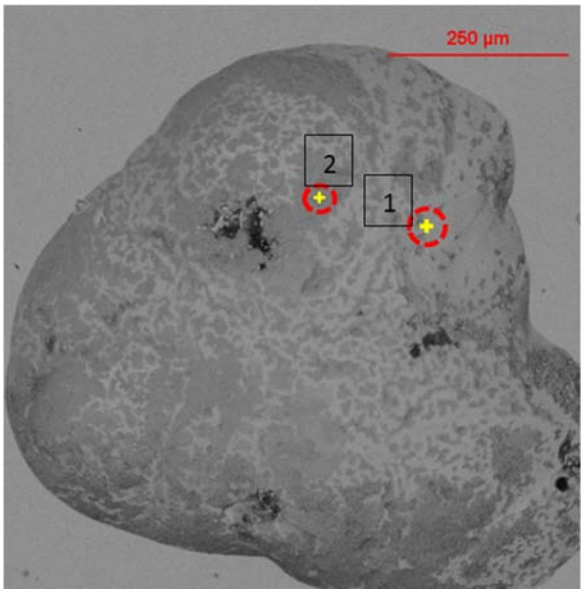

Figure 4. Undissolved FeMn particle observed in steel

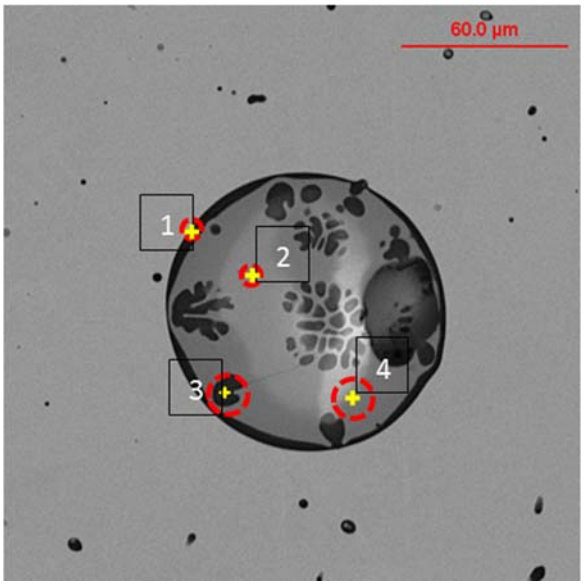

Figure 5. Typical inclusion observed in steel after Fe75Si+FeMn addition

When Fe75Si and FeMn were added together (Fe75Si+FeMn) to the steel the effect of stronger de-oxidation was observed as the inclusions were depleted in FeO content. Figure 5 shows a typical inclusion observed in steel after Fe75Si+FeMn

addition. The inclusion observed had a SiO_2 layer on the outside and regions of SiO_2 precipitation inside the inclusions (formed during cooling). The composition of the phases marked on this inclusion is provided in Table 4.

Table 4. Composition at different points marked on the inclusion in Figure 5

Inclusion #	O (%)	Si (%)	Fe (%)	Mn (%)	Al (%)
1	56	37.5	2.8	1	2.7
2	61.4	13.9	13.2	13	1.6
3	56.2	40.5	-	-	3.4
4	55.5	12.8	17.3	13.1	1.3

To validate the observations from ASPEX, inclusions cross-section was analyzed by using focused ion beam (FIB). Figure 6 shows a FIB cross-section of a typical inclusion observed in steel after Fe75Si+FeMn addition. The elemental map was plotted of the cross-section marked by a rectangular box on a relative scale. The map clearly shows SiO_2-rich ring on the outside of the inclusion. The interior of the inclusion has some Fe, which is significantly less than the matrix (edge of the rectangle).

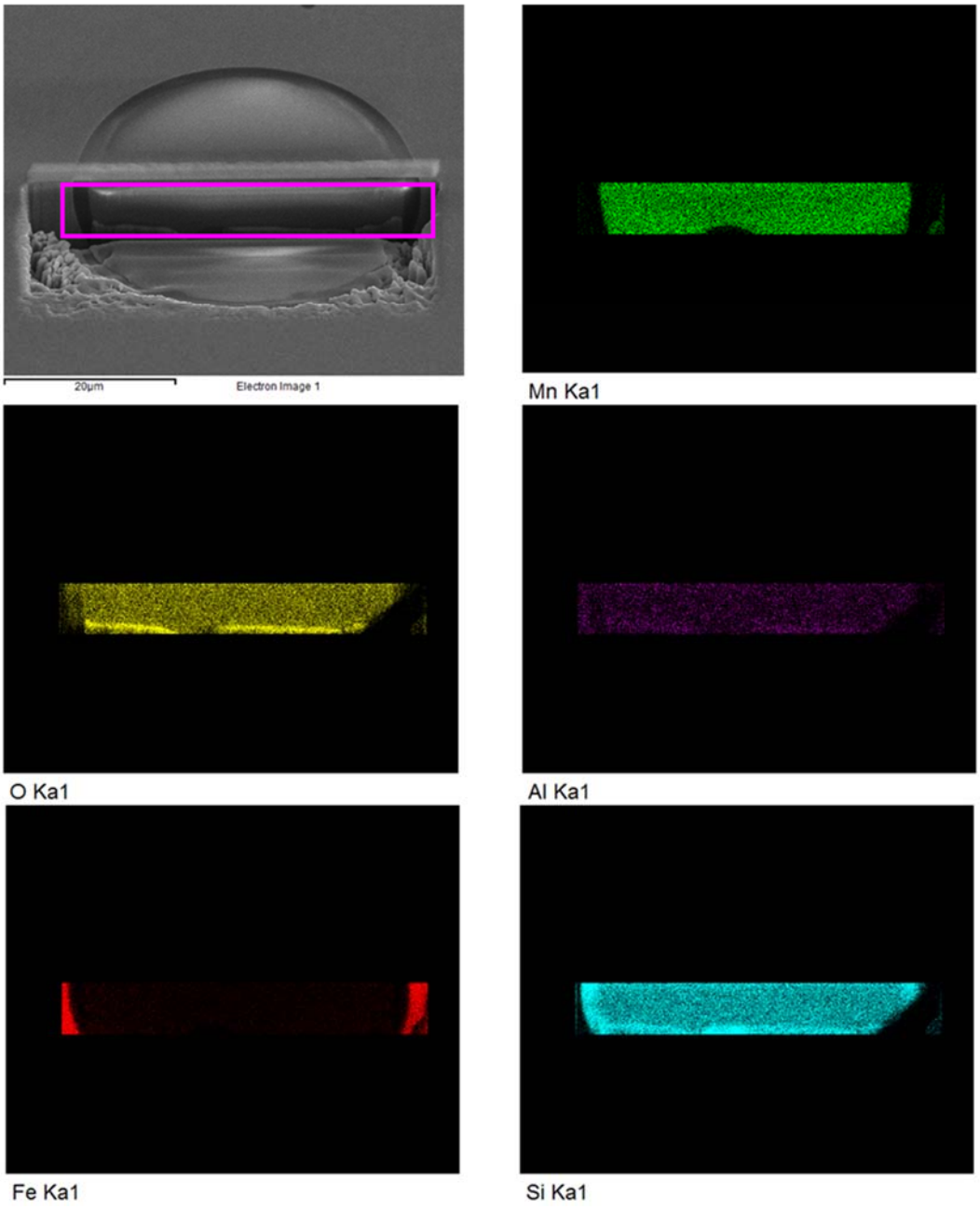

Figure 6. Elemental map of a FIB cross-section of an inclusion with Si-rich layer outside a Mn-Si-Al-Fe-O core observed in steel after Fe75Si+FeMn addition

APPENDIX B.

CALCULATION OF SOLIDIFICATION TIME IN THE CERAMIC SAMPLER

This appendix shows the calculations performed to estimate the total solidification time for steel in the ceramic sampler used to study ferro-alloy dissolution. As the sampler was dipped into liquid steel, a layer of solidified steel formed on the outside of the ceramic shell (Figure 1).

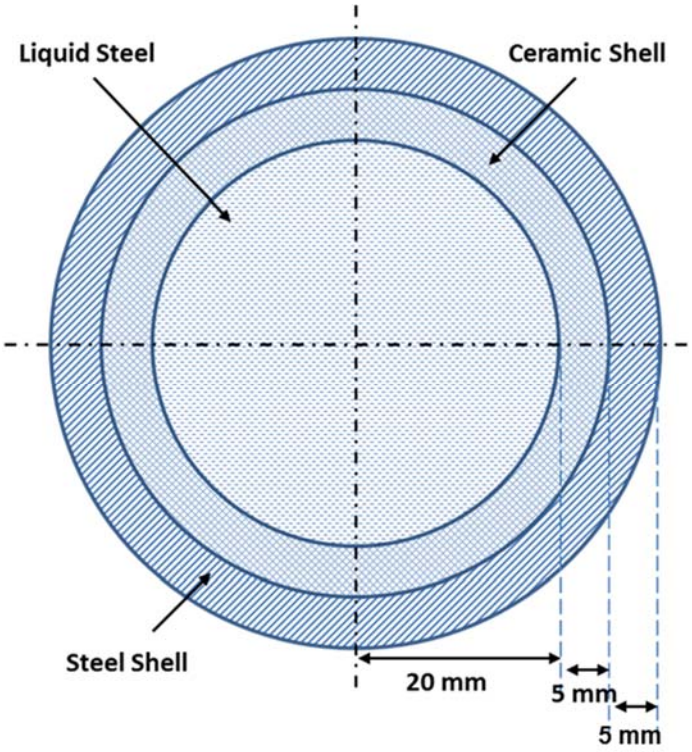

Figure 1. Representation of the sampler volume used for the solidification time calculation

The data used for calculation of solidification time is reported in Chapter 2 as Table 3. Following assumptions were used for these calculations:

- Initial shell temperature 673K.
- The solidified steel shell is of uniform thickness of 5 mm.
- Initial heat due to solidification of the outer layer goes into increasing the temperature of the ceramic shell.

Table 1 and Table 2 show the calculation results for heat released by steel and change in temperature of the ceramic shell respectively.

Table 1. Calculation for heat released by the solidified steel layer

Inner Radius (mm)	Outer Radius (mm)	Density (kg/m^3)	Heat of fusion for Steel (J/kg)	Total Heat (J)
25	30	7268	246557	85383.17

Table 2. Calculation for Temperature rise in the ceramic shell

Inner Radius (mm)	Outer Radius (mm)	Density (kg/m^3)	Heat Capacity (J/kg.K)	ΔT (K)
20	25	2020	1500	882.27

Using the above data, the total solidification time can be calculated as follows:

- At t=0,
  - T = 1873 K for 0 < R < 20 mm.
  - T = 1555 K for 20 mm < R < 25 mm
  - T = 1758 K (solidus temperature) for 25 mm < R < 30 mm
- For steady state,
  - T = 1758 K at R =20 mm.

For steady state heat loss,

Transfer due to conduction through (shell + solidified steel) = Rate of heat loss at the outer surface (R=30 mm) of the solidified steel due to convection + radiation

$$\frac{1758 - T_{R=.03}}{\frac{1}{4\pi k_{shell}}\left(\frac{1}{.02} - \frac{1}{.025}\right) + \frac{1}{4\pi k_{steel}}\left(\frac{1}{.025} - \frac{1}{.03}\right)} = h_{air} 4\pi(.03^2)(T_{R=.03} - 300) + \epsilon\sigma 4\pi(.03^2)({T_{R=.03}}^4 - 300^4)$$

Using $\epsilon = 0.5$,

- T = 1414.5 K at R = 30 mm.
- Rate of heat loss = 1415.9 Watts
- T = 1436.3 K at R = 25 mm.
- h_{air} = 10.45 W/m^2K

{ $h_c = 10.45 - v + 10\,v^{1/2}$

where, v = the relative speed of the object through the air (m/s) }

To reach steady state,

- Heat required by ceramic shell,

$$\int_{.02}^{.025} \rho_{shell} C_{p\ shell} (T_{shell} - 1555) 4\pi R^2\, dR$$

Where, $T_{shell} = 1758 + \frac{(1758-1436.3)}{(.02-.025)}(R - .02)$

On solving heat required = 2930.8 J

- Heat lost by solidified steel layer outside the shell

$$\int_{.025}^{.03} \rho_{steel} C_{p\ steel} (T_{steel} - 1758) 4\pi R^2\, dR$$

Where, $T_{steel} = 1436.3 + \frac{(1436.3-1414.5)}{(.025-.03)}(R - .025)$

On solving heat lost = 23665 J

For steel in the sampler to completely solidify (final T = 1758 K),

- Heat lost by liquid steel,

$$\frac{4}{3}\pi(.02^3)\rho_{steel}\left[\int_{1758}^{1873} C_{p\ steel}\, dT + L_{steel}\right]$$

On solving heat lost = 79221 J

Heat Balance

Total available heat (-2930.8 + 23665 + 79221) = Rate of heat loss x time

Time = 70 .6 seconds

APPENDIX C.

MnS PRECIPITATES ON TITANIUM-OXIDE INCLUSIONS

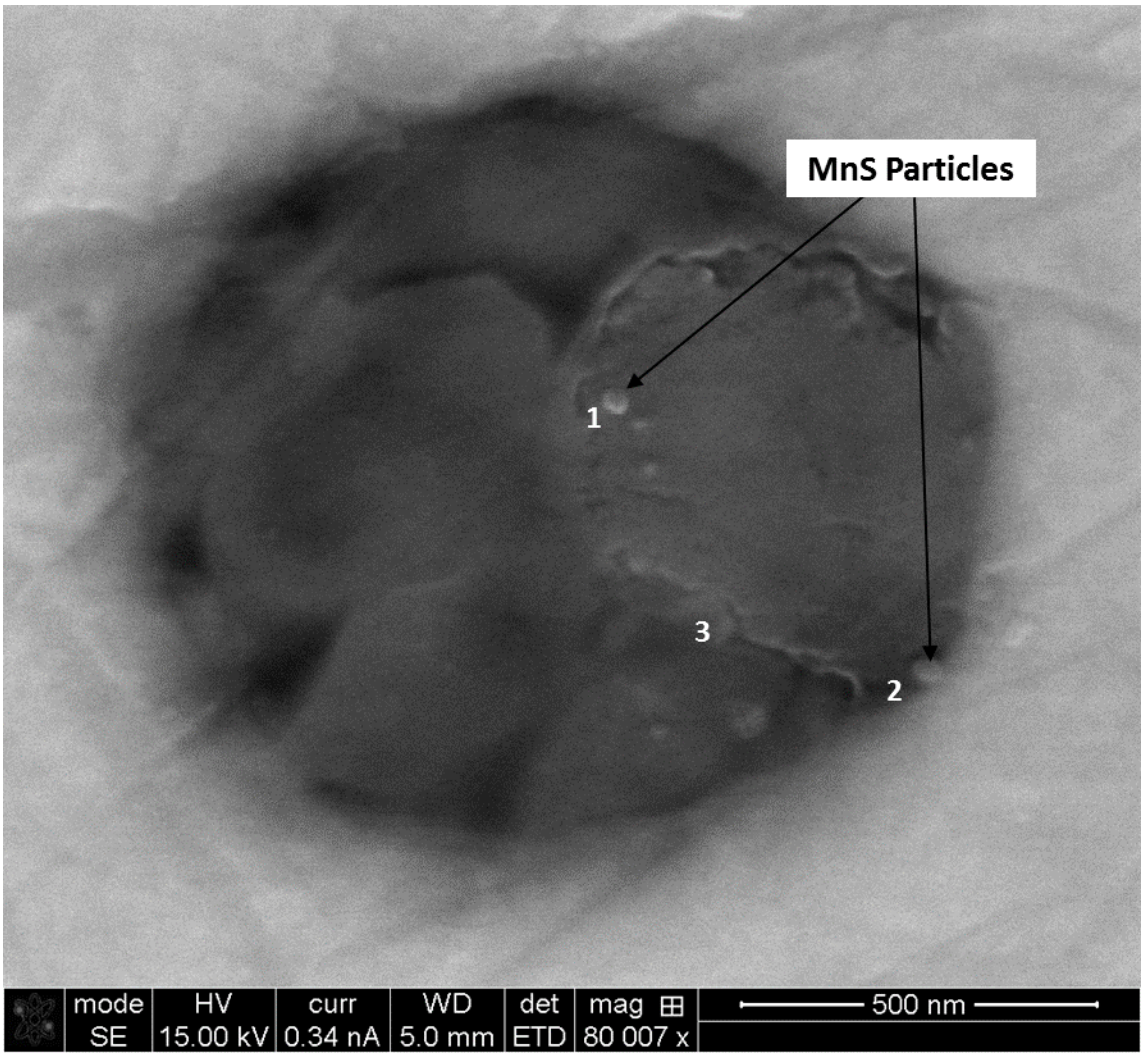

Figure 1. Inclusions observed in steel after FeTi addition with MnS particles precipitated on the oxide inclusions

Table 1. Composition at points marked in Figure 1

Element	Weight%		
	#1	#2	#3
O K	25.29	26.46	31.67
Al K	0.7	0.78	0.74
Si K	5.44	4.8	5.81
S K	6.28	6.59	0.6
Ti K	26.02	24.35	28.01
Mn K	20.7	20.6	13.91
Fe K	15.57	15.98	19.26

APPENDIX D.

MACRO PROCESSING USING FACTSAGE

FactSage provides a macro language which can be used to treat large and lengthy calculation. Macros can be used to automate the calculations which need to be repeated. Users can write series of commands and functions as calculation steps which are repeated by the macro processor. The macro processor loads "equilib" files, can read input parameters from an Excel file (or built-in the code), calculates the equilibrium and save the results. Then it moves on to the next step and repeats this procedure. Thus it enables the user to automatically run "equilib" files in the background. However, if Excel file is being used by the macro, it prevents the user from using Microsoft excel during the course of the simulation.

The first step to writing a macro code is to create "equilib" files and save them in a directory. FactSage macro processing looks for "equilib" and "stream" files in the defined

"My Files" directory. The default "My Files" directory in FactSage is "C:\FactSage\". Macro files can be created/edited with text editor. The extension for these files is "*.mac". There are four principal macro commands:

– OPEN: Opens the "equilib" file.

– CALC: Runs the "equilib" file.

– SAVE: Saves stream/data

– SHOW: Shows the "equilib" file during processing.

Following are the steps to run a macro file

- Go to the reactants window in the "Equilib" module
- Go to File → Macro processing → Run macro → Browse →
- Locate the "*.mac" file and open → ok

FactSage provides a feature called Object Linking and Embedding (OLE) to link FactSage with an excel workbook. By creating OLE links, user can read or write data to an excel workbook. Up to nine simultaneous dynamic links can be created (OLE1 to OLE9) allowing users to read/write data from nine worksheets. This feature can be used to read inputs and store intermediate Equilib calculation results into excel. Following are some basic commands to use with OLE:

- To create an OLE link – OLEn Excelfilename.xlsx sheetname (or .xls for older versions of excel)
- To clear cells – OLEn CELLS ALL CLEAR (for all cells in the worksheet)
  – OLEn RANGE A1:C3 CLEAR (for a range of cells)
- To read value from a cell – %var OLEn READ A1 or %var OLEn READ R10C10 (where %var is a variable)
- To write a value from a cell – %var OLEn WRITE A1 or %var OLEn WRITE R10C10
- To save and close excel link – OLEn CLOSE SAVE 'Excelfilename'
- To close worksheet without saving – OLEn QUIT

Variables can be defined in the macro language by using a "%" sign in front of the variable name. There are nine pre-declared variables (built-in notations), %1 to %9, which can be used without declaring them first. User variables can be declared by the VARIABLE statement. Following are some basic commands used along with variables:

- Value allocation – %var = 2 (with space before and after the "=" sign)
- %var STEP value – adds 'value' to %var
- %var STEP – adds 1 to %var
- Variables are used in defining loops

  %var = 'FirstValue' TO 'LastValue' STEP 'IncrementValue'

  (macro lines)

%var LOOP // End of loop.

A LOOP is always executed at least once ('FirstValue'). Loops can be nested.

The end of a macro is identified by the command “END”. “END” indicates the end of processing and all commands after that are ignored. User can create a jump to the END (quit the macro program) by using the command “GOTO END”.

- IF … GOTO END

The logical operators available in the macro language are: =, <, >, <> (not equal to), <=, >=. Multiple operators AND or OR can also be used. These can be combined with IF THEN ELSEIF operators.

- IF … THEN … ELSEIF … ENDIF

Nested IFs are NOT permitted.

Users can use REM to write remarks within the code. Another option to write comments within the code is to use “//”. The macro processor ignores anything written after “//” in a line. The use of comments in the code by using “//” makes it easier to read and understand the code. Following is a sample macro code:

```
REM // File VTD-Kinetics.mac - FactSage 6.4 (29Jan2015)

REM ================================
REM Remarks about the code.
REM ================================

HIDE                                        // hide the Equilib window
PAUSE 1                                     // pause the execution for
                                            // 1 sec to allow the
                          // user to read the comment
VARIABLE %Temp %row %col %dum               // user defined variables
%DIR C:\FactSage\test3
                                            // reset of default FactSage
                                            // directory
```

```
OLE1 Model-data.xlsx Datatest            // creation of OLE link
OLE2 Model-data.xlsx Results
%row = 2                                 // position of row to
%col = 2                                 // read/print
%dum = 1 TO 10                           // loop over max. time-step
                                         // in excel
%dum OLE2 WRITE R%rowC1                  // write time-step value into
                                         // 1st column of the current
                                         // row
IF %dum = 1 THEN                         // Initiation

OPEN EquiCreate-Steel-t0.DAT             // Open Equilib file to
                                         // create steel with the
                                         // initial composition
SET REACTANT 1 MASS 3534                 // set the value of 1st
                                         // reactant
                                         // in the equilib file
SET FINAL P 1                            // set Pressure at 1 atm
CALC                                     // execute the equilib file

SAVE MixtSteel-Zone0.DAT FSstel-LIQU     // Save the liquid steel
                                         // stream
SAVE MixtLIncl-Zone0.DAT FToxid-SLAGA    // Save the slag stream
SAVE MixtSIncl-Zone0.DAT SOLIDS          // Save all the solids

ENDIF

OPEN EquiFEM-Zone-1.DAT

%2 OLE1 READ R%rowC2                     // read from Excel
SET REACTANT 1 MASS %2                   // SET reactant 1 mass
%2 OLE1 READ R%rowC3
SET REACTANT 2 MASS %2
%2 OLE1 READ R%rowC4
SET REACTANT 3 MASS %2

%2 OLE1 READ R%rowC5                     // read from Excel
SET FINAL P %2                           // SET final pressure
```

```
CALC

%1 = 1 to 3                              // loop for values of
                                         // variable%1 from 1 to 3
%results = $E_mg%1$                      // store the weight of
                                         // solution no.%1 into
                                         // variable %results
%results OLE2 WRITE R%rowC%col           // write the stored value in
                                         // %results at currentrow
                                         // and column
%col STEP                                // increment %col value by 1
%1 LOOP                                  // continue loop until final
                                         // value ‘3’ is achieved
%col STEP                                // increment %col value by 1

%1 = 128 TO 152                          // loop from 128 to 152
%results = $E_sg%1$                      // store the weight of
                                         // species no.
                                         // %1 into %results variable
%results OLE2 WRITE R%rowC%col           // write in excel
%col STEP                                // increment %col value by 1

%1 LOOP                                  // end of loop
%row STEP                                // increment %row value by 1
%dum LOOP                                // continue loop %dum until
                                         // final
                                         // value ‘10’ is achieved
END                                      // end of macro
```

REFERENCES

1) J.P. Birat: *Ironmaking & Steelmaking*, 31 (2004), 183.

2) S. Ge, M. Isac and R.I.L. Guthrie: *ISIJ Int.*, 52 (2012), 2109.

3) H. Bessemer: US Patent 49053, (1865).

4) Z. Zhang, F. Zhang and F. Wang: *Research on Iron & Steel*, 39 (2011), 57.

5) Nucor Corporation: Castrip Technology, Process and Product Information Brochure, Castrip LLC, Charlotte, NC, (2014).

6) D.J. Sosinsky, P. Campbell, W. Blejde, R. Mahapatra and F. Fisher: *Metallurgist*, 52 (2008), 691.

7) T. Smith: 4th European Continuous Casting Conf., Steel Times International, Birmingham, UK, (2003), 29.

8) P. Campbell, W. Blejde, R. Mahapatra, R. Wechsler and G. Gillen: *Iron and Steel Technology*, 2 (2005), 56.

9) D. G. Edelman, P. C. Campbell, C. R. Killmore, K. R. Carprnter, H.R. Kau, J. G. Williams and W. N. Blejde: *Iron Steel Technol*., 6 (2009), 47.

10) C.R. Killmore, H. Creely, A. Phillips, H. Kaul, P. Campbell, M. Schueren, J.G. Williams and W. Blejde: *Materials Forum*, 32 (2008), 13.

11) S. Ge, M. Isac and R.I.L. Guthrie: *ISIJ Int*., 53 (2013), 729.

12) L. Holappa, M. Hämäläinen, M. Liukkonen and M. Lind: *Ironmaking &Steelmaking*, 30 (2003), 111.

13) Y. Higuchi, M. Numata, S. Fukagawa and K. Shinme: *ISIJ Int*., 36 (1996), S151.

14) L. Zhang and B.G. Thomas: *ISIJ Int*., 43 (2003), 271.

15) E. T. Turkdogan: "Fundamentals of Steelmaking", The Institute of Materials, London, (1996), 1.

16) S.A. Argyropoulos and R.I.L. Guthrie: Proc. Of the 65th Steelmaking Conf., ISS, Warrendale, PA, USA, (1982), 156.

17) S.A. Argyropoulos: Electric Furnace Proc., Detroit, Mich., USA, (1983), 81.

18) L. Holappa and S. Louhenkilpi: The 13th International Ferroalloys Congress, Almaty, Kazakhstan, (2013), 1083.

19) M.M. Pande, M. Guo, X. Guo, D. Geysen, S. Devisscher, B. Blanpain and Patrick Wollants: *Ironmaking & Steelmaking*, 37 (2010), 502.

20) P.V. Riboud, C. Gatellier, H. Gaye, J. Pontoire and P. Rocabois: *ISIJ Int*., 36 (1996), S22.

21) M. Iguchi, Y. Sumida, R. Okada and Z. Morita: *ISIJ Int*., 34 (1994), 164.

22) M.L. Yang, Z.S. Li, F.L. Wei, C.G. Cheng, X. Chen and S.B. Qi: *Advanced Materials Research*, 424-425 (2012), 811.

23) H. Solhed and L. Jonsson: *Scandinavian Journal of Metallurgy*, 32 (2003), 15.

24) "Treatise on Process Metallurgy", Vol. 2, ed. by S. Seetharaman, Elsevier, (2014), 266.

25) K. Beskow and D. Sichen: *Ironmaking & Steelmaking*, 31 (2004), 393.

26) S. Riaz, K.C. Mills and K. Bain: *Ironmaking & Steelmaking*, 29 (2002), 107.

27) M. Song, M. Nzotta and D. Sichen: *Steel Research Int*., 80 (2009), 753.

28) J.W. Cho, T. Emi, H. Shibata and M. Suzuki: *ISIJ Int*., 38(1998), 834.

29) J.W. Cho, H. Shibata, T. Emi and M. Suzuki: *ISIJ Int*., 38 (1998), 440.

30) Z. Feng, M. Changsong and L. Guangqiang: *Baosteel Technical Research*, 9 (2012), 47.

31) B.R. Marple, S. Poudrette and F.G. Hamel: 75th Steelmaking Conference Proc., Toronto, Canada, (1992), 353.

32) A. Kumar, V. Thapliyal and J. Smith: *Int. J. of Applied Ceramic Tech*., 11 (2014), 1001.

33) A. Kumar, V. Thapliyal, D.G.C. Robertson and J.D. Smith: *J. Am. Ceram. Soc*., (2015). doi: 10.1111/jace.13492.

34) A. Kumar, V. Thapliyal and J. Smith: *China's Refractories*, 0 (2015), 1.

35) "Treatise on Process Metallurgy", Vol. 3, ed. By S. Seetharaman, Elsevier, (2014), 347.

36) L. Zhang and B.G. Thomas: XXIV National Steelmaking Symposium, Morelia, Mich, Mexico, (2003), 138.

37) R. Kiessling: "Non-metallic Inclusions in Steel", The institute of Materials, London, (1968), Q87.

38) S. Maeda, T. Soejima, T. Saito, H. Matsumoto, H. Fujimoto and T. Mimura: Steelmaking Conference Proc., Vol. 77, ISS, Warrendale, PA, USA, (1989), 379.

39) G. Murtazaand R. Akid: *Eng. Fract. Mech*., 67(2000), 461.

40) 1997-2002 Kawasaki Steel 21st Century Foundation, 2003 JFE 21st Century Foundation in http://www.jfe-21st-cf.or.jp/chapter_1/1c_1.html

41) V. B. Ginzburg and R. Ballas: "Flat Rolling Fundamentals", ed. by Marcel Dekker, Inc., New York, Basel, (2000), 354.

42) L.A. Frank: Steelmaking Conference Proc., Vol. 84, ISS, Baltimore, Maryland, (2001), 403.

43) C. E. Sims: *Trans. Met. Soc. AIME*, 215 (1959), 367.

44) L.O. Uhrus: "Clean Steel", Special Report No. 77 of Iron and Steel Institute, London, 1962, 104.

45) J.D. Murray and R.F. Johnson: ISI Special Report 77, London, 1963, 110.

46) M. Atkinson: *JISI*, 195 (1960), 64.

47) A. Josefsson, Y. Koeneman and G. Lagerberg: *JISI*, 191 (1959), 240.

48) A. Schoberl: Radex-Rundschau, (1966), 170.

49) G. Hassal and K. Mills: "Fundamental Studies Related to the Mechanisms of Inclusion Removal from Steel", Technical Steel Research, (1987), 31.

50) R. Kiessling: *Met. Sci*., 14(1980), 161.

51) "Treatise on Process Metallurgy", Vol. 3, ed. By S. Seetharaman, Elsevier, (2014), 358.

52) J. Takamura and S. Mizoguchi: The 6th International Iron and Steel Congress, Vol. 1, IISC, Nagoya, Japan, (1990), 591.

53) S. Mizoguchi and J. Takamura: The 6th International Iron and Steel Congress, Vol. 1, IISC, Nagoya, Japan, (1990), 598.

54) Z. Ma and D. Janke: *Acta Metallurgica Sinica*, 11 (1998), 79.

55) Zhongting Ma : "Control of Nonmetallic Inclusions in Continuously Cast Steels in View of Macro-cleanliness, Castability, Precipitation Modification and Grain Refinement", PhD Thesis, TU Bergakademie Freiberg, Germany, 2001.

56) "The Making, Shaping and Treating of Steel", 11th edition, ed. By R.J. Fruehan, The AISE Steel Foundation, Pittsburg, PA, (1998), 693.

57) "The Making, Shaping and Treating of Steel", 11th edition, ed. By R.J. Fruehan, The AISE Steel Foundation, Pittsburg, PA, (1998), 151.

58) R.J. Fruehan: "Vacuum Degassing of Steel", ISS, Warrendale, PA, (1990), 1.

59) N. Bannenberg, P. Chapellier and M. Nadif: *Steel Research*, 113 (1993),75.

60) N. Bannenberg, B. Bergmann and H. Gaye: *Steel Research*, 63 (1992), 431.

61) FLUENT 6.2: Fluent Inc., Lebanon, New Hampshire, Report, (2005).

62) I.-H. Jung, S. Decterov and A.D. Pelton, "Computer Applications of Thermodynamic Databases to Inclusion Engineering", *ISIJ Int*., 44 (2004), 527.

63) METSIM Process Simulator, Available at http://www.metsim.com, (2014).

64) L. Zhang, S. Taniguchi and K.Cai: *Metallurgical and Materials Transactions B*, 31 (2000), 253.

65) B. Kaufmann, A. Niedermayr, H. Sattler, and A. Preuer: *Steel Res*., 64 (1993), 203.

66) K.-H. Tacke and J.C. Ludwig: *Steel Res*., 58 (1987), 262.

67) Y. Sahai and T. Emi: *ISIJ Int*., 36 (1996),166.

68) A.K. Sinha and Y. Sahai: *ISIJ Int*., 33 (1993), 556.

69) Lindborg and Torssell: *Trans AIME*, 242 (1968), 94.

70) P. Rocabois, C. Gatellier and J.P. Teres: *Ironmaking and Steelmaking*, 30 (2003), 95.

71) P. Kozakevitch and M. Olette: "Production and Application of Clean Steels", The Iron and Steel Institute, London, (1972), 42.

72) A. W. Cramb and I. Jimbo: W. O. Philbrook Memorial Symposium Proc., ISS,Warrendale, PA, (1988), 259.

73) H. Gaye, L. D. Lucas, M. Olette and P. V. Riboud: *Can. Metall. Q*., 23 (1984), 179.

74) K. Nogi and K. Ogino: *Can. Metall. Q*., 22 (1983), 19.

75) J. Mancini and J. Stel: *Rev. Métall., CIT*, 89 (1992), 269.

76) D. Bourisa and G. Bergeles: *Metallurgical and Materials Transactions B*, 29 (1998), 641.

77) S.K. Michelic, M. Hartl, B. Mario and C. Bernhard: AISTech 2011 Proc., Vol. II, ISS, Warrendale, PA, USA, (2011), 617.

78) R. Dippenaar: *Ironmaking & Steelmaking*, 32(2005), 35.

79) S.H. Lee, C. Tse, K.W. Yi, P. Misra, V. Chevrier, C. Orrling, S. Sridhar and A. W. Cramb: *Journal of non-crystalline solids*, 282 (2001), 41.

80) K. G. Rackers and B. G. Thomas: 78thSteelmaking Conference Proc., ISS, Nashville, TN, (1995), 723.

81) R.B. Tuttle: "Innovative Refractories for Preventing Nozzle Clogging in Continuously Cast Aluminum-Killed Steels", PhD Thesis, Missouri S&T, MO, (2004).

82) S. Ogibayashi: *Taikabutsu Overseas*, 15 (1995), 3.

83) T. Kawawa and M. Ohkkubo: *Transactions ISIJ*, 8 (1968), 203.

84) K. Krishnapisharody and G.A. Irons: *Steel Research international*, 81 (2010), 880.

85) M. Ek, P. Valentin and D. Sichen: *Steel Research international*, 81 (2010), 1056.

86) E.T. Turkdogan: "Fundamentals of Steelmaking", The Institute of Materials, London, (1996), 251.

87) Y.J. Kang, L. Yu and D. Sichen: *Ironmaking and Steelmaking*, 34 (2007), 253.

88) V. Chevrier and A. Cramb: Proc. Prof. Holappa Conference on 'Metal separation technology', Copper Mountain, CO, (2004), 10.

89) J.P. Bellot, V.D. Felice, B. Dussoubs, A. Jardy and S. Hans: *Metallurgical and Materials Transactions B*, 45 (2014), 13.

90) B.G. Thomas, A. Dennisov and H. Bai: 80th Steelmaking Conference Proc., ISS, Chicago, IL, (1997), 375.

91) L. Zhang, J. Aoki and B.G. Thomas: *Metallurgical and Materials Transactions B*, 37 (2006), 361.

92) P. Cremer and J. Driole: *Metallurgical and Materials Transactions B*, 13 (1982), 45.

93) N. Kaddah: Conf. Records of IEEE on Industrial Applications, IEEE, Piscataway, NJ, (1988), 1162.

94) J. Alexis and J. Bjorkvall: AISTech 2011 Proc., ISS, Warrendale, PA, USA, (2011), 1389.

95) O.J. Ilegbusi and J. Szekely: *ISIJ Int*., 29 (1989), 1031.

96) L. Limoges and L. Beitelman: *Iron Steelmaker*, 24 (1997), 49.

97) P.C. Glaws, R.V. Fryan and D.M. Keener: 74th Steelmaking Conference Proc., ISS, Warrendale, PA, (1991), 247.

98) E. Pretorius, H. Oltman and T. Cash: AIST 2010 Conf. Proc, ISS, Warrendale, PA, USA, (2010), 31.

99) S. Yang, J. Li, Z. Wang, J. Li and L. Lin: *International Journal of Minerals, Metallurgy, and Materials*, 18 (2011), 18.

100) G. Walter, G. Torga, F. Fuhr and C. Cicutti: AISTech 2003 Conf. Proc., ISS, Warrendale, PA, USA, (2003), 165.

101) P.C. Pistorius, P. Presoly and K.G. Tshilombo: Proc. of TMS Annual Meeting and Exhibition, San Antonio, TX, (2006), 373.

102) N. Verma, M. Lind, P.C. Pistorius, R.J. Fruehan and M. Potter: *Iron and steel Technology*, 7 (2010), 189.

103) N. Verma, P.C. Pistorius, R.J. Fruehan, M. Potter, H.G. Oltmann and E.B. Pretorious: *Metallurgical and Materials Transactions B*, 43 (2012), 830.

104) G. Yuming, X. Zhongbo and W. Haitao: *Iron Steel Vanadium Titanium*, 3(2007), 7.

105) I.H. Jung, G. Eriksson, P. Wu and A. Pelton: *ISIJ Int*., 49 (2009), 1290.

106) W.C. Doo, D.Y. Kim, S.C. Kang and K.W. Yi: *Metals and Materials Int*., 13 (2007), 249.

107) M. Fernandes, J.C. Pires, N. Cheung and A. Garcia: *Materials Characterization*, 51 (2003), 301.

108) P. Misra, V. Chevrier, S. Sridhar, and A.W. Cramb: *Metall. Mater.Trans. B*, 31 (2000), 1135.

109) Y. Kanga, I. Jung and H. Lee: *Calphad*, 30 (2006), 226.

110) H. Amitani, K. Morita and N. Sano: *ISIJ Int*., 36 (1996), S26.

111) A. Costa e Silva: *Rare Metals*, 25 (2006), 412.

112) C. Garlick, M. Griffiths, P. Whitehouse and C. Gore: *Ironmaking and Steelmaking*, 29 (2002), 140.

113) R. Kiessling: "Non-metallic Inclusions in Steel", The Institute of Materials, London, (1978), I7.

114) A. Hultgren: *Jernkont. Ann*., 129 (1945), 633.

115) I.H. Jung, Y. Kang, S.A. Decterov and A.D. Pelton: *Metallurgical and Materials Transactions B*, 35 (2004), 259.

116) R.B. Snow: *Journal of American Ceramic Society*, 26 (1943), 11.

117) G. Roghani, E. Jak and P. Hayes: *Metallurgical and Materials Transactions B*, 33 (2002), 827.

118) Y.B. Kang, H.S. Kim, J. Zhang and H.G. Lee: *Journal of Physics and Chemistry of Solids*, 66 (2005), 219.

VITA

Vivek Thapliyal was born November, 7, 1984 at Chamoli, Uttrakhand, India. He received his B.Tech. in Materials and Metallurgical Engineering in May 2007 from Indian Institute of Technology (IIT), Kanpur, India. From November 2007 to May 2009, he was a business analyst at marketRx, Gurgaon, India. Following that he worked with Professor B. Deo as a senior research associate at IIT, Kanpur till May 2010. In August 2010, he started working as a graduate research assistant with Dr. Kent D. Peaslee at Missouri S&T. He continued his research with Dr. Jeffrey D. Smith and received his PhD in Material Science & Engineering in May 2015 from Missouri University of Science and Technology. During his stay at Missouri S&T, he taught labs and lectures on steelmaking for undergraduate courses.

Mr. Thapliyal was an active member of AIST since 2010 and has presented posters and paper at AISTech conferences. Additionally, he was a member of Alpha Sigma Mu since 2011.